

Device Physics and Applications of Ternary Organic Photovoltaics

by

Xinjing Huang

A dissertation submitted in partial fulfillment
of the requirements for the degree of
Doctor of Philosophy
(Applied Physics)
in the University of Michigan
2023

Doctoral Committee:

Professor Stephen R. Forrest, Chair
Professor Hui Deng
Professor Cagliyan Kurdak
Professor Ctirad Uher

Xinjing Huang

xjhuang@umich.edu

ORCID iD: 0000-0002-9641-8369

© Xinjing Huang 2023

“It is the time you have wasted for your rose that makes your rose so important.”

—— Antoine de Saint-Exupéry, *The Little Prince*

ACKNOWLEDGEMENTS

Time always flies faster than we expect, and I'm coming to the finish line of my PhD journey. While challenging, this journey is undoubtedly exciting and full of remarkable moments. I am lucky and grateful to have met lots of fantastic people along the way, this dissertation could not have been accomplished without their help and support.

First and foremost, I would like to express my sincere gratitude to my advisor, Prof. Stephen Forrest, for his mentorship throughout these years. His exceptional insight and passion have opened the world of bridging physical science with engineering for me. He always pushes me to face the challenge and think outside the box, which profoundly shaped my path towards a qualified researcher. In addition, he is a perfect life mentor with his humor, his understanding in art and music, and experience in many other aspects of life besides scientific research. I am truly honored and grateful to have worked under his supervision.

Next, I want to thank the fantastic colleagues I have met in the OCM group. I am particularly thankful to Yongxi Li, my mentor, who introduced me to the field of organic photovoltaics and carefully trained me on device fabrication and characterization. I would also like to thank Xiao Liu for teaching me device physics and Dejiu Fan for his mentoring on nanofabrication and photolithography. I also thank Claire Arneson for our collaboration in OPV degradation and side-by-side OLED, Bin Liu for our collaboration on polariton photodetector, and Quinn Burlingame, Xiaoheng Huang, Rachel Koltun, Byungjun Lee, Boning Qu and Hafiz Sheriff for the great experience of working together in the SunShot and SETO project teams. I am also

grateful to have met all other members in the group for our enjoyable time together, including Xiaozhou Che, Caleb Coburn, Kan Ding, Jeffery Horowitz, Shaocong Hou, Jongchan Kim, Rebecca Lentz, Peicheng Li, Jihun Lim, Sritoma Paul, Yue Qu, Siwei Zhang and Haonan Zhao. My special thanks go to our group administrative Eva Ruff, my life has been much easier with her help on the logistics.

I would also like to acknowledge my collaborators outside the group, including Prof. Mark Thompson's group from the University of Southern California and Prof. Jian Fan's group from Soochow University. They are both groups full of outstanding chemists, providing me with great help from the materials and chemistry aspect. I also thank my friends Sicen Du, Junhong Guo, Xiaoer Hu, Guanglong Huang, Hongling Lott, Weitao Sun, Xinyan Wang, Luze Xu and many others, with whom I spent lots of joyful time after work to refresh myself.

Last, but not least, I want to thank my family who have given me constant support, love and care. Especially, I owe thanks to the two people who first taught me to speak and think. Thanks Mom and Dad, for everything I have accomplished and I can imagine. Finally, to my husband Dejiu who has been my mentor in both research and life: I have been working on solar cells and you are my sun, I am so grateful to have you as my life partner.

Xinjing Huang

Ann Arbor, MI

August, 2023

TABLE OF CONTENTS

DEDICATION	ii
ACKNOWLEDGEMENTS.....	iii
LIST OF TABLES	x
LIST OF FIGURES.....	xi
ABSTRACT	xiv
Chapter 1 Introduction	1
1.1 Properties of Organic Semiconductors	2
1.1.1 Organic Molecules	3
1.1.2 Excitons.....	5
1.1.3 Optical Properties.....	6
1.1.4 Exciton Transfer.....	8
1.1.5 Electronic Properties	10
1.1.6 Advantages of Organic Optoelectronics	10
1.2 Fundamentals of Organic Photovoltaics.....	12
1.2.1 Basics of OPV Operation.....	12
1.2.2 Device Architecture	15
1.2.3 Device Characterization.....	18
1.2.4 Advantage of OPVs: Semitransparent OPVs.....	20
1.2.5 Ternary Organic Photovoltaics.....	22
1.3 Organization of the Thesis	26
Chapter 2 Alloy or Blend: Analysis of Ternary Organic Photovoltaics.....	33
2.1 Criteria of Molecular Alloy	34

2.2 Characterization of a Ternary OPV System.....	36
2.2.1 Experimental Methods.....	36
2.2.2 Frontier Orbitals.....	38
2.2.3 Exciton States.....	39
2.2.4 Charge Transfer States.....	40
2.2.5 Absence of Molecular Alloy in Ternary OPVs.....	43
2.3 Evaluation of Other Possible Systems.....	44
2.4 Conclusion.....	46
Chapter 3 End-capping Exchange Leads to Unstable Ternary Organic Photovoltaic Cells.....	53
3.1 Introduction.....	54
3.2 Characterization of End-capping Exchange Reaction.....	56
3.2.1 Experimental Methods.....	56
3.2.2 Interaction between Archetype NFAs: BT-IC and BT-CIC.....	57
3.2.3 Reaction Conditions.....	58
3.2.4 Generality of Reaction.....	60
3.3 Impact of End-capping Exchange on Ternary OPVs.....	62
3.3.1 Experimental Methods.....	62
3.3.2 Impact on Device Reproducibility.....	65
3.3.3 Impact on Device Reliability.....	71
3.4 Degradation of CT State Electroluminescence and V_{OC}.....	73
3.4.1 Relationship between CT State EL and V_{OC} Degradation.....	73
3.4.2 CT State EL and V_{OC} Degradation of Ternary OPVs.....	76
3.5 Conclusion.....	77
Chapter 4 Impact of Dipolar Molecules on the Reliability of Ternary Organic Photovoltaic Cells.....	84
4.1 Introduction.....	85

4.2 Theoretical Calculation of Dipolar Molecules Reorganization.....	86
4.2.1 Theory	86
4.2.2 Simulated Reorganization of Dipoles	87
4.2.3 Calculation of Dielectric Constant Change.....	89
4.3 Impact of Dipolar Molecules on Ternary OPVs Reliability	90
4.3.1 Experimental Methods	90
4.3.2 Impact on Dielectric Constant	91
4.3.3 Impact on Device Reliability and Charge Collection Efficiency.....	93
4.4 Conclusion	96
Chapter 5 Ternary Tandem Organic Photovoltaic with Extended Near-	
infrared Absorption.....	102
5.1 Introduction.....	103
5.2 Materials Absorption	103
5.3 Ternary NIR Absorbing Sub-cell.....	105
5.3.1 Experimental Methods	105
5.3.2 Ternary Device Performance	106
5.3.3 Electronic States in the Ternary OPV	107
5.4 Tandem Solar Cell.....	109
5.4.1 Tandem OPV Structure	109
5.4.2 Experimental Methods.....	110
5.4.3 Device Performance.....	111
5.5 Conclusion	113
Chapter 6 Semitransparent Organic Photovoltaic Module with Minimal	
Resistance Loss	118
6.1 Introduction.....	119
6.2 Impact of Series Resistance on 1 cm² OPV.....	120
6.2.1 Experimental Methods	120

6.2.2 1-cm ² OPV Performance.....	124
6.3 Prototype ST-OPV Module	126
6.3.1 Module Design.....	126
6.3.2 Module Performance.....	127
6.4 Conclusion	129
Chapter 7 Multilevel Peel-off Patterning of Semitransparent Organic Photovoltaic Module	135
7.1 Peel-off Patterning Method.....	136
7.2 Module Fabrication	139
7.2.1 Multilevel Peel-off to Realize Series Connection.....	139
7.2.2 Module Layout Design	140
7.2.3 Experimental Methods.....	141
7.3 Prototype OPV Module Performance	143
7.3.1 Characterization Method.....	143
7.3.2 Opaque Module.....	144
7.3.3 Semitransparent Module with Optimized APT.....	145
7.3.4 Neutral Color Semitransparent Module.....	147
7.3.5 Discussion.....	148
7.4 Application of Peel-off Patterning in Other Organic Electronic Devices	149
7.4.1 Polariton-based Photodetector	149
7.4.2 Side-by-side White OLED Solid-state Lighting.....	150
7.5 Conclusion	151
Chapter 8 Outlook.....	159
8.1 Remaining Challenges in Understanding Ternary OPVs	160
8.1.1 Ternary OPVs with End-capping Exchange	160
8.1.2 Mechanism of Multi-nary OPVs.....	161
8.2 Prospects for ST-OPVs	163

8.2.1 Scalability of ST-OPVs	163
8.2.2 Reliability of OPV Modules	165
APPENDIX	173

LIST OF TABLES

Table 1.1 Comparison of properties of inorganic and organic semiconductors.....	2
Table 2.1 Summary of potential organic alloy systems.	45
Table 3.1 Charge transfer states emission peaks in binary and ternary OPVs.....	71
Table 5.1 Performance of PCE-10:BT-CIC:BEIT-4F ternary OPVs with different blend ratios under simulated AM1.5G illumination.	107
Table 5.2 Discrete sub-cells and tandem devices performances under simulated AM1.5G illumination.	112
Table 6.1 Performance of 4 mm ² and 1 cm ² OPV devices under simulated AM1.5G illumination.	126
Table 6.2 Performance of 9 cm ² ST-OPV module under simulated AM1.5G illumination.....	128
Table 7.1 Performance of 4 mm ² PCE-10:BT-CIC:TT-FIC OPV device, and 12.8 cm ² active area (13.34 cm ² total area) module under simulated AM1.5G illumination at 1 sun intensity.....	147

LIST OF FIGURES

Figure 1.1 Examples of organic molecules.....	3
Figure 1.2 Energetic diagram of semiconductors.	5
Figure 1.3 Illustration of excited state and excitons.	6
Figure 1.4 Optical transition energy diagram and spectra.	7
Figure 1.5 Three types of exciton energy transfer.	9
Figure 1.6 Advantages of organic optoelectronic devices.	11
Figure 1.7 Schematic illustration of photogeneration at organic heterojunction.....	13
Figure 1.8 Processes at organic heterojunctions.	14
Figure 1.9 Two types of organic heterojunction (HJ) architectures.....	16
Figure 1.10 Typical structure of single-junction organic photovoltaic (OPV) device.....	17
Figure 1.11 Illustration of tandem OPV structure.....	18
Figure 1.12 Characteristics of OPV devices.	19
Figure 1.13 Calibration of solar simulator source with a reference detector.	20
Figure 1.14 Structure and performance of ST-OPVs.....	21
Figure 1.15 Concept and properties of ternary OPV.....	23
Figure 1.16 Current models of ternary OPVs.	24
Figure 2.1 Ultraviolet Photoelectron Spectroscopy (UPS) measurements of ICBA:PC ₆₁ BM blends.	38
Figure 2.2 Photoluminescence (PL) measurements of ICBA:PC ₆₁ BM blends.....	40
Figure 2.3 Electroluminescence (EL) of ternary OPV devices and corresponding Gaussian fits.	41
Figure 2.4 Relationship between ternary OPV charge transfer (CT) state and blend ratio.	42
Figure 3.1 Generality of end-capping exchange reaction between A-D-A non-fullerene acceptors (NFAs).....	55
Figure 3.2 End-capping exchange reaction between archetype NFAs BT-IC and BTIC-4Cl.	57
Figure 3.3 Reaction conditions of end-capping exchange.	59
Figure 3.4 End-capping exchange between IT-IC and BTIC-4F with 4 reaction products.	61

Figure 3.5 End-capping exchange reaction of Y-series and perylene-series NFAs.	61
Figure 3.6 Impact of end-capping exchange reaction on archetype ternary OPV device reproducibility.	66
Figure 3.7 Generality of the impact of impurities on ternary device reproducibility.	67
Figure 3.8 Morphologies of neat and blend films.	69
Figure 3.9 EL spectra of binary and ternary OPVs.	70
Figure 3.10 Impact of end-capping exchange reaction on archetype ternary OPV device reliability.	71
Figure 3.11 Morphological changes of cold and hot ternary blend films over aging.	72
Figure 3.12 Change in charge extraction of cold and hot ternary OPVs over aging.	73
Figure 3.13 Non-radiative recombination loss during cold and hot ternary devices aging.	77
Figure 4.1 Dipolar molecules reorganization and electric field distribution in OPVs.	87
Figure 4.2 Simulated morphology of an acceptor blend containing dipolar molecules.	88
Figure 4.3 Calculation of internal voltages induced by dipolar molecules.	90
Figure 4.4 Capacitance-voltage ($C-V$) characteristics of devices with different ratios of dipolar molecules.	92
Figure 4.5 Summary of capacitance and relative dielectric constant before and after aging.	93
Figure 4.6 Carrier densities of OPV devices with different ratios of dipolar molecules.	93
Figure 4.7 Device performance degradation under 10 suns intensity illumination.	94
Figure 4.8 Evolution of charge extraction efficiency under 10 suns intensity illumination.	95
Figure 5.1 Absorption spectra of materials.	104
Figure 5.2 Performance of ternary OPVs based on PCE-10:BT-CIC:BEIT-4F with different blend ratios.	106
Figure 5.3 Electronic states in PCE-10:BT-CIC:BEIT-4F ternary OPVs.	108
Figure 5.4 Design of tandem OPV.	109
Figure 5.5 Ternary tandem OPV performance.	112
Figure 6.1 Schematic of 1 cm ² ST-OPV device structure.	121
Figure 6.2 Fabrication flow of Kapton shadow mask.	122
Figure 6.3 Performance of 4 mm ² and 1 cm ² OPV devices.	125
Figure 6.4 Schematic of the design of prototype ST-OPV module.	127
Figure 6.5 Performance of 9 cm ² prototype ST-OPV module.	128

Figure 7.1 Description of the peel-off patterning method.	138
Figure 7.2 Schematic illustration of multilevel peel-off patterning scheme.....	140
Figure 7.3 Design of module layout.	141
Figure 7.4 Optoelectronic properties of opaque OPV modules.....	144
Figure 7.5 Optoelectronic properties of the ST-OPV modules with out-coupling (OC) structure.	146
Figure 7.6 Optoelectronic properties of the neutral color ST-OPV modules.....	148
Figure 7.7 Peel-off patterned polariton-based organic photodetector.....	150
Figure 7.8 Peel-off patterned side-by-side white OLED for solid state lighting.....	151
Figure 8.1 Relationship between V_{OC} and blend ratio of cold and hot ternary devices.....	160
Figure 8.2 Relationship between V_{OC} and blend ratio of quaternary OPVs.	162
Figure 8.3 Efficiency loss in ST-OPV modules.....	164
Figure 8.4 Performance degradation of OPV modules.....	166

ABSTRACT

Organic photovoltaics (OPVs) are emerging as an attractive candidate for solar energy harvesting due to their advantages in environmental compatibility, low-cost, flexibility and transparency. The past few decades have witnessed substantial development in innovative molecular and device architecture designs to improve the performance of OPVs. The ternary bulk heterojunction (BHJ) devices stand out as one of the most widely employed strategies due to their broad absorption, efficient photocurrent generation and simple fabrication process. This thesis explores the working principles of ternary OPVs and demonstrates their application in high efficiency and scalable OPV devices.

The first part of the thesis focuses on the photogeneration process in ternary OPVs. We test the validity of the concept of “molecular alloy” by investigating the optoelectronic properties of a representative ternary system. Furthermore, we show that the end-capping exchange reaction between acceptor-donor-acceptor type of non-fullerene acceptors (NFAs) generates up to four unexpected molecular species in the ternary BHJs, leading to reduced reproducibility and reliability of OPV devices. The dipolar reaction products of the end-capping exchange are shown to reorient over time and impact the dielectric properties and device performance.

In the second part, we present the application of ternary OPVs in multi-junction devices and semitransparent modules. With the extended absorption in near-infrared (NIR) provided by a ternary sub-cell, we demonstrate high efficiency tandem OPV device. In addition, it is essential to

develop a scalable fabrication process of modules to commercialize OPV technology. We study the resistance loss when scaling up semitransparent OPV (ST-OPV) devices and demonstrate ultrafine metal grid structure in a prototype module to realize negligible efficiency loss from series resistance. Moreover, we introduce a high resolution, non-destructive multilevel peel-off patterning method in the fabrication of ST-OPV modules. Combined with a NIR-absorbing ternary BHJ, the ST-OPV mini-module simultaneously achieves high light utilization efficiency and geometric fill factor. The demonstrations in this dissertation provide insight to further understand the mechanisms, and then advance the application of ternary OPVs.

Chapter 1

Introduction

Organic semiconductors possess the chemical and mechanical benefits of organic compounds and the electronic properties of semiconductor materials. Owing to these features, organics have become an attractive solution to high performance, low cost and lightweight optoelectronic devices on flexible substrates over large area.^{1,2} The past few decades have witnessed the vast development of organic light emitting diodes (OLEDs) which are widely employed in the information display and solid-state lighting industry.³⁻⁸ The success of OLEDs has also facilitated the understanding of device physics as well as the evolution of fabrication technology of organic optoelectronic devices. As another application of organic semiconductors, organic photovoltaics (OPVs) are emerging as a promising alternative to convert solar to electrical energy. Although OPV technology is still in the transition stage from laboratory to commercialized products, the performance of OPVs has been steadily advancing towards power conversion efficiency (PCE) exceeding 20%⁹⁻¹³ as well as exceptional operational stability,^{14,15} which are comparable to the most efficient thin-film solar cell technologies. This chapter will give a brief introduction on the fundamentals of organic semiconductors and OPVs.

1.1 Properties of Organic Semiconductors

Although both are semiconductors, organic semiconductors have distinct properties compared to their inorganic analogs owing to the differences in the fundamental structures of the materials. Table 1.1 summarizes the main differences between organic and inorganic semiconductors.¹ In organic solids, molecules are bonded through van der Waals force, which is in contrast to inorganic materials consisting of chemically bonded atoms. The large dielectric constant (usually >10) of inorganic semiconductors lead to a small exciton binding energy on the order of 5-10 meV. Therefore, the Wannier-Mott excitons in inorganics can dissociate at room temperature. The organic materials, however, have low dielectric constant around 3, resulting in tightly bonded electron-hole pair, the Frenkel exciton, with large binding energy. Due to the charge transport mechanism of polaron hopping, organics exhibit much lower mobility than the inorganics. On the other hand, organic materials show advantage in their much higher absorption coefficient. This section will explain the properties of organic semiconductors in detail and the advantage of these unique characteristics in applications.

Table 1.1 Comparison of properties of inorganic and organic semiconductors.

<i>Property</i>	<i>Inorganic</i>	<i>Organic</i>
<i>Bond Type</i>	covalent/ionic	van der Waals
<i>Exciton</i>	Wannier-Mott	Frenkel
<i>Exciton Binding Energy</i>	$\sim 5-10$ meV	$\sim 500-1000$ meV
<i>Absorption Coefficient</i>	10^3-10^4 cm ⁻¹	10^5-10^6 cm ⁻¹
<i>Charge Transport</i>	band transport	polaron hopping
<i>Charge Mobility</i>	~ 1000 cm ² /V·s	≤ 1 cm ² /V·s
<i>Dielectric Constant</i>	10-15	2-3

1.1.1 Organic Molecules

Organic semiconductors are composed of organic molecules that are mainly made up by carbon and hydrogen atoms, with a few other elements such as oxygen, nitrogen, sulfur and halogens. The organic materials employed in optoelectronics applications are generally classified into two categories: small molecules and polymers. The small molecules are single-unit molecules with well-defined and relatively small molecular weights. They can be deposited by either vapor deposition or solution processes. Figure 1.1 shows examples of two typical types of organic small molecules, the fullerene molecule C_{70} and the non-fullerene molecule BT-CIC. In contrast, polymers are composed of repeating units along a chain and have large and uncertain molecular weights, which can only be deposited by solution process. An example of a widely used polymer PCE-10 is shown in Fig 1.1.

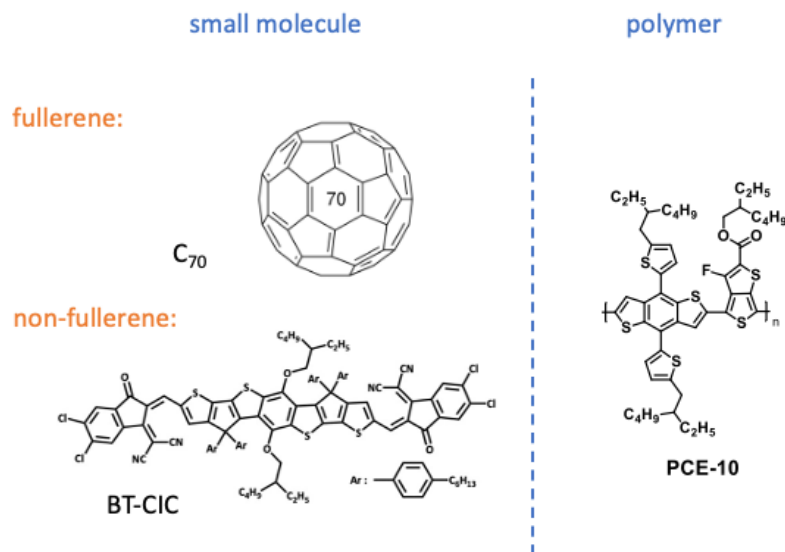


Figure 1.1 Examples of organic molecules.

Chemical structures of small molecules C_{70} and BT-CIC, and polymer PCE-10.

In contrast to inorganic semiconductors where atoms are mostly bonded through strong covalent or ionic bonds, the organic molecules are held together by the much weaker van der Waals force.¹⁶ Therefore, inorganic semiconductors often show charge delocalization among all

periodically arranged atoms and thus a density of states (DOS) spreading over a large bandwidth, resulting in the continuous energy band structure as shown in Fig. 1.2(a). The electronic wavefunction in organic semiconductors, however, is localized at individual molecules, leading to discrete energy levels with narrow bandwidths as shown in Fig. 1.2(b).

The electron orbitals of organic molecules can be calculated based on the Born-Oppenheimer (B-O) approximation¹⁷ which separates the electronic and nuclear components:

$$\Psi_{total} = \Psi_{el}\Psi_{vib}\sigma_{spin}, \quad (1.1)$$

where Ψ_{total} is the total wavefunction of a molecular state, Ψ_{el} is the electronic spatial wavefunction, Ψ_{vib} is the nuclear vibrational wavefunction, and σ_{spin} is the electronic spin wavefunction. Assuming that the nuclei of the molecule are relatively stationary compared to electrons, the electronic states can be solved from the eigenstates of Schrödinger's equation based on the electronic wavefunction of an N-electron system, which is the product of the one-electron wavefunctions, $\Psi_{el} = \prod_i \Psi_{el,i}$. The density functional theory (DFT) is also employed to calculate the molecular orbitals of complex systems.

Analogous to the valence band in inorganic semiconductors, the highest energy molecular orbital that contains an electron at the ground state is called the highest occupied molecular orbital (HOMO). Similarly, the lowest unoccupied MO (LUMO) is the energy level directly above the HOMO which contains no electron in the ground state is analogous to the conduction band in inorganic semiconductors. The energy offset between these two frontier orbitals is the energy gap, E_g . These frontier orbitals are highly sensitive to the molecular structures, allowing for tuning of optoelectronic properties through chemical modification.

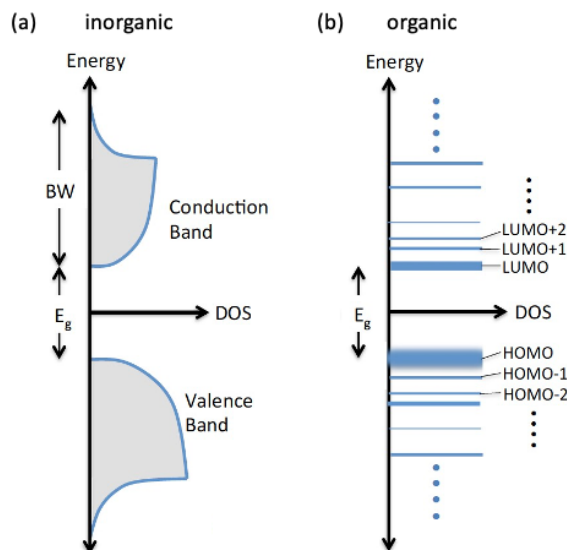


Figure 1.2 Energetic diagram of semiconductors.

Schematic illustration of (a) the energy bands of an inorganic semiconductor and (b) the energy levels of an organic semiconductor. Figure reproduced from Ref.¹

1.1.2 Excitons

Upon excitation, the distribution of electrons over the molecular orbitals changes accordingly. As illustrated in Fig. 1.3(a), the configuration of the ground state, S_0 , has all the electrons fill the orbitals up to HOMO, whereas the configuration with one of the electrons at HOMO excited to the LUMO, leaving the other electron with opposite spin at the HOMO, is known as the first singlet excited state, S_1 . The vacancy left by the excited electron is considered as a hole which carries a positive electron charge. Such a Coulombically bounded electron-hole pair is treated as a quasi-particle that can transfer energy among molecules, which is called an exciton. The Coulomb interaction between the electron and hole results in the exciton state energy lower than the E_g by the exciton binding energy, $E_B = q^2/4\pi\epsilon_r\epsilon_0r^2$, where q is the electron charge, ϵ_r is the relative dielectric constant, ϵ_0 is the vacuum permittivity and r is the exciton radius.

Depending on the magnitude of E_B , there are three types of excitons: Frenkel excitons, charge transfer (CT) excitons, and Wannier-Mott excitons, as shown in Fig. 1.3(b). The most

common excitons in organic semiconductors are Frenkel excitons where the electron-hole pair is usually confined at a single molecule, resulting in the largest binding energy > 200 meV among the three types.¹⁸ The CT excitons are shared between neighboring molecules and the electron and hole are spatially separated.¹⁹ The Wannier-Mott excitons are the most delocalized with the smallest binding energy $\ll 100$ meV,²⁰ which typically exist in the high dielectric constant inorganic semiconductors.

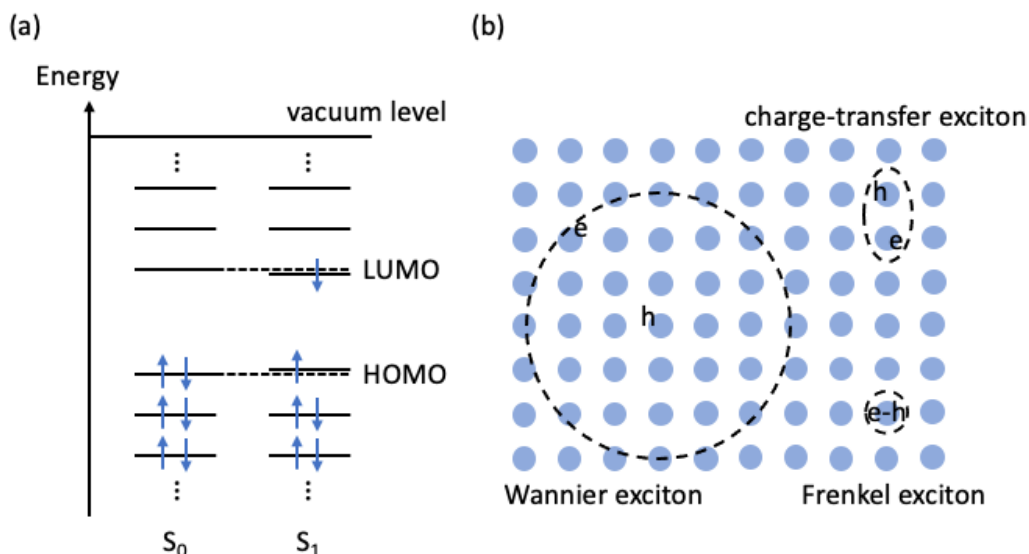


Figure 1.3 Illustration of excited state and excitons.

(a) The orbitals diagram of ground state S_0 and excited state S_1 , with arrows representing electrons with spin up and down. (b) Three different types of excitons and their characteristics.

1.1.3 Optical Properties

The optical transition, i.e., absorption and emission, between the ground and excited states is illustrated in Fig. 1.4. While the electrons are treated separately based on the B-O approximation, the vibrational motion of atomic nuclei introduces another important subset of energy levels in the ground and excited state manifolds, called the vibronic states. The configuration coordinate, Q , represents the configuration of the nuclei in the organic molecules. Based on the Franck-Condon (F-C) principle,²¹ the nuclear configuration does not change immediately upon optical transition,

the transitions between different states are vertical to the Q axis as shown in Fig. 1.4(a). As the molecules at higher vibrational levels rapidly relax to the 0th level via changes in Q , the transitions between states preferentially originate from the lowest vibrational sublevels in the manifold, resulting in the mirror-symmetry in the absorption and emission spectra of organic semiconductors as shown in Fig. 1.4(b).^{22,23} In solution or solid, an energy difference between the 0-0 transitions in absorption and emission is commonly observed due to the solvation effect from surrounding molecules. This offset is also referred to as the Stokes shift.

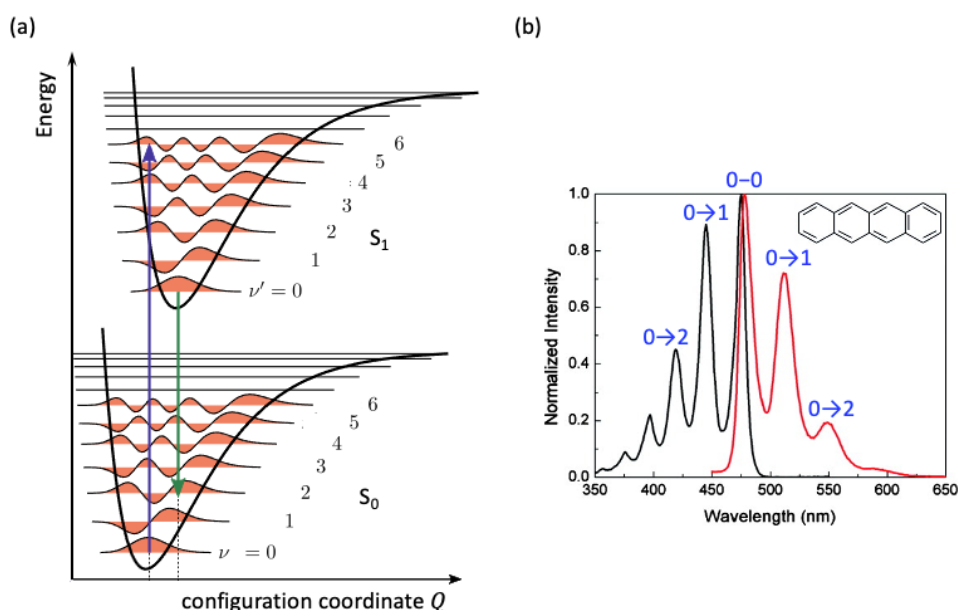


Figure 1.4 Optical transition energy diagram and spectra.

(a) Energy diagram of transition from ground state S_0 to the first singlet excited state S_1 based on Franck-Condon principle. Figure reproduced from Wikipedia: Franck-Condon principle. (b) Absorption and emission spectra of tetracene. Figure reproduced from Ref.²²

The transition rate k_{if} between an initial state Ψ_i and a final state Ψ_f is determined by Fermi's Golden Rule:²⁴

$$k_{if} = \frac{2\pi}{\hbar} |\langle \Psi_i | \widehat{H}' | \Psi_f \rangle|^2 \rho_f, \quad (1.2)$$

where ρ_f is the density of the final states. The perturbation Hamiltonian is approximated by electric dipole transition, such that $\widehat{H}' = -\boldsymbol{\mu} \cdot \mathbf{F}$, where $\boldsymbol{\mu}$ is the dipolar operator and \mathbf{F} is the optical

electric field. By inserting the total wavefunction in Eq. 1.1 to Eq. 1.2, the transition rate can be expressed as:

$$k_{if} = \frac{2\pi}{\hbar} \rho_f |\langle \Psi_{el,i} | -\boldsymbol{\mu} \cdot \mathbf{F} | \Psi_{el,f} \rangle|^2 |\langle \Psi_{vib,i} | \Psi_{vib,f} \rangle|^2 |\langle \sigma_i | \sigma_f \rangle|^2. \quad (1.3)$$

The first term in Eq. 1.3 is the electronic factor that controls the overall intensity of the transition. This integral requires opposite parity between the initial and final states to be non-zero. The value of this integral scales with the overlap between the electronic wavefunctions of the initial and final states as well as the value of the transition dipole moment $\boldsymbol{\mu}$. The second term is the vibrational factor, which is also referred to as the Franck-Condon-factor. This integral indicates that transition between two vibronic states with larger overlap has a higher probability than that with smaller overlap. The last term is the spin factor, which is non-zero only when the spins of the initial and final states are equal, therefore forbidding transitions between a triplet and a singlet state. Nevertheless, the phosphorescence from T_1 to S_0 is observed in the presence of spin-orbit coupling, in which case the spin and orbital angular momenta are coupled and only the total angular momentum needs to be conserved during the transition.² This effect can be enhanced by introducing heavy metal atoms in the molecules, which is a widely used strategy to achieve highly efficient phosphorescent OLEDs.⁴

1.1.4 Exciton Transfer

The discussion above focuses on the dynamics of excitons within the molecule, whereas the excitons can also transfer energy between molecules. Figure 1.5 illustrates the three types of exciton transfer in organic semiconductors: Dexter transfer, Förster transfer, and radiative energy transfer.

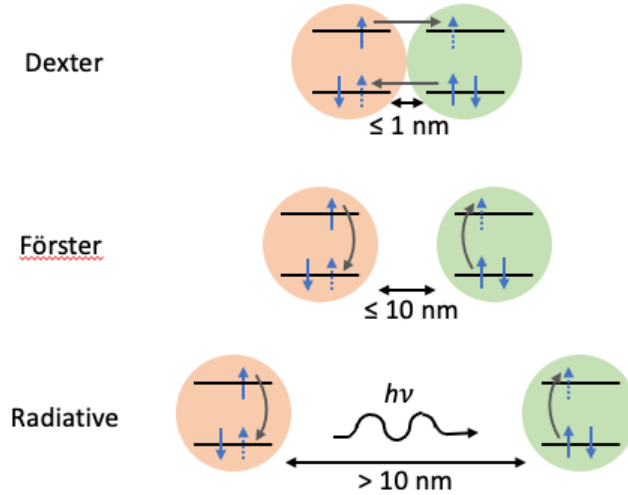


Figure 1.5 Three types of exciton energy transfer.

Three types of exciton energy transfer in organic semiconductors: the near-field energy transfer Dexter and Förster transfer, and the far-field radiative energy transfer.

Dexter transfer, as shown in Fig. 1.5, happens when two molecules are in close contact, typically within 1 nm.²⁵ The electron on the excited state of the energy donor is directly transferred onto the excited state of the acceptor, with simultaneous electron transfer between their ground states. The energy transfer rate k_{ET} of Dexter transfer as a function of the distance between donor and acceptor molecules is given as:

$$k_{ET} \propto \frac{J}{R_{DA}^2} e^{-\frac{2R_{DA}}{L}}, \quad (1.4)$$

where R_{DA} is the distance between the molecules, J is the spectral overlap between donor emission and acceptor absorption, and L is the effective average orbital radius.

Förster transfer, also known as the fluorescent resonant energy transfer (FRET), originates from the non-radiative resonant dipole-dipole coupling.²⁶ The transfer rate is derived from Fermi's golden rule with Coulomb interactions:

$$k_{ET} = \frac{1}{\tau_D} \left(\frac{R_0}{R_{DA}} \right)^6, \quad (1.5)$$

where τ_D is the exciton lifetime of the donor molecule and R_0 is the Förster radius. When $R_{DA} = R_0$, Eq. 1.5 yields $k_{ET} = 1/\tau_D$, indicating that the Förster radius is the distance between molecules

at which energy transfer and spontaneous decay are equally probable. The Förster transfer is efficient when R_{DA} is within 10 nm, which is longer than Dexter transfer distance.

In addition to the two types of near-field energy transfer, the third type is far-field radiative energy transfer through photon emission from the donor, which is subsequently absorbed by the acceptor. The radiative energy transfer can occur at distances of hundreds of nanometers.

1.1.5 Electronic Properties

In contrast to inorganic semiconductors where charge experiences coherent band transport, a charge is localized on a single molecular site in organics. In organic semiconductors, the electron-phonon interaction overwhelms the charge exchange interactions, leading to enhanced charge scattering and thus charge localization. In the limit that the charge is scattered at each molecular site such that the charge mean free path is similar to the distance between molecules, the charge transport becomes incoherent and hopping transport takes over band transport. The charged molecule also influences its neighbors through polarization effect, and the local polarization moves together with the charge. Thus, the charge forms a small polaron which is the combination of charge and polarization, and charge transport occurs via inter-site polaron hopping.^{27,28} The polaron hopping transport in organic semiconductors leads to much lower charge mobility compared to inorganics.

1.1.6 Advantages of Organic Optoelectronics

Owing to their unique properties, organic semiconductors provide distinct advantages in their application in optoelectronic devices. First of all, the non-toxic nature of the materials as well as the byproducts during fabrication makes organic electronic devices *environment compatible*. In

addition, organic materials can be deposited with vacuum deposition or solution processes at room temperature, thus lowering the energy consumption compared to conventional semiconductors such as Si that require high temperature processing.

Moreover, organic materials are soft and fragile due to the weak intermolecular van der Waals force, which makes it possible for deposition over *large areas* on a variety of *flexible* substrates. Such properties give rise to the high throughput, roll-to-roll (R2R) manufacturing of organic optoelectronic devices, as shown in Fig. 1.6(a),²⁹ which can reduce the production cost.³⁰

Furthermore, organic semiconductors can allow for transparency across the visible spectrum with selective absorption in the near-infrared (NIR) due to their relatively narrow excitonic absorption spectra, leading to *semitransparent* devices that have wide application in building integrated photovoltaics (BIPVs).^{31–33} Figure 1.6(b) shows a photo of a prototype semitransparent OPV (ST-OPV) module, Chapters 6 and 7 will provide further discussion on the realization of scalable ST-OPVs.

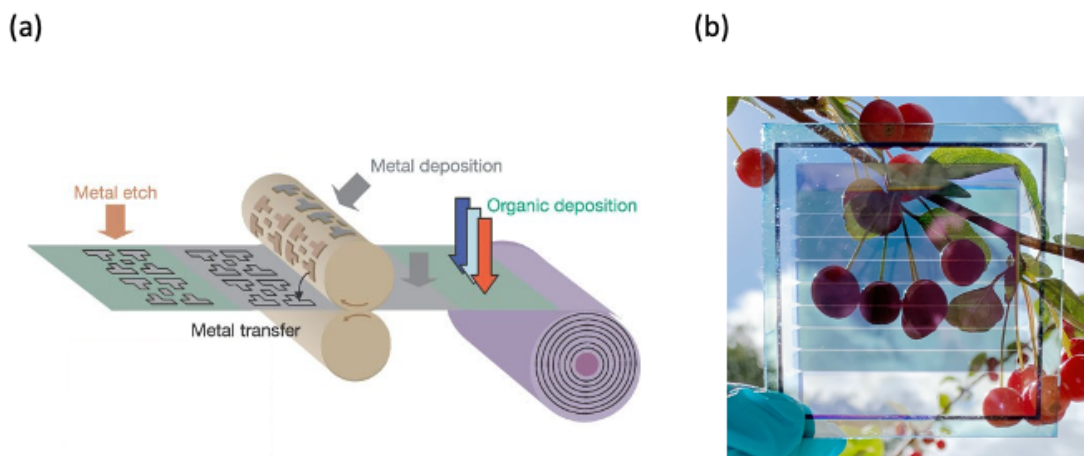


Figure 1.6 Advantages of organic optoelectronic devices.

(a) Roll-to-roll (R2R) manufacturing of organic electronic devices due to their capability of deposition over large area and flexible substrates. Figure reproduced from Ref. ²⁸ (b) Photo of a semitransparent organic photovoltaic (ST-OPV) module.

1.2 Fundamentals of Organic Photovoltaics

With continuously growing demand in energy consumption, shifting from fossil fuels to renewable energy sources has become an essential step to avoid depletion of resources and detrimental influences on the global environment. Among all renewable energy technologies, photovoltaic (PV) technology that transfers solar energy to electronic energy is one of the most promising solutions. With the vast success of OLED, OPVs are attracting increasing attention from the PV industry for their potential application in low cost, large area solar panels with transparency across the visible spectrum. This section will briefly review the fundamental concepts of OPVs from operation principles to devices architectures, and introduce the concept of the ternary OPV, a widely used strategy to improve OPV performance.

1.2.1 Basics of OPV Operation

An essential element to the photocurrent generation in OPVs is the heterojunction (HJ) between organic molecules. As the Frenkel exciton generated by light absorption has a large binding energy that prevents the separation of charge carriers, a type-II heterojunction between organic molecules with different HOMO and LUMO levels is employed in the photoactive region to assist exciton dissociation. The molecule with shallower energy levels (relative to vacuum level) is called a donor (D) molecule as it will give away an electron during photogeneration, whereas the molecule with deeper energy level is called an acceptor (A) molecule as it will receive an electron in the process. As illustrated in Fig. 1.7, the photogeneration process in an organic HJ contains four steps. The absorption of photon generates an exciton (step 1), which subsequently diffuses towards the D-A interface (step 2). At the HJ interface, the electron tends to occupy the LUMO of the acceptor while the hole prefers the HOMO of the donor due to the energy offset

between donor and acceptor molecules, resulting in exciton dissociation. At this step, the electron and hole are spatially separated on two neighboring molecules while still bound by Coulomb interactions, forming a bonded polaron pair (PP), also known as the CT state (step 3), which can either dissociate to contribute to photocurrent, or recombine. At the last step, the bonded PP is dissociated into free charge carriers which will be collected by corresponding electrodes (step 4).

The external quantum efficiency (EQE), defined by the number of charges collected at electrode per incident photon, is the product of the efficiency of these four steps:

$$\eta_{EQE} = \eta_A \eta_{ED} \eta_{CT} \eta_{CC}, \quad (1.6)$$

where η_A is the absorption efficiency, η_{ED} is the exciton diffusion efficiency, η_{CT} is the charge transfer efficiency and η_{CC} is the charge collection efficiency.

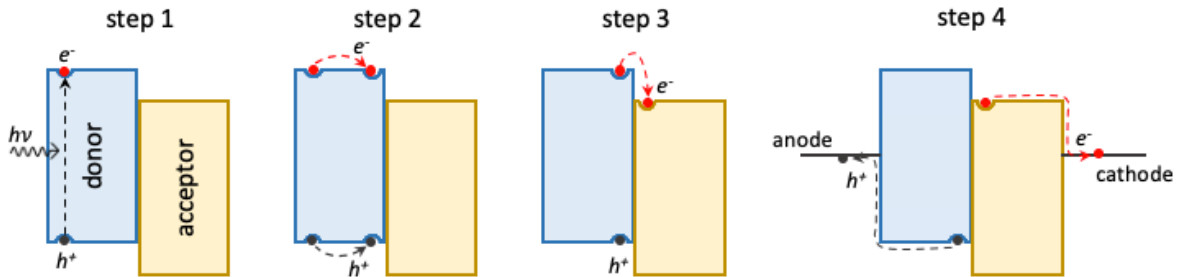


Figure 1.7 Schematic illustration of photogeneration at organic heterojunction.

Step 1: exciton generation upon photon absorption. Step 2: exciton diffusion to heterojunction (HJ) interface. Step 3: exciton dissociation into bonded polaron pair, also known as charge transfer state. Step 4: dissociation into free charge and collected by electrodes.

Based on the generation, dissociation and recombination of PPs, a generalized ideal diode equation for organic HJs was derived by Giebink et al.³⁴ with the processes illustrated in Fig. 1.8. The density of PPs is ζ , and ζ_{eq} is the density of PPs at thermal equilibrium. The excitons diffuse to the HJ to form PPs at a rate of J_X/a_0 , with exciton flux J_X and the electron-hole separated by distance a_0 . The PPs recombine to the ground state at a rate of k_{ppr} , or dissociate into free charges at a rate of k_{ppd} . The current density J contributes to the free carrier density, n_l and p_l , at the HJ

interface at a rate of J/qa_0 (q is the electron charge), whereas the free carriers recombine to form PPs at a rate of k_{rec} .

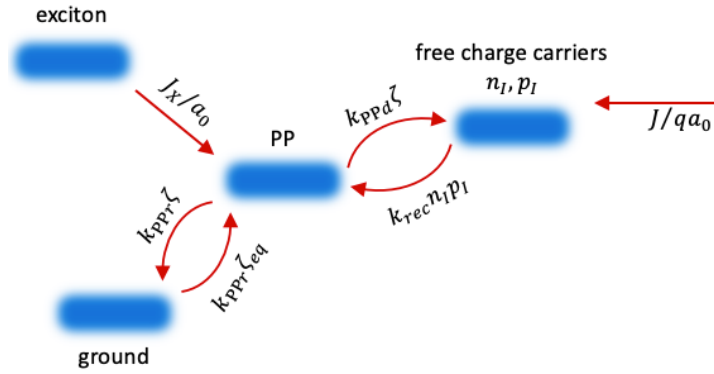


Figure 1.8 Processes at organic heterojunctions.

Schematic of the processes related to polaron pairs occurring at organic heterojunction.

Figure reproduced from Ref.³³

At steady state, the density of PPs and free carriers does not change, therefore the processes can be described via:

$$\frac{J_x}{a_0} - k_{PPr}(\zeta - \zeta_{eq}) - k_{PPd}\zeta + k_{rec}n_I p_I = 0, \quad (1.7)$$

and

$$\frac{J}{qa_0} + k_{PPd}\zeta - k_{rec}n_I p_I = 0. \quad (1.8)$$

Solving Eqs. (1.7) and (1.8) yields the ideal diode equation of organic HJs in the absence of traps:

$$J = J_{s0} \left[\exp(qV_a/k_B T) - \frac{k_{PPd}}{k_{PPd,eq}} \right] - q\eta_{PPd} J_x, \quad (1.9)$$

where V_a is the applied voltage, k_B is Boltzmann constant, T is temperature, $k_{PPd,eq}$ is k_{PPd} at thermal equilibrium, and $\eta_{PPd} = \frac{k_{PPd}}{k_{PPd} + k_{PPr}}$ is the PP dissociation probability. The first term in Eq.

(1.9) describes the dark current density with a pre-factor J_{s0} , known as the saturation dark current.

The second term is the photogenerated current.

Due to a molecular disorder in most OPVs, the DOS around the HOMO and LUMO is broadened into a Gaussian distribution, whose low-energy tail can be treated as traps, leading to ideality factor $n > 1$ and modified diode equation:

$$J = J_{SD} \left[\exp(qV_a/n_D k_B T) - \frac{k_{PPd}}{k_{PPd,eq}} \right] + J_{SA} \left[\exp(qV_a/n_A k_B T) - \frac{k_{PPd}}{k_{PPd,eq}} \right] - q\eta_{PPd} J_x, \quad (1.10)$$

where the dark saturation current J_{SD} and ideality factor n_D originates from the traps on donor materials, and J_{SA} and n_A originates from acceptors.

Furthermore, to include the influence of series resistance, R_S , Eqs. (1.9) and (1.10) can be further modified by substituting V_a with $(V_a - JR_S)$.

1.2.2 Device Architecture

In an OPV device, an organic HJ is employed in the photoactive layer to absorb light and generate photocurrent. The first successful OPV device was based on a planar HJ structure as shown in Fig. 1.9(a),³⁵ where donor and acceptor materials are deposited in sequence as separate layers. The advantage of such a planar HJ is that once the polaron pair is dissociated at the interface, the charge carriers have continuous extraction path to reach their corresponding electrodes, leading to high η_{CC} . However, the planar HJ requires that excitons generated at the donor or acceptor layer needs to diffuse to the interface. Therefore, the thickness of the photoactive layer is limited by the relatively short diffusion length of excitons to maintain a high η_{ED} , which in turn significantly reduces the absorption of the layer, η_A . Due to this limitation of the planar HJ, the blended bulk HJ (BHJ) was introduced where the donor and acceptor materials are mixed together in the photoactive layer,^{36,37} as shown in Fig. 1.9(b). The BHJ structure can simultaneously achieve high η_{ED} and η_A as the HJ interface is dispersed across the whole layer and the excitons do not need to diffuse over long distance. Compared to planar HJ, the BHJ leads to a reduced η_{CC} due to lack of continuous extraction pathways. Such deficiencies can be mitigated via optimization on morphology and thickness. Other HJ structures such as chessboard HJ and planar-mixed HJ have

also been demonstrated and investigated,³⁸ while the BHJ is the most widely employed structure owing to its simple fabrication process and high efficiency.

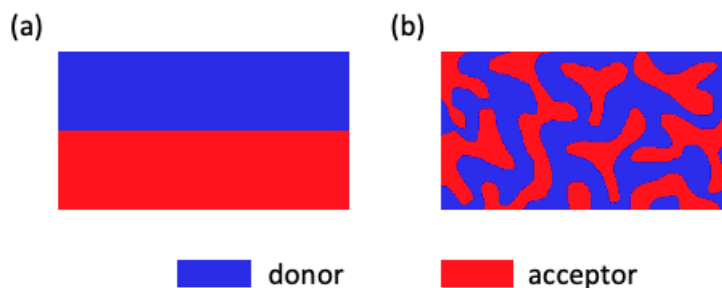


Figure 1.9 Two types of organic heterojunction (HJ) architectures. Schematics of (a) planar HJ and (b) bulk HJ (BHJ).

The typical structure of a single-junction OPV device has the photoactive layer sandwiched between buffer layers and electrodes, as shown in Fig. 1.10(a). The substrate is typically highly transparent glass or plastic. The electrodes are used to collect the photogenerated charges. The bottom electrode needs to be transparent to ensure that maximum amount of incident illumination reaches the active layer. Transition metal oxides such as indium tin oxide (ITO) are widely employed as this electrode owing to high transparency and low resistance, while efforts have also been made to develop other transparent electrode materials.³⁹ The choice for the top electrode depends on the application. Typical opaque devices employ thick metal layers to ensure high conductivity as well as reflectivity of unabsorbed light back to the photoactive layer for absorption, whereas semitransparent devices require transparent top electrode whose deposition and treatment method is non-destructive to the underlying organic layers. The buffer layers are also known as the charge transporting layers since they transport certain type of charge carrier while blocking the other type, as shown in the energy diagram in Fig. 1.10(b). Therefore, an electron transporting layer (ETL) at the cathode side and a hole transporting layer (HTL) at the anode side help guide the photogenerated charges to corresponding electrodes. Besides transporting charges, the buffer layer may also serve as exciton blocking layers to confine excitons in the photoactive layer, and

can protect the photoactive layer from subsequent deposition, especially to prevent penetration from metal deposition.

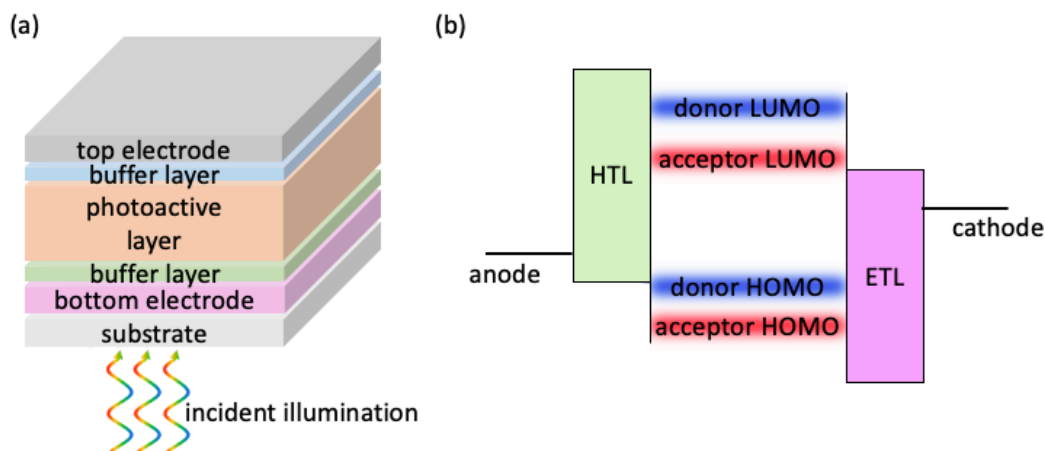


Figure 1.10 Typical structure of single-junction organic photovoltaic (OPV) device.

(a) Schematic illustration of the single-junction OPV device structure. (b) Energy diagram of the OPV in (a).

The single-junction OPVs face a trade-off between photocurrent and output voltage due to the thermalization loss of the excitation by photon energies larger than the energy gap. By stacking subcells with different energy gaps into a multi-junction device, the efficiency of the OPV can exceed the thermodynamic limit of a single-junction device due to broader spectral coverage and reduced thermalization loss. Figure 1.11 illustrates an example of the tandem OPV device structure where two subcells are series-connected with a charge recombination zone (CRZ). The front subcell with a wide energy gap absorbs the high energy photons, whereas the back subcell with a narrow energy gap absorbs the low energy photons. The different charge carriers from the subcells recombine in the CRZ, which balances the current of the tandem device. An ideal CRZ should be highly transparent with good charge transport properties to reduce both the optical and electrical losses.

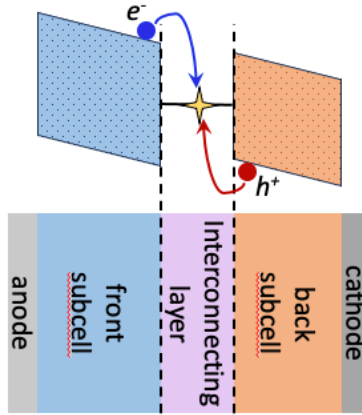


Figure 1.11 Illustration of tandem OPV structure.
 Device structure and working principle of a tandem OPV device with two series-connected subcells.

1.2.3 Device Characterization

The current density-voltage (J - V) curve and the EQE spectrum are the most important characteristics to understand the operation of a solar cell. Figure 1.12(a) shows the J - V characteristics of an OPV device. The short-circuit current density (J_{SC}), open-circuit voltage (V_{OC}) and fill factor (FF) are the three main parameters that represent the ability of the OPV to generate electric power. The J_{SC} and V_{OC} are the intercepts of the illuminated J - V curve with the J and V axes, respectively. The maximum power point (MPP) represents the maximum power (P_{max}) generated by the cell, which is defined by maximizing the area of the shaded rectangle, and FF is defined as

$$FF = \frac{J_{MPP}V_{MPP}}{J_{SC}V_{OC}}. \quad (1.11)$$

Here J_{MPP} and V_{MPP} are the J and V at the MPP. Therefore, the PCE of OPV is described via:

$$PCE = \frac{P_{max}}{P_{inc}} = \frac{J_{SC} \times V_{OC} \times FF}{P_{inc}}, \quad (1.12)$$

where P_{inc} is the incident power. A widely used standard reference solar spectrum is AM1.5G at $P_{inc} = 100 \text{ mW/cm}^2$.

The photocurrent, J_{ph} , is the difference between the illuminated current and dark current. As the dark current is zero at zero voltage bias, J_{SC} is also the J_{ph} generated at zero bias, which can be calculated by integrating the EQE of the solar cell over solar spectrum, such that:

$$J_{SC} = q \int \eta_{EQE}(\lambda) \phi_{sun}(\lambda) d\lambda, \quad (1.13)$$

where $\phi_{sun}(\lambda)$ is the solar spectral photon flux density. The example of the EQE spectrum of an OPV device is shown in Fig. 1.12(b), which is acquired by measuring the photocurrent generated by the OPV under monochromated light.

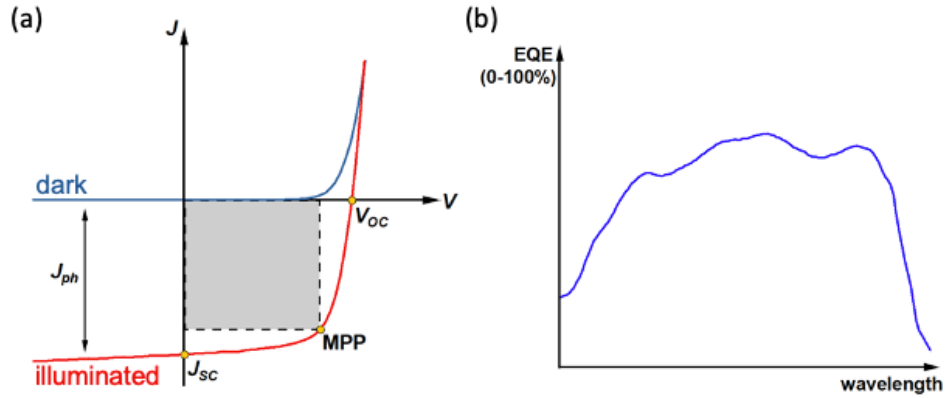


Figure 1.12 Characteristics of OPV devices.

(a) Current density-voltage (J - V) characteristics of OPV. (b) External quantum efficiency (EQE) of OPV.

It should be noted that the integral method generally provides a more accurate J_{SC} compared to J - V measurements under a solar simulator. The mismatch arises from the spectral mismatch between the solar simulator, a Xe lamp with appropriate optical filter, and the AM1.5G spectrum. Therefore, it is important to calibrate the source lamp with a reference detector. The spectral mismatch factor, M , is given by:

$$M = \frac{\int_{\lambda_1}^{\lambda_2} E_{sim}(\lambda) S_{test}(\lambda) d\lambda \int_{\lambda_1}^{\lambda_2} E_{ref}(\lambda) S_{ref}(\lambda) d\lambda}{\int_{\lambda_1}^{\lambda_2} E_{ref}(\lambda) S_{test}(\lambda) d\lambda \int_{\lambda_1}^{\lambda_2} E_{sim}(\lambda) S_{ref}(\lambda) d\lambda}, \quad (1.14)$$

where $E_{sim}(\lambda)$ and $E_{ref}(\lambda)$ are the irradiance spectra of the solar simulator and reference spectrum, $S_{test}(\lambda)$ and $S_{ref}(\lambda)$ are the spectral responsivities of the tested OPV cell and the

reference Si detector. These parameters can be clearly understood with the illustration in Fig. 1.13. When the solar simulator is calibrated by the reference detector so that it has same photocurrent under the simulator as under reference spectrum, the J_{SC} measured under the simulator, $J_{SC, sim}$, can be calibrated to the $J_{SC, ref}$ under reference illumination via:

$$J_{SC, ref} = \frac{J_{SC, sim}}{M}. \quad (1.15)$$

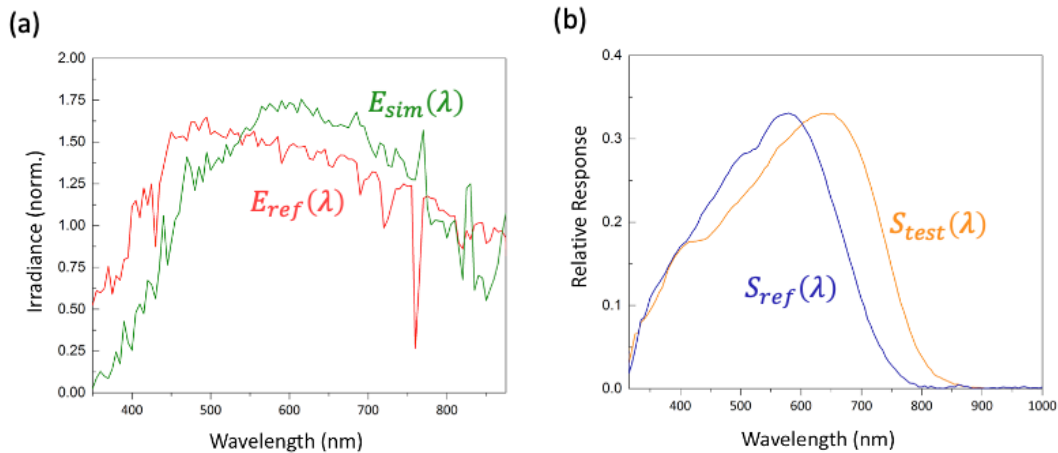


Figure 1.13 Calibration of solar simulator source with a reference detector.

(a) Irradiance of the solar simulator of filtered Xe lamp and reference AM1.5G spectra. (b) Relative responsivity of reference Si detector and tested photovoltaic device. Figure reproduced from Ref.¹

1.2.4 Advantage of OPVs: Semitransparent OPVs

Despite the high efficiency achieved by OPV, they are not competitive in the solar industry when compared to low-cost Si solar panel (< 0.30 \$/W_p). Therefore, to realize the successful commercialization of OPVs, it is important to identify the appropriate niche for OPVs that distinguishes them from incumbent solar technologies.^{40,41} As discussed in the previous section, the unique feature of narrow excitonic absorption spectra of organic semiconductors allows for transparency across the visible spectrum while selectively absorbing in the NIR, making them ideal for applications as power generating windows in the BIPV industry.

As illustrated in Fig. 1.14(a), the device structure of ST-OPVs comprises transparent electrodes, a BHJ and charge transporting layers, as well as optical coatings. Figure 1.14(b) is a summary of light utilization efficiency (LUE = PCE x APT) vs. average photopic transmission (APT) of various of solar technologies.⁴² The solid lines represent the thermodynamic limit of semitransparent PVs⁴³ as well as the calculated performance as a function of energy loss, E_{loss} , which is the energy difference between qV_{OC} and the lowest energy of absorbed photons. The calculations assume that the absorption is unity outside the visible region and (1-APT) inside the visible range. The figure shows that increased APT leads to larger LUE, indicating that the wavelength-selective absorption of OPVs allows for improvement in APT without sacrificing efficiency. Owing to their unique absorption properties, OPVs are leading the record LUE = 5%,⁴⁴ which surpasses both inorganic and perovskite based semitransparent PVs.

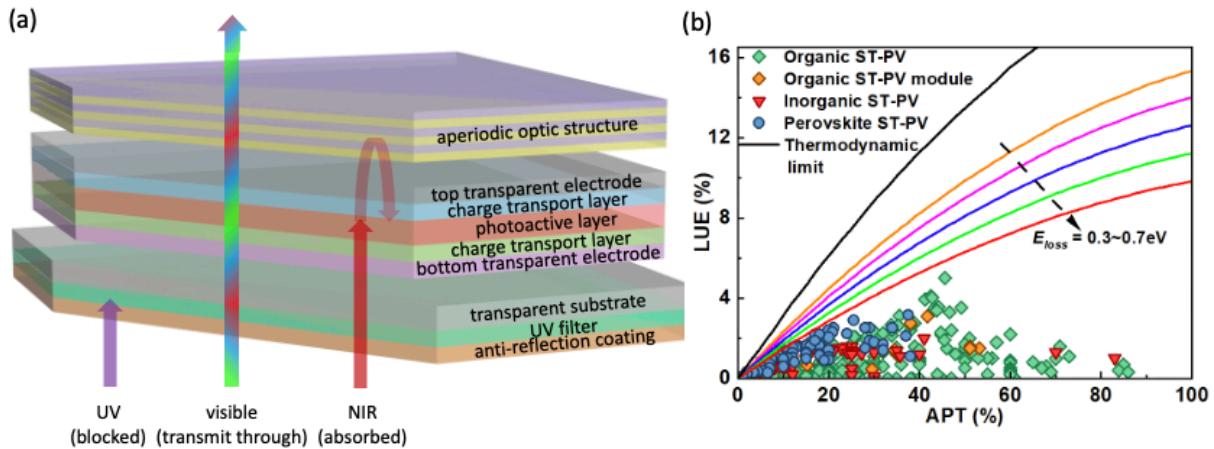


Figure 1.14 Structure and performance of ST-OPVs.

(a) Schematic illustration of the layered structure of ST-OPVs with optical coatings. (b) Calculation of ST-PV performances and comparison between ST-OPV and other ST-PV technologies.

To realize ST-OPVs for power generating windows, it is important to demonstrate high efficiency as well as acceptable aesthetics, which depend on the development of NIR-absorbing materials and optimal design of optical structures. Ideally, the photoactive layer should comprise molecules with intense and narrow NIR absorption and low binding energy, E_B , while maintaining

appropriate frontier orbital energy offsets, ΔE_{LUMO} and ΔE_{HOMO} , between donor and acceptor for efficient charge dissociation. To enhance visible transmission and NIR absorption, a reflecting mirror should be integrated to the distal interface to reflect NIR light that is not absorbed in the first pass through BHJ, as well as an outcoupling structure to improve APT and shape the transmission spectrum. In addition, an antireflection coating on the substrate surface facing the sun can maximize light coupling into the BHJ, and an ultraviolet (UV) filter can protect organic materials from detrimental high energy photons.¹⁵

1.2.5 Ternary Organic Photovoltaics

As discussed above, the efficiency of a single-junction OPV comprising one donor and one acceptor material is limited by the trade-off between J_{SC} and V_{OC} . As the BHJ absorbs photons with energy higher than the energy gap, decreasing the energy gap can broaden the absorption and benefit J_{SC} . In contrast, V_{OC} is limited by the offset between donor HOMO and acceptor LUMO, which decreases with reduced energy gap. Despite the multi-junction strategy described above, another simple approach to overcome this constraint is introducing a third component in the BHJ to create a ternary OPV, as shown in Fig. 1.15(a). The third component in the ternary BHJ acts as an additional donor or acceptor, leading to broader absorption, as shown in Fig. 1.15(b), without sacrificing V_{OC} . In addition, the third component adjusts the aggregation properties of the ternary blend. Examples of the third molecular species lying at the donor-acceptor interfaces embedded in the domain of another component, and forming independent domains is shown in Fig. 1.15(c).⁴⁵ The tunability to optimize film morphology leads to reduced energy loss and facilitated charge extraction. With these advantages, the PCE of single-junction ternary OPVs has steadily improved to approach 20%.^{9,13}

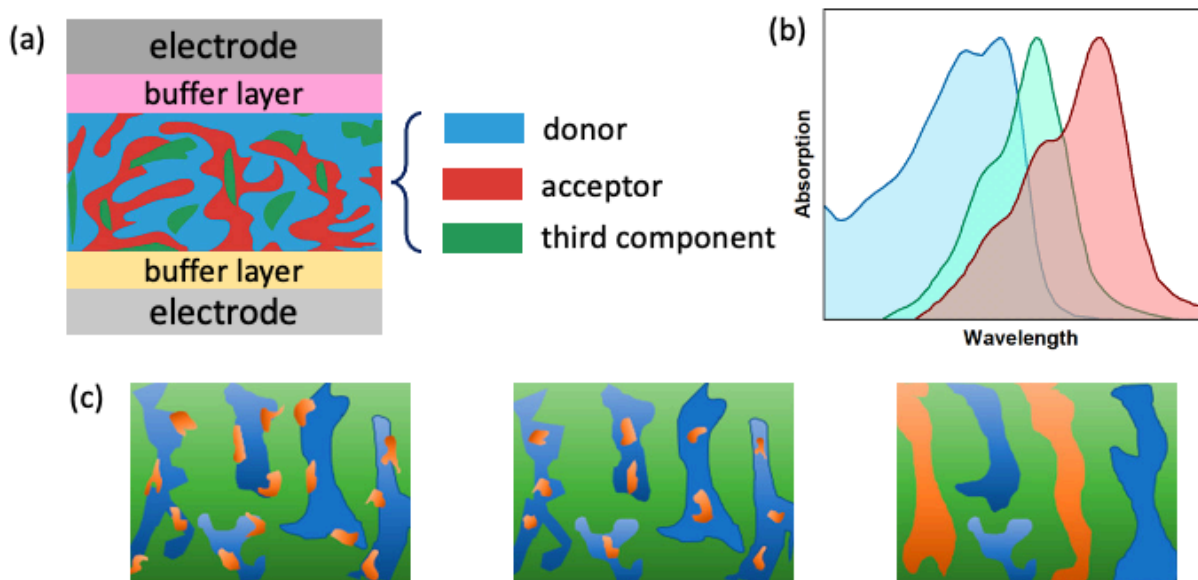


Figure 1.15 Concept and properties of ternary OPV.

(a) Device structure of OPV with a ternary blend BHJ. (b) Absorption spectra of three components in ternary OPV. (c) Examples of different morphologies of ternary BHJ with the third component located at the donor-acceptor interface, embedded within in the domain of donor or acceptor, and forming separate domain (left to right). Figure reproduced from Ref.⁴⁵

Compared to binary OPVs where the photogeneration occurs between one donor and one acceptor, the working mechanism of ternary OPV is more complicated due to the existence of an additional donor or acceptor species. Figure 1.16 illustrates the four prominent models for charge generation, namely the charge transfer, energy transfer, parallel and alloy model, of ternary OPVs^{46–49} with the example of two donors and one acceptor. The situation with one donor and two acceptors works similarly.

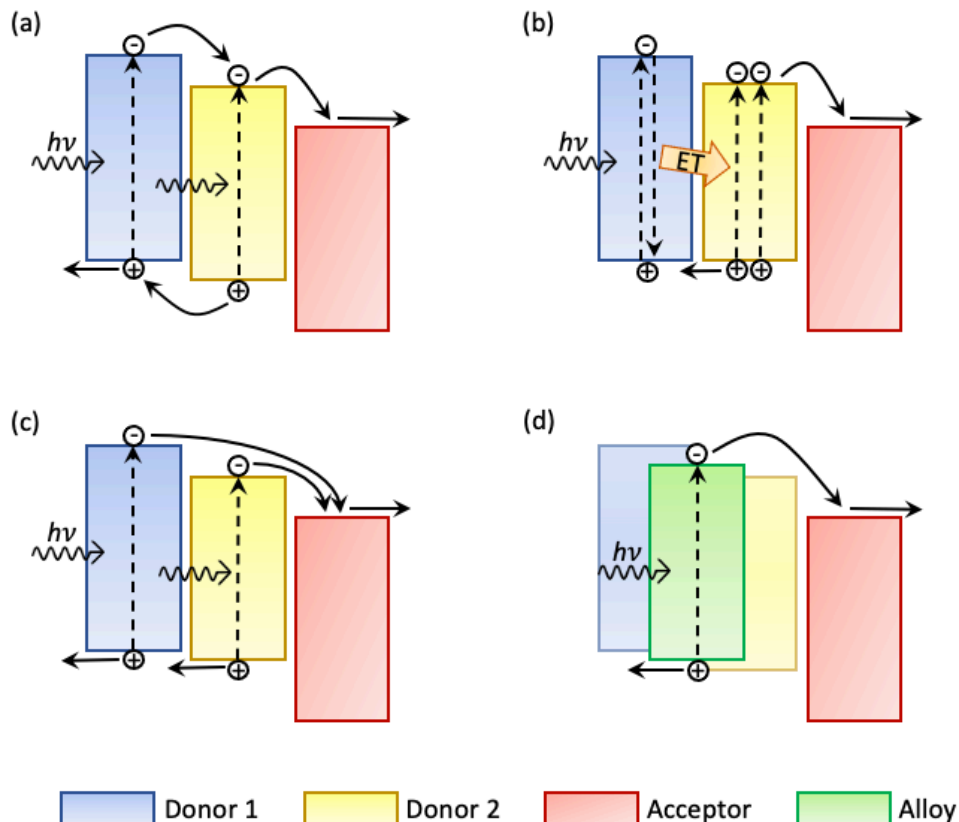


Figure 1.16 Current models of ternary OPVs.

Energy diagram of current models of photogeneration in ternary OPVs. (a) Charge transfer model. (b) Energy transfer model. (c) Parallel model. (d) Alloy model.

In the cases where the charge transfer mechanism dominates, the three components in the ternary BHJ have energy levels in cascade alignment. As shown in Fig. 1.16(a), both donors contribute to charge generation at interfaces between donor and acceptor or between donor 1 and donor 2, whereas donor 2 molecules act as charge transfer intermediate. Holes generated at or transferred to its HOMO will be subsequently transferred to the HOMO of donor 1. Similarly, electrons on its LUMO will be transferred to the acceptor LUMO. Such ternary BHJs require blend morphology where donor 2 molecules are located at the interfaces of donor 1 and acceptor molecules to provide efficient charge transfer, as illustrated in Fig. 1.15(c). The V_{OC} of such a ternary OPV is pinned at the lower binary V_{OC} (donor 1-acceptor binary V_{OC}) independent of the

blend ratio as only the HOMO of donor 1 and LUMO of acceptor carries the electrons and holes to be collected at electrodes.

The energy transfer model illustrated in Fig. 1.16(b) has one component acting as an absorber and transfers energy to other chromophores. While both donors absorb light and generate excitons, only excitons at donor 2 dissociate and generate free charge carriers, whereas the excited state at donor 1 transfers energy through Dexter or Förster transfer to excite donor 2 and return to the ground state. Similar to the charge transfer mechanism, in the energy transfer model only two components (donor 2 and acceptor) participate in the charge percolation and extraction, resulting in a constant V_{OC} independent of blend ratio.

The parallel model assumes that the ternary OPV is composed of two binary subcells, donor 1-acceptor and donor 2-acceptor, which work independently and contribute to the performance as parallel-connected diodes. As shown in Fig. 1.16(c), the two donors have their independent charge transport channels, requiring interfaces with the acceptors of both donor molecules. As a consequence of the parallel-connected circuit, the photocurrent generation of the ternary OPV is the sum of two constituent binary diodes, which is the weighted average of the J_{sc} of corresponding binary OPVs based on the composition of the ternary blend.⁵⁰ In addition, the V_{OC} of the ternary OPV is between those of binary cells and varies with the proportion of the blend constituents.

In contrast to the previous three models where charge transfer happens between the energy levels of the three components, the fourth mechanism, the alloy model, proposes that the two similar components form an organic alloy, or a molecular alloy, with new energy levels that are between those of the two components. As shown in Fig. 1.16(d), the exciton generation and charge transfer happen on the new energy levels of the donor alloy. The energy levels of the alloy, and thus V_{OC} of the ternary OPV, is a function of the ratio between the two donors, analogous to an

inorganic semiconductor alloy. Although this organic alloy formation has been claimed in many ternary BHJs, well-defined criteria of such molecular alloy, as well as clear evidence of the emergence of new energy levels and CT states are still missing, which will be further discussed in Chapter 2.

1.3 Organization of the Thesis

Since the invention of ternary BHJs, ternary OPVs have become one of the most widely employed strategies to improve efficiency. The major goal of this thesis is to investigate the device physics of ternary OPVs and explore their applications in high efficiency and scalable OPV devices. Chapter 2 focuses on the validity of the concept of a molecular alloy, which has been frequently mentioned in ternary OPVs while lacking clear and uniform definition in the past. We propose the criteria that a molecular organic alloy should meet and the procedure to identify its formation to avoid ambiguity. Specifically, the optoelectronic properties of a ternary OPV system are investigated, which indicate the absence of an organic alloy in the BHJ. In Chapter 3, an end-capping exchange reaction between archetype non-fullerene acceptors (NFAs) is found to occur during device fabrication. It influences the reproducibility and reliability of ternary OPV devices comprising one donor and two NFAs. This discovery unlocks new insights to understand the working mechanism of ternary OPVs. Chapter 4 provides further study on the impact of the dipolar reaction products on the dielectric properties and performance of ternary OPVs over time. The results suggest that dipolar molecules in organic electronic devices can negatively impact their operational stability. Chapter 5 moves to the application of ternary OPVs in high efficiency solar cells. A ternary subcell is employed to improve the PCE of a tandem device due to the extended absorption in the near-infrared (NIR). Chapters 6 and 7 focus on the scalability of ST-OPV devices,

which is an essential step towards commercialized products. Chapter 6 investigates the resistance loss when scaling OPV devices. Ultrafine metal grids are designed and realized to reduce the series resistance and achieve an ST-OPV module with minimal PCE loss. Another considerable loss channel in an OPV module is the large interconnection area between constituent cells due to lack of non-destructive, high-resolution patterning method. Chapter 7 introduces a multilevel peel-off method that can realize micron-scale patterning over a large device area. Compared to the state-of-art laser ablation method, the peel-off patterning achieves equally high resolution while avoiding the potential damage to organic materials. With the peel-off method, a ternary BHJ-based high efficiency ST-OPV module was fabricated with geometric fill factor over 95%. Lastly, we summarize the unsolved issues in ternary OPVs and provide an outlook on the applications of OPVs in the BIPV industry in Chapter 8.

Chapter 1

Bibliography

1. Forrest, S. R. *Organic Electronics: Foundations to Applications*. (Oxford University Press, 2020).
2. Köhler, A. & Bässler, H. *Electronic processes in organic semiconductors: An introduction*. (Wiley-VCH Verlag, 2015).
3. Tang, C. W. & Vanslyke, S. A. Organic electroluminescent diodes. *Appl. Phys. Lett.* **51**, 913–915 (1987).
4. Baldo, M. A. *et al.* Highly efficient phosphorescent emission from organic electroluminescent devices. *Nature* **395**, 151–154 (1998).
5. Kamtekar, K. T., Monkman, A. P. & Bryce, M. R. Recent Advances in White Organic Light-Emitting Materials and Devices (WOLEDs). *Adv. Mater.* **22**, 572–582 (2010).
6. D’Andrade, B. W. & Forrest, S. R. White Organic Light-Emitting Devices for Solid-State Lighting. *Adv. Mater.* **16**, 1585–1595 (2004).
7. Hong, G. *et al.* A Brief History of OLEDs—Emitter Development and Industry Milestones. *Adv. Mater.* **33**, 2005630 (2021).
8. Adachi, C., Baldo, M. A., Thompson, M. E. & Forrest, S. R. Nearly 100% internal phosphorescence efficiency in an organic light-emitting device. *J. Appl. Phys.* **90**, 5048–5051 (2001).
9. Zhan, L. *et al.* Manipulating Charge Transfer and Transport via Intermediary Electron Acceptor Channels Enables 19.3% Efficiency Organic Photovoltaics. *Adv. Energy Mater.* **12**, 2201076 (2022).
10. Meng, L. *et al.* Tandem organic solar cells with efficiency over 19% via the careful

- subcell design and optimization. *Sci. China Chem.* **66**, 808–815 (2023).
11. Zheng, Z. *et al.* Tandem Organic Solar Cell with 20.2% Efficiency. *Joule* **6**, 171–184 (2022).
 12. Wang, J. *et al.* A Tandem Organic Photovoltaic Cell with 19.6% Efficiency Enabled by Light Distribution Control. *Adv. Mater.* **33**, 2102787 (2021).
 13. Cui, Y. *et al.* Single-Junction Organic Photovoltaic Cell with 19% Efficiency. *Adv. Mater.* **33**, 2102420 (2021).
 14. Burlingame, Q. *et al.* Intrinsically stable organic solar cells under high-intensity illumination. *Nature* **573**, 394–397 (2019).
 15. Li, Y. *et al.* Non-fullerene acceptor organic photovoltaics with intrinsic operational lifetimes over 30 years. *Nat. Commun.* **12**, 1–9 (2021).
 16. Margenau, H. Van der waals forces. *Rev. Mod. Phys.* **11**, 1 (1939).
 17. Born, M. & Oppenheimer, R. Zur Quantentheorie der Molekeln. *Ann. Phys.* **389**, 457–484 (1927).
 18. Frenkel, J. On the Transformation of light into Heat in Solids. I. *Phys. Rev.* **37**, 17 (1931).
 19. Bulović, V., Burrows, P. E., Forrest, S. R., Cronin, J. A. & Thompson, M. E. Study of localized and extended excitons in 3,4,9,10-perylenetetracarboxylic dianhydride (PTCDA) I. Spectroscopic properties of thin films and solutions. *Chem. Phys.* **210**, 1–12 (1996).
 20. Wannier, G. H. The Structure of Electronic Excitation Levels in Insulating Crystals. *Phys. Rev.* **52**, 191 (1937).
 21. Lax, M. The Franck-Condon Principle and Its Application to Crystals. *J. Chem. Phys.* **20**, 1752–1760 (1952).
 22. Kasha, M. Characterization of electronic transitions in complex molecules. *Discuss.*

- Faraday Soc.* **9**, 14–19 (1950).
23. Burdett, J. J., Müller, A. M., Gosztola, D. & Bardeen, C. J. Excited state dynamics in solid and monomeric tetracene: The roles of superradiance and exciton fission. *J. Chem. Phys.* **133**, 144506 (2010).
 24. Orear, J., Fermi, E., Rosenfeld, A. H. & Schluter, R. A. Nuclear physics : a course given by Enrico Fermi at the University of Chicago. 248 (1974).
 25. Dexter, D. L. & Bovey, L. F. H. A Theory of Sensitized Luminescence in Solids. *J. Chem. Phys.* **21**, 836–850 (1953).
 26. Förster, T. 10th Spiers Memorial Lecture. Transfer mechanisms of electronic excitation. *Discuss. Faraday Soc.* **27**, 7–17 (1959).
 27. Holstein, T. Studies of polaron motion: Part II. The “small” polaron. *Ann. Phys. (N. Y.)* **8**, 343–389 (1959).
 28. Lu, N., Li, L., Geng, D. & Liu, M. A review for polaron dependent charge transport in organic semiconductor. *Org. Electron.* **61**, 223–234 (2018).
 29. Forrest, S. R. The path to ubiquitous and low-cost organic electronic appliances on plastic. *Nature* **428**, 911–918 (2004).
 30. Qu, B., Chen, Z., Lahann, L. & Forrest, S. R. Cost Estimates of Roll-to-Roll Production of Organic Light Emitting Devices for Lighting. *ACS Photonics* (2023).
doi:10.1021/ACSPHOTONICS.3C00226
 31. Lunt, R. R. & Bulovic, V. Transparent, near-infrared organic photovoltaic solar cells for window and energy-scavenging applications. *Appl. Phys. Lett.* **98**, 113305 (2011).
 32. Meiss, J., Holzmueller, F., Gresser, R., Leo, K. & Riede, M. Near-infrared absorbing semitransparent organic solar cells. *Appl. Phys. Lett.* **99**, 10–13 (2011).

33. Li, Y. *et al.* High Efficiency Near-Infrared and Semitransparent Non-Fullerene Acceptor Organic Photovoltaic Cells. *J. Am. Chem. Soc.* **139**, 17114–17119 (2017).
34. Giebink, N. C., Wiederrecht, G. P., Wasielewski, M. R. & Forrest, S. R. Ideal diode equation for organic heterojunctions. I. Derivation and application. *Phys. Rev. B* **82**, 1–12 (2010).
35. Tang, C. W. Two-layer organic photovoltaic cell. *Appl. Phys. Lett.* **48**, 183–185 (1986).
36. Yu, G., Gao, J., Hummelen, J. C., Wudl, F. & Heeger, A. J. Polymer Photovoltaic Cells: Enhanced Efficiencies via a Network of Internal Donor-Acceptor Heterojunctions. *Science* (80-.). **270**, 1789 (1995).
37. Halls, J. J. M. *et al.* Efficient photodiodes from interpenetrating polymer networks. *Nat.* *1995 3766540* **376**, 498–500 (1995).
38. Yang, F. & Forrest, S. R. Photocurrent generation in nanostructured organic solar cells. *ACS Nano* **2**, 1022–1032 (2008).
39. Cao, W., Li, J., Chen, H. & Xue, J. Transparent electrodes for organic optoelectronic devices: a review. *J. Photonics Energy* **4**, 040990 (2014).
40. Burgués-Ceballos, I. *et al.* Transparent organic photovoltaics: A strategic niche to advance commercialization. *Joule* **5**, 2261–2272 (2021).
41. Riede, M., Spoltore, D. & Leo, K. Organic Solar Cells—The Path to Commercial Success. *Adv. Energy Mater.* **11**, 2002653 (2021).
42. Li, Y. *et al.* Enhanced Light Utilization in Semitransparent Organic Photovoltaics Using an Optical Outcoupling Architecture. *Adv. Mater.* **1903173**, 1903173 (2019).
43. Traverse, C. J., Pandey, R., Barr, M. C. & Lunt, R. R. Emergence of highly transparent photovoltaics for distributed applications. *Nature Energy* **2**, 849–860 (2017).

44. Li, Y. *et al.* Color-neutral, semitransparent organic photovoltaics for power window applications. *Proc. Natl. Acad. Sci. U. S. A.* **117**, 21147–21154 (2020).
45. Zhang, Y. & Li, G. Functional Third Components in Nonfullerene Acceptor-Based Ternary Organic Solar Cells. *Accounts Mater. Res.* **1**, 158–171 (2020).
46. Günther, M. *et al.* Models and mechanisms of ternary organic solar cells. *Nat. Rev. Mater.* **2023** 1–16 (2023). doi:10.1038/s41578-023-00545-1
47. Lu, L., Kelly, M. A., You, W. & Yu, L. Status and prospects for ternary organic photovoltaics. *Nat. Photonics* **9**, 491–500 (2015).
48. Ameri, T., Khoram, P., Min, J. & Brabec, C. J. Organic ternary solar cells: A review. *Adv. Mater.* **25**, 4245–4266 (2013).
49. Fu, H., Wang, Z. & Sun, Y. Advances in Non-Fullerene Acceptor Based Ternary Organic Solar Cells. *Sol. RRL* **1700158**, 1700158 (2017).
50. Yang, L., Zhou, H., Price, S. C. & You, W. Parallel-like bulk heterojunction polymer solar cells. *J. Am. Chem. Soc.* **134**, 5432–5435 (2012).

Chapter 2

Alloy or Blend: Analysis of Ternary Organic Photovoltaics

In inorganic materials, an alloy is a mixture of two or more substances that generally exhibits electronic and/or physical properties that differ from those of its constituents. In organic systems, the formation of a “molecular alloy” comprising mixtures of molecular organic materials has also been proposed. In this chapter, we test the validity of this concept via the study of the optoelectronic properties of a ternary system that has previously been identified to form a molecular acceptor alloy, namely a blend of a P3HT donor, with two acceptors ICBA and PC₆₁BM.¹ Using photoelectron spectroscopy, we find that the ICBA:PC₆₁BM blend shows the same highest occupied molecular orbital and exciton energies as that of ICBA, indicating the absence of a new exciton state in the blend. Furthermore, charge transfer state spectra of ternary blends are found to comprise a simple linear superposition of the corresponding binaries. From these results, emergent electronic states are not found to support the existence of a molecular alloy in this system. We discuss the criteria that should be met by a molecular organic alloy and procedures needed for their unambiguous identification. To our knowledge, there is as yet no clear evidence of the existence of an alloy in any organic semiconductor system.

2.1 Criteria of Molecular Alloy

An alloy is commonly understood to be a physical mixture of two or more constituents with variable proportions that exhibits electronic and/or physical properties different from its components.² Common examples of metal alloys are steel (C + Fe) or brass (Zn + Cu). Binary semiconductors such as $\text{Si}_x\text{Ge}_{1-x}$, ternary semiconductors such as $\text{In}_x\text{Ga}_{1-x}\text{As}$, and other quaternary and quinary inorganic semiconductors are also commonly referred to as alloys.² All of these materials have optical and electrical properties that are distinct from the substances of which they are comprised. The physical properties (i.e. Young's moduli, melting points, etc.) are also different in most alloy mixtures than in their constituents.³ Their characteristics derive almost entirely from the strong chemical bonds formed between atoms in the mixtures.

In contrast to inorganic alloys comprising atomic constituents, organic materials are bonded by far weaker, electrostatic van der Waals forces. It has been proposed that in some cases these weakly bonded organic mixtures form a new substance which is called a "molecular alloy". One potential class of molecular alloys are CT salts and their solid solutions,⁴⁻⁸ another are organic eutectics.⁹⁻¹³ The formation of molecular alloys has also been claimed to be observed in disordered organic solid solutions.¹⁴ Recently, ternary blends in the active regions of OPV cells and so-called organic co-crystals have been identified to form organic alloys.^{1,15-23} Although there has been frequent mention of molecular organic alloys over many decades, to our knowledge no uniform framework has been developed to clearly define what is meant by this term, and how an organic alloy differs from chemically bonded mixtures whose electronic, optical and physical properties are not a mere extrapolation of those of the individual constituents.

A chemical bond between organic molecules commonly results in an entirely new compound, not an alloy mixture. Given the absence of chemical bonds between molecules, the

correspondence between a molecular organic alloy and alloys found in metals and inorganic semiconductors admittedly cannot be precise. The weak and electrostatic nature of van der Waals forces in molecular alloys as compared with chemical bonds in atomic alloys implies that the term alloy, itself, will have a different meaning for mixtures in these different systems. To clarify these substantially different definitions, we propose that a molecular alloy should meet with the following criteria:

1. It should be a physical mixture of two or more species of organic molecules with no chemical reaction occurring during mixture formation. The proportion of constituents can vary over a wide range.
2. It should have electron orbital interactions between different molecular species that result in modifications of electronic states that cannot be ascribed to a simple linear superposition of those inherent to the constituents.
3. The orbital interactions should lead to electronic or physical properties clearly distinguishable from those of its constituents.

Note that electron transfer between molecules needs special attention relative to Criterion 2. For example, the electron transfer in a donor:acceptor blend is driven by the energy offset between the corresponding states in the participating molecules. This does not meet the requirements of Criterion 2 if the inherent properties of the electronic states involved are left unchanged by the transfer process. The changes in electronic or physical properties mentioned in Criterion 3 are often observed. Specifically, changes in electronic properties have often been used to claim the formation of a molecular organic alloy.^{1,4,6,7,15-18,22} Also, changes in physical properties (e.g. eutectic formation) may also indicate the presence of an alloy.¹⁰⁻¹² These changes are also often the result of electronic interactions. Unfortunately, most prior studies have not provided

evidence that the other two criteria are also fulfilled.

2.2 Characterization of a Ternary OPV System

To identify the existence of molecular alloy, we investigate a ternary mixture that forms the active region of an OPV cell that has previously been claimed to be an organic alloy.¹ The ternary system comprises a donor (D) P3HT, blended with two acceptors ICBA (A_1) and PC₆₁BM (A_2).^{1,24} Evidence for the existence of an alloy between the two acceptors was based on the observed dependence of the CT state absorption energy and the V_{OC} of the OPV on the blend ratio. Although these composition-dependent electronic properties may suggest the formation of an organic alloy, investigation of the origins of the observed changes are needed to identify whether they fully meet the three criteria discussed above. Here we provide a detailed investigation of the HOMO levels, the Frenkel exciton states, and CT states of this system.

2.2.1 Experimental Methods

The ICBA/PC₆₁BM acceptor blends with ICBA weight fractions of 0, 0.2, 0.5, 0.8, 1 were dissolved in chlorobenzene (CB) at total concentration of 20 mg/mL and stirred overnight at 60°C at 300 rpm. The solutions were then spin-coated at 1000 rpm for 60s on 150 nm thick ITO on glass substrates to form 90-100nm thick acceptors films for ultraviolet photoelectron spectroscopy (UPS) measurements. The films were thermally annealed at 150°C for 60 min, 20 min, 50 min, 20 min, and 10 min, respectively. The measurements were done in an ultrahigh vacuum chamber (base pressure $< 1 \times 10^{-9}$ Torr) using the 21.22 eV He-I gas-discharge lamp emission. The spectra were collected by a hemispherical electron energy analyzer (Thermal VG) with a pass function full width half maximum (FWHM) of 0.16 eV.

The acceptor films were similarly prepared for photoluminescence (PL) measurements on quartz substrates. The samples were excited in low vacuum at wavelength $\lambda = 442$ nm using a continuous wave He-Cd laser to obtain steady-state PL. The spectra were collected using a fiber-coupled monochromator (Princeton Instruments SP-2300i) equipped with a Si charge-coupled device (CCD) (PIXIS:400). For time-resolved PL measurements, the samples were excited at $\lambda = 480$ nm using 150 fs pulses at a 1 kHz repetition rate from a Ti:sapphire laser (Clark-MXR CPA series) pumped optical parametric amplifier (TOPAS-C). The photon counts were measured using a time-correlated single photon counter (PicoHarp 300) coupled to a Si single photon avalanche detector (PDM series).

The OPV devices were grown on a solvent cleaned, 145 nm thick film of ITO, patterned into 1 mm wide stripes on a glass substrate. The ternary blends comprising P3HT:(ICBA:PC₆₁BM) of different acceptor weight ratios were separately prepared in CB at total concentration 20 mg/mL and stirred overnight at 60°C at 300 rpm. A 45 nm thick layer of PEDOT:PSS (CLEVIOS™ P VP AI 4083, filtered with a Whatman™ 0.45 μ m nylon filter w/glass micro fiber) was first spin-coated on the ITO and baked at 150°C for 30 min. Subsequently, the P3HT:(ICBA:PC₆₁BM) active layer was spin-coated in an ultrapure nitrogen environment ($O_2 < 0.1$ ppm, $H_2O < 0.1$ ppm) on top of the PEDOT:PSS at 1000 rpm for 60s to form a 90-100 nm thick film. Then the samples were transferred into a high vacuum chamber (base pressure $\sim 10^{-7}$ Torr) for Al thermal evaporation at 1Å/s to form a 100 nm thick film. The samples were transferred back to the nitrogen environment for thermal annealing at 150°C. The thermal annealing time was 10 min for 1:1:0, 20 min for 1:0.2:0.8 and 1:0.8:0.2, 40 min for 1:0.6:0.4, 50 min for 1:0.5:0.5 and 60 min for 1:0:1.²⁴ The charge transfer state electroluminescence (EL) spectra were measured under 4V forward-bias, collected using a fiber-coupled monochromator equipped with a Si CCD and an InGaAs

photoreceiver with sensitivity from $\lambda = 800$ to 1700 nm (Newport Model 2153). The EL spectra were fit with Gaussian distributions using OriginPro 2017. The V_{OC} were measured in a glovebox filled with nitrogen ($O_2 < 0.1$ ppm, $H_2O < 0.1$ ppm), using a solar simulator with a 300W Xe lamp with an AM1.5G filter, whose 1 sun intensity was calibrated with a National Renewable Energy Laboratory-traceable Si reference cell.

2.2.2 Frontier Orbitals

Figure 2.1 shows the UPS spectra of the two acceptors and their blends in the ratios of 1:4, 1:1 and 4:1. The short vertical lines in Fig. 2.1(a) indicates the emission cutoff extracted from the spectra due to the 21.2 eV He-I transition. Figure 2.1(b) shows the low-binding-energy region of the spectra. The short vertical lines show that the HOMO energy for ICBA and the blends is at -5.8 ± 0.1 eV (referenced to vacuum), and for PC₆₁BM the HOMO energy is at -6.0 ± 0.1 eV.

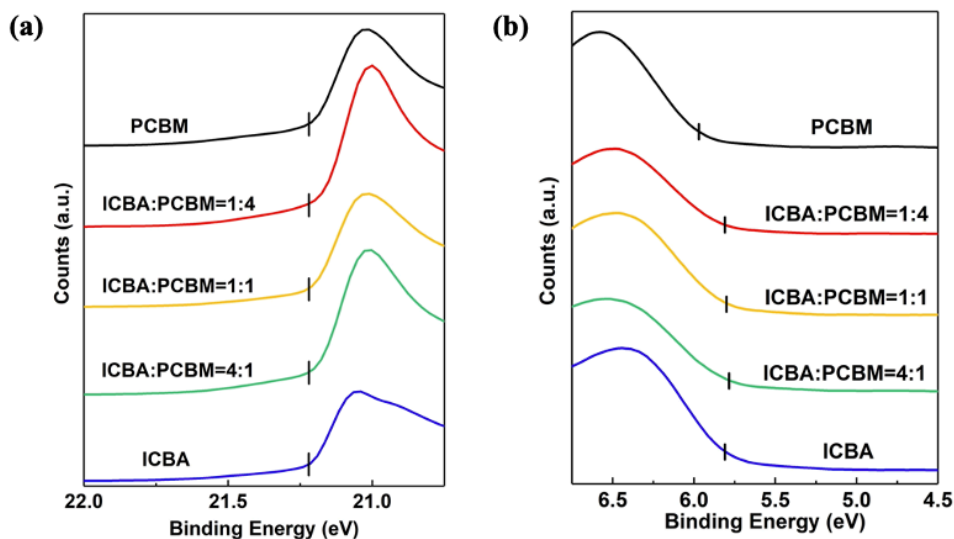


Figure 2.1 Ultraviolet Photoelectron Spectroscopy (UPS) measurements of ICBA:PC₆₁BM blends.

(a) High-binding-energy region of UPS spectra of ICBA, PC₆₁BM and their blends at ratios indicated. The short vertical lines represent the emission cutoff energies. (b) Low-binding-energy region where the short vertical lines indicate the highest occupied molecular orbital energies.

Analysis of the UPS data indicates that the HOMO levels of the acceptor blends are the same as that of ICBA, independent of the acceptor blend ratio, with no evidence found for the emergence of new ground state.

2.2.3 Exciton States

The exciton states of individual acceptors and blends are investigated with PL, with the results shown in Fig. 2.2. The normalized steady-state PL spectra are provided in Fig. 2.2(a). The dominant 0-0 transition peaks have energies of 1.66 ± 0.01 eV for ICBA, 1.70 ± 0.01 eV for PC₆₁BM, and 1.66 ± 0.01 eV for all of the blends. Also, ICBA and the blends show 0-1 transition emission at 1.60 ± 0.01 eV, and 0-2 transition peaks at 1.51 ± 0.01 eV. PC₆₁BM has its 0-1 transition at 1.55 ± 0.01 eV. Figure 2.2(b) presents the first derivatives of the normalized PL spectra to more accurately determine the peak positions. The data indicate that all acceptor blends have same peak positions as that of ICBA. To further explore whether there exists a new excitonic state, the dynamics of the exciton state recombination were studied using time-resolved PL, with results shown in Fig. 2.2(c). The transients are fit by a single exponential decay shown by solid lines, yielding exciton lifetimes of $\tau = 0.98 \pm 0.04$ ns for ICBA, $\tau = 0.94 \pm 0.04$ ns for PC₆₁BM, and $\tau = 0.95 \pm 0.04$ ns for the blend. All these decay rates are equal to within experimental accuracy.

The steady-state PL data spectra show that the exciton energies of the acceptor blends are also the same as for ICBA, nor does the exciton lifetime extracted from Fig. 2.2(c) depend on the blend ratio. Therefore, the excited states in the acceptor blends also do not appear to be influenced by the mixture composition.

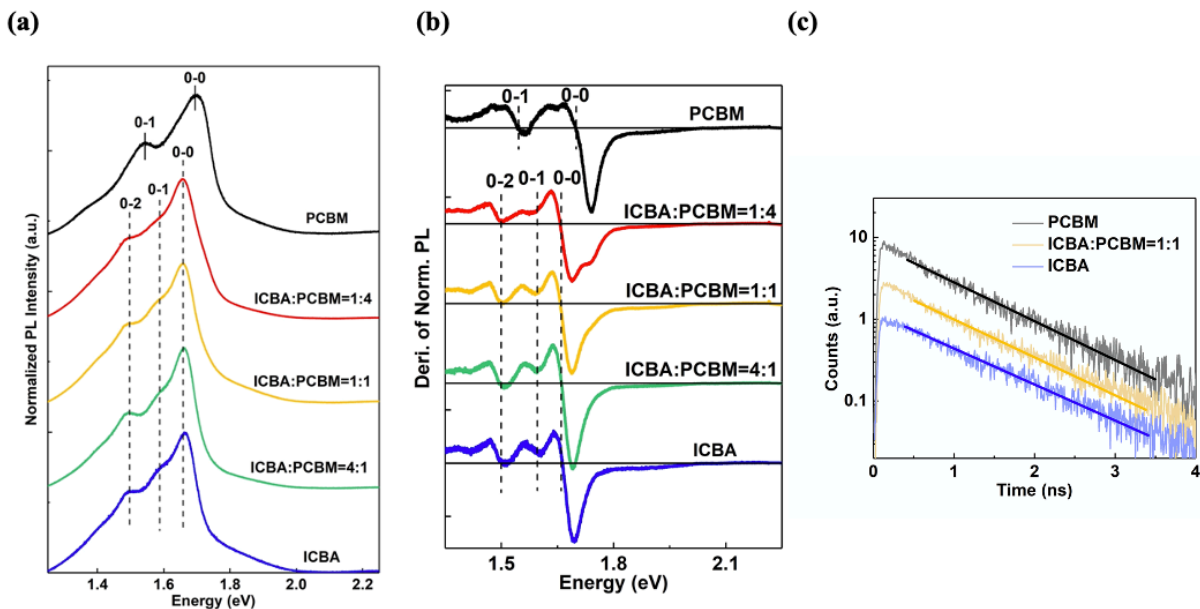


Figure 2.2 Photoluminescence (PL) measurements of ICBA:PC₆₁BM blends.

(a) Normalized steady-state PL spectra of ICBA, PC₆₁BM and their blends at indicated ratios. The short vertical lines indicate the exciton energies of PC₆₁BM, the long dashed lines indicate the exciton energies of the various vibronics of ICBA and the blends. (b) Derivative of the normalized steady-state PL spectra to more clearly indicate the alignment of the transition energies. (c) Time-resolved PL of ICBA, PC₆₁BM and their 1:1 blend. The solid lines are monoexponential fits used to extract the exciton lifetimes.

2.2.4 Charge Transfer States

The EL spectra of ternary OPVs with different blend ratios are shown Fig. 2.3(a). The CT state emission peak monotonically blue shifts from 1080 nm to 990 nm as the proportion of ICBA in the two acceptors increases from 0 to 100%. To understand this hypsochromic shift, we used a series of Gaussians to fit the EL spectra. As shown in Fig. 2.3(b), the EL spectrum of the DA₁ binary is fit using a P3HT exciton peak at 646 nm, ICBA exciton peaks at 725 nm and 823 nm, and the DA₁ binary CT state at 990 nm with a FWHM = 205 nm. Figure 2.3(c) is the EL spectrum of the DA₂ binary fit assuming a P3HT exciton peak at 645 nm, and of PC₆₁BM at 708 nm. Then the DA₂ binary CT state is at 1080 nm with FWHM = 215 nm. Figure 2.3(d) is an example of the Gaussian fit to the EL spectrum of the ternary DA₁A₂ with ratio 1:(0.5:0.5). It has the same exciton

peak positions of P3HT and PC₆₁BM. The CT emission peak comprising the two binaries is fit by their linear superposition with peaks at 990 nm and 1080 nm, and with FWHM = 205 nm and 215 nm, respectively. Thus, The CT state EL spectrum of a 1:(0.5:0.5) DA₁A₂ blend does not exhibit spectral features independent of those of the individual binaries.

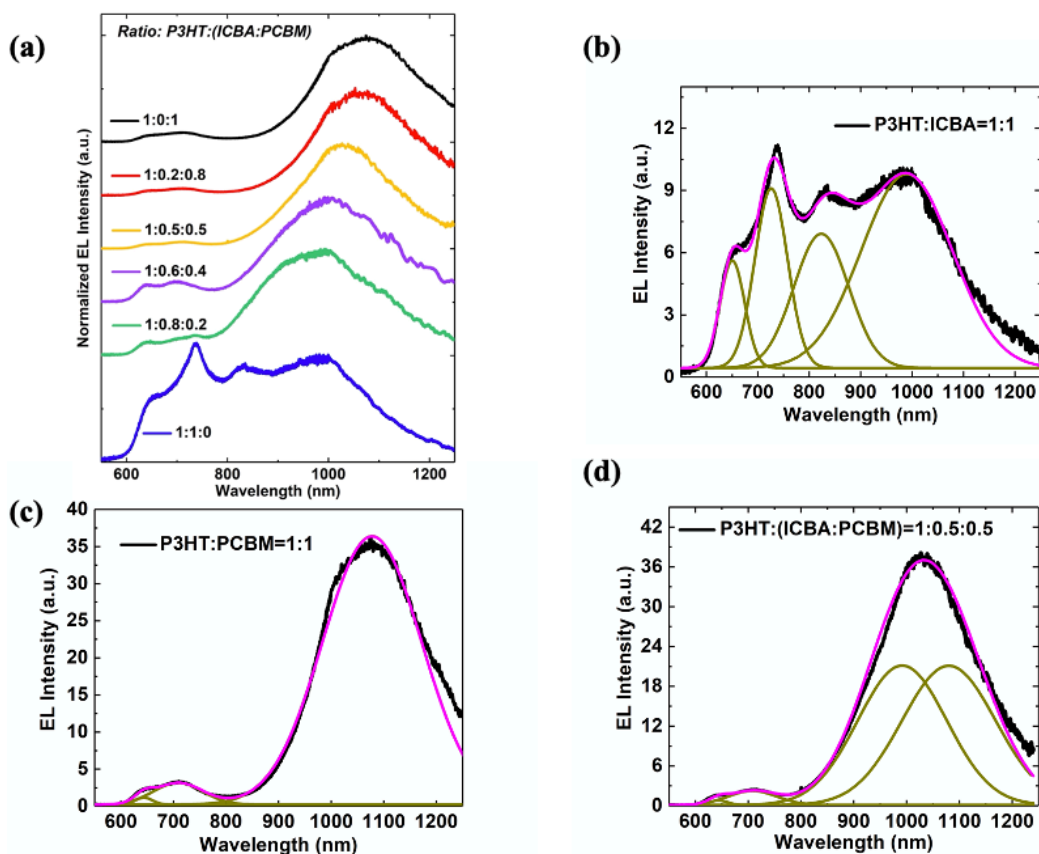


Figure 2.3 Electroluminescence (EL) of ternary OPV devices and corresponding Gaussian fits.

(a) EL spectra of binary and ternary OPVs with different P3HT:(ICBA:PC₆₁BM) blend ratios indicated. (b) The EL spectrum of 1:1 P3HT:ICBA. The Gaussian distributions used to fit the spectrum and the sum of these Gaussians are shown by the green and pink lines, respectively. (c) The EL spectrum of 1:1 P3HT:PC₆₁BM with the series of Gaussians (green lines) and their sum (pink). (d) The EL spectrum of 1:0.5:0.5 P3HT:(ICBA:PC₆₁BM) with fits as in (b) and (c).

A similar fitting procedure is applied to DA₁A₂ junctions of the same composition but with different acceptor blend ratios. The intensities of the DA₁ and DA₂ CT emission are found from the areas under the corresponding Gaussian distributions. In Fig. 2.4(a), the ordinate is the fraction of DA₂ CT state emission intensity, CT(DA₂), in the total ternary CT emission, CT(DA₁) + CT(DA₂).

The abscissa is the fraction of PC₆₁BM (A_2) in the acceptor mixture (A_1+A_2). We find a linear relationship between CT(DA₂) and A_2 blend fraction with unity slope and an intercept at the origin. Therefore, the CT emission of the ternary blends is a linear superposition of the binary spectra whose intensities are proportional to their concentration in the blends.

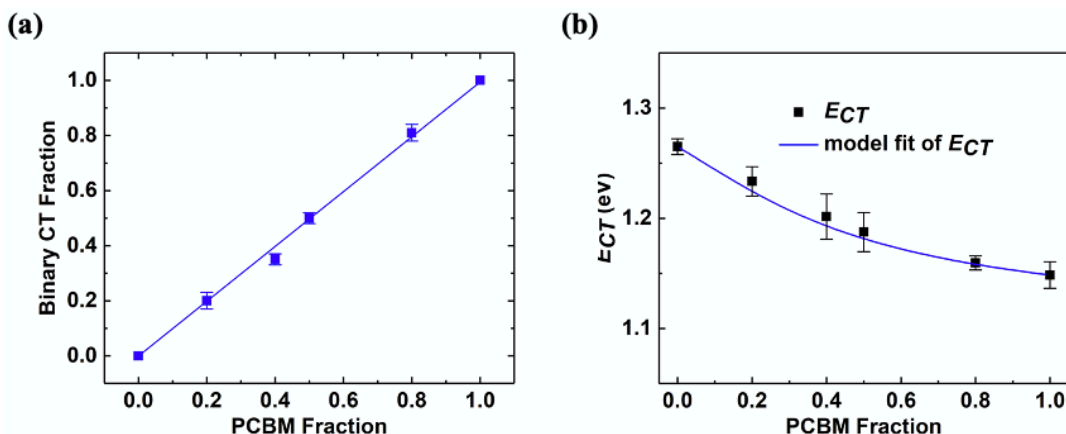


Figure 2.4 Relationship between ternary OPV charge transfer (CT) state and blend ratio.

(a) Relationship between the intensity fraction of the P3HT:PC₆₁BM CT state vs. the fraction of PC₆₁BM in the acceptors in the ternary blend. The line is a least square fit with unity slope and intercept at the origin. (b) Charge transfer state energy vs. PC₆₁BM fraction in the acceptors. The line shows the calculated relationship between the peak position of the sum of two binary Gaussians vs. blend ratio. The fit to the data show the measured peak positions are equal to the linear superposition of the Gaussian line shapes.

In the less clearly resolved absorption spectral analysis of Street, et al.,¹ it was found that the CT peak position of the blend follows Vegard's law via:

$$E_{CT} = (1 - x)E_{CT1} + xE_{CT2} - bx(1 - x), \quad (2.1)$$

where x is the fraction of PC₆₁BM to the total acceptor concentration, and $b = 0.15$ is the bowing parameter. Vegard's law is a simple, extrapolative expression with no analytical physical origin. Nevertheless, the existence of a bowing parameter suggests that the CT peak position may indeed be influenced by electronic orbital interactions in the mixture, although no comment was made to explain this in the previous work.¹ To explore this apparent nonlinearity, in Fig. 2.4(b) we simulate the sum of Gaussian distributions representing the two binary CT states. The blue solid line represents the simulated peak position found from the sum of two Gaussians centered at $E_{CT1} =$

1.15 eV and $E_{CT2} = 1.25$ eV, corresponding to the two binary CT state energies. The peak position is plotted as a function of the intensity fraction, which is the same as PC₆₁BM fraction as illustrated in Fig. 2.4(a). The simulation indicates that the linear superposition of these two Gaussian distributions results in an identical extrapolative dependence found by Vegard's Law, where the bowing arises from the simple addition of the two, Gaussian-shaped CT emission spectra.

2.2.5 Absence of Molecular Alloy in Ternary OPVs

Since the totality of the measurements show no evidence for the emergence of new electronic states, we conclude that the properties of the P3HT:ICBA:PC₆₁BM active region are explained by the linear superposition of the characteristics of the two constituent heterojunctions. Hence, we can eliminate, at least in this case, the existence of a molecular alloy.

One exogenous cause for the lack of evidence for alloying in P3HT:ICBA:PC₆₁BM blends based on our three criteria may be phase separation between the two acceptor components. That is, if separate domains of P3HT:ICBA and P3HT:PC₆₁BM are formed in the blend, the opportunity for electronic interactions between the two acceptors would not exist, thus explaining why no alloys are detected. However, similar chemical structures and thin film surface energies of ICBA (24.9 mN/m) and PC₆₁BM (27.6 mN/m) strongly predict the miscibility of these two molecules.²⁵ Furthermore, detailed nuclear magnetic resonance studies of acceptors blend and ternary blend show shifts of the ¹H and ¹³C resonance frequencies of the two acceptors compared to their individual spectra. This is attributed to homogeneous, random contacts between acceptors in the blends, indicating a lack of phase separation.²⁶ Hence, at least in this particular system, the lack of evidence for an alloy cannot be attributed to spatial separation of the two donor:acceptor constituents in the blend.

2.3 Evaluation of Other Possible Systems

The forgoing characterization illustrates a general procedure by which to identify the existence of an alloy. Based on the criteria stated in the introduction, the first step is to measure and compare the electronic states of the organic constituents and mixtures. If the electronic states of the mixtures are unchanged from those in the constituents, no alloy has been formed. If a difference is found, other reasons should be considered and if possible excluded, such as a linear superposition of electronic states of the constituents, aggregation of one molecular species when introducing another or other morphology changes,²⁷ and trap-state filling,²⁸ etc. The final identification of a molecular alloy can be made after this procedure is complete.

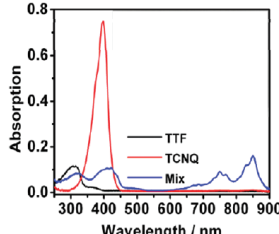
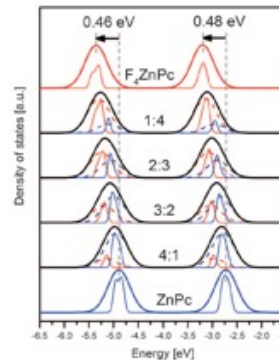
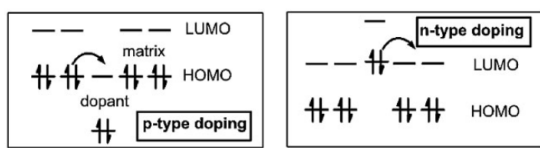
With these criteria in mind, we can attempt to evaluate other possible molecular alloy systems. Table 2.1 is a summary of some of the organic mixtures that have previously been described as organic alloys.

Organic CT salt complexes and their solid solutions are frequently mentioned as representing a class of organic alloys.⁴⁻⁸ The absorption and Raman spectra of organic CT salts are composed of the superposition of the spectra of the individual anionic and cationic states.^{5,6,8,29} This suggests that the result is a mixture of anions and cations that do not form alloys whose properties should differ from those of the reduced or oxidized constituents.

Another materials class with potential to form alloys are organic co-crystals, defined as a single phase material comprising two or more molecular organic species.^{22,23,30} Although some co-crystals appear to have tunable energy levels such as halogenated benzodifurandione-based oligo(p-phenylene vinylene) (BDOPV)-based small molecules,²² the origin of this energy level change is due only to electrostatic interactions between molecular dipoles or higher order

multipoles.^{31,32} Note that in this situation it is important to distinguish electrostatic interactions from intermolecular orbital interactions. For example, simulations based on electrostatic interactions and its consistency with experimental results³¹ can provide evidence as to whether electrostatic effects or alloying is responsible for the modification in electronic states.

Table 2.1 Summary of potential organic alloy systems.

Material system	Properties	Electronic states
Ternary OPV	V_{OC} depends on the blend ratio	In the P3HT:ICBA:PC ₆₁ BM ternary system, the excitonic and CT states are just the simple superposition of those of the two binaries.
Organic CT complexes	Metal-insulator transition temperature and conductivity depending on mixture ratio	 <p>UV-vis absorption of the TTF-TCNQ mix:²⁹ TTF radical cations (330, 430, and 650-700 nm); TCNQ radical anions (700-800 and 800-900 nm)</p>
Organic co-crystals	Tunable bandgap	 <p>DOS simulation of ZnPc:F₄ZnPc³¹ based on electrostatic interactions of molecular quadrupole fits to experimental results</p>
Organic eutectics	Solidification temperature depending on mixture ratio	No evidence presented to show modification of electronic states
Doped organic semiconductors	Conductivity and Seebeck coefficients depend on doping concentration	<p>Scheme of organic molecular doping process³⁷</p> 

Furthermore, organic eutectics are materials that have phase transition temperatures dependent on the relative proportion of their constituents.⁹⁻¹³ This distinct physical property is

similar to inorganic alloys and may, indeed, indicate formation of organic alloy. But the evidence thus far presented has not shown intermolecular electronic coupling. Hence, it is inconclusive that these mixtures are true alloys.

Doped organic semiconductors whose conductivities and Seebeck coefficients depend on doping concentration have also been studied as possible examples of alloys.³³⁻³⁷ Doping with donors or acceptors results in the charge transfer between electronic states from the dopant to the host.^{36,37} Even at the high molar densities typically used in highly doped organics (~0.1 molar ratio of dopant to host) new electronic states have not been reported. Other organic mixtures that do not belong to these categories have also been studied,^{14,38,39} including disordered organic solid solutions and binary helicies, yet once again no evidence has been presented to support the claim of a modification of the parent electronic states. To our understanding, therefore, there is yet no complete evidence to identify electronic coupling that would justify unambiguous identification of a molecular alloy in any of these previously reported systems.

2.4 Conclusion

In this chapter, we propose criteria that must be met to unambiguously identify a molecular organic alloy: that is, a mixture of two or more molecular organic substances that have intermolecular electron coupling that results in modification of the electronic states of the constituent molecules. Specifically, we investigated the P3HT:(ICBA:PC₆₁BM) ternary system which has previously been proposed to form molecular alloy between the two acceptors in the blend. The HOMO levels and the exciton energies of the acceptor blends are the same as for the individual components. Furthermore, the CT states in the ternary blends of varying acceptor ratios are a linear superposition of the two distinct binary CT states. According to our criteria, this ternary

system is simply a combination of two binary heterojunctions that do not form an organic molecular alloy. Using our procedure to identify a molecular organic alloy, we find no clear example has yet been found for the existence of such a material.

Chapter 2

Bibliography

1. Street, R. A., Davies, D., Khlyabich, P. P., Burkhart, B. & Thompson, B. C. Origin of the tunable open-circuit voltage in ternary blend bulk heterojunction organic solar cells. *J. Am. Chem. Soc.* **135**, 986–989 (2013).
2. Adachi, S. *Properties of semiconductor alloys : group-IV, III-V and II-VI semiconductors*. (Wiley, 2009).
3. Davis, J. R. (Joseph R. . *Alloying : understanding the basics*. (ASM International, 2001).
4. Engler, E. M., Scott, B. A., Etemad, S., Penney, T. & Patel, V. V. Organic Alloys: Synthesis and Properties of Solid Solutions of Tetraselenafulvalene-Tetracyano-p-quinodimethane (TSeF-TCNQ) and Tetrathiafulvalene-Tetracyano-p-quinodimethane (TTF-TCNQ). *J. Am. Chem. Soc.* **99**, 5909–5916 (1977).
5. Murata, T. *et al.* Tuning of multi-instabilities in organic alloy, [(EDO-TTF)_{1-x}(MeEDO-TTF)_x]2PF₆. *Chem. Mater.* **22**, 3121–3132 (2010).
6. Kubo, K. & Yamashita, M. New BEDT-TTF Radical Cation Salt with Mixed Anions: α' -[BEDT-TTF]₂[CuBr₂]_{0.4}[CuCl₂]_{0.6}. *Crystals* **2**, 284–293 (2012).
7. Ishikawa, T. *et al.* Optical Study of Electronic Structure and Photoinduced Dynamics in the Organic Alloy System [(EDO-TTF)_{0.89}(MeEDO-TTF)_{0.11}]2PF₆. *Appl. Sci.* **9**, 1174 (2019).
8. Murata, T. *et al.* Metal-insulator transition of alloyed radical cation salts, (Me_xEDO-TTF)₂PF₆. *Phys. B Condens. Matter* **405**, 45–48 (2010).
9. Pradesh, U. Physicochemical studies on organic eutectics and the 1 : 1 addition compound : **27**, 711–718 (1992).

10. Sturz, L., Witusiewicz, V. T., Hecht, U. & Rex, S. Organic alloy systems suitable for the investigation of regular binary and ternary eutectic growth. *J. Cryst. Growth* **270**, 273–282 (2004).
11. Rai, U. S. & Shekhar, H. Solidification behaviour of binary organic eutectic alloys. *Cryst. Res. Technol.* **29**, 533–542 (1994).
12. Witusiewicz, V. T., Sturz, L., Hecht, U. & Rex, S. Thermodynamic description and unidirectional solidification of eutectic organic alloys: I. Succinonitrile-(D)camphor system. *Acta Mater.* **52**, 4561–4571 (2004).
13. Rai, U. S. & Rai, R. N. Physical chemistry of organic eutectic and monotectic: hexamethylbenzene - Succinonitrile system. *Chem. Mater.* **11**, 3031–3036 (1999).
14. Bellows, J. C. & Prasad, P. N. Molecular motions and lattice stability of a disordered organic alloy: Binary solid solutions of 1,4-dihalonaphthalenes. *J. Chem. Phys.* **67**, 5802–5808 (1977).
15. Khlyabich, P. P., Rudenko, A. E., Thompson, B. C. & Loo, Y. L. Structural Origins for Tunable Open-Circuit Voltage in Ternary-Blend Organic Solar Cells. *Adv. Funct. Mater.* **25**, 5557–5563 (2015).
16. de Zerio, A. D. & Müller, C. Glass Forming Acceptor Alloys for Highly Efficient and Thermally Stable Ternary Organic Solar Cells. *Adv. Energy Mater.* **1702741**, 1–18 (2018).
17. Zhang, J. *et al.* Conjugated Polymer-Small Molecule Alloy Leads to High Efficient Ternary Organic Solar Cells. *J. Am. Chem. Soc.* **137**, 8176–8183 (2015).
18. Khlyabich, P. P., Sezen-Edmonds, M., Howard, J. B., Thompson, B. C. & Loo, Y. L. Formation of Organic Alloys in Ternary-Blend Solar Cells with Two Acceptors Having Energy-Level Offsets Exceeding 0.4 eV. *ACS Energy Lett.* **2**, 2149–2156 (2017).

19. Cheng, P. *et al.* Alloy Acceptor: Superior Alternative to PCBM toward Efficient and Stable Organic Solar Cells. *Adv. Mater.* **28**, 8021–8028 (2016).
20. Ameri, T., Khoram, P., Min, J. & Brabec, C. J. Organic ternary solar cells: A review. *Adv. Mater.* **25**, 4245–4266 (2013).
21. Lu, L., Kelly, M. A., You, W. & Yu, L. Status and prospects for ternary organic photovoltaics. *Nat. Photonics* **9**, 491–500 (2015).
22. Dou, J. *et al.* Organic Semiconducting Alloys with Tunable Energy Levels. *J. Am. Chem. Soc.* jacs.8b13471 (2019). doi:10.1021/jacs.8b13471
23. Dabros, M., Emery, P. R. & Thalladi, V. R. A supramolecular approach to organic alloys: Cocrystals and three- and four-component solid solutions of 1,4-diazabicyclo[2.2.2]octane and 4-X-phenols (X = Cl, CH₃, Br). *Angew. Chemie - Int. Ed.* **46**, 4132–4135 (2007).
24. Khlyabich, P. P., Burkhart, B. & Thompson, B. C. Efficient ternary blend bulk heterojunction solar cells with tunable open-circuit voltage. *J. Am. Chem. Soc.* **133**, 14534–14537 (2011).
25. Khlyabich, P. P., Rudenko, A. E., Street, R. A. & Thompson, B. C. Influence of polymer compatibility on the open-circuit voltage in ternary blend bulk heterojunction solar cells. *ACS Appl. Mater. Interfaces* **6**, 9913–9919 (2014).
26. Angmo, D., Bjerring, M., Nielsen, N. C., Thompson, B. C. & Krebs, F. C. Fullerene alloy formation and the benefits for efficient printing of ternary blend organic solar cells. *J. Mater. Chem. C* **3**, 5541–5548 (2015).
27. Mollinger, S. A., Vandewal, K. & Salleo, A. Microstructural and Electronic Origins of Open-Circuit Voltage Tuning in Organic Solar Cells Based on Ternary Blends. *Adv. Energy Mater.* **5**, 1–12 (2015).

28. Felekidis, N., Melianas, A. & Kemerink, M. Design Rule for Improved Open-Circuit Voltage in Binary and Ternary Organic Solar Cells. 37070–37077 (2017).
doi:10.1021/acsami.7b08276
29. Xiao, J. *et al.* Postchemistry of organic particles: When TTF microparticles meet tcnq microstructures in aqueous solution. *J. Am. Chem. Soc.* **132**, 6926–6928 (2010).
30. Sada, K. *et al.* Multicomponent organic alloys based on organic layered crystals. *Angew. Chemie - Int. Ed.* **44**, 7059–7062 (2005).
31. Schwarze, M. *et al.* Band structure engineering in organic semiconductors. *Science* **352**, 1446–9 (2016).
32. Salzman, I. *et al.* Tuning the ionization energy of organic semiconductor films: The role of intramolecular polar bonds. *J. Am. Chem. Soc.* **130**, 12870–12871 (2008).
33. Pfeiffer, M., Beyer, A., Fritz, T. & Leo, K. Controlled doping of phthalocyanine layers by cosublimation with acceptor molecules: A systematic Seebeck and conductivity study. *Appl. Phys. Lett.* **73**, 3202–3204 (1998).
34. Nollau, A., Pfeiffer, M., Fritz, T. & Leo, K. Controlled n-type doping of a molecular organic semiconductor: Naphthalenetetracarboxylic dianhydride (NTCDA) doped with bis(ethylenedithio)-tetrathiafulvalene (BEDT-TTF). *J. Appl. Phys.* **87**, 4340–4343 (2000).
35. Kim, G. H., Shao, L., Zhang, K. & Pipe, K. P. Engineered doping of organic semiconductors for enhanced thermoelectric efficiency. *Nat. Mater.* **12**, 719–723 (2013).
36. Lüssem, B., Riede, M. & Leo, K. *Doping of organic semiconductors. Physica Status Solidi (A) Applications and Materials Science* **210**, (2013).
37. Walzer, K., Männig, B., Pfeiffer, M. & Leo, K. Highly efficient organic devices based on electrically doped transport layers. *Chem. Rev.* **107**, 1233–1271 (2007).

38. Lei, Y. *et al.* Complex assembly from planar and twisted π -conjugated molecules towards alloy helices and core-shell structures. *Nat. Commun.* **9**, (2018).
39. Masumoto, Y. & Mori, T. Application of organic bathocuproine-based alloy film to organic light-emitting diodes. *Thin Solid Films* **516**, 3350–3356 (2008).

Chapter 3

End-capping Exchange Leads to Unstable Ternary Organic Photovoltaic Cells

For OPV devices to achieve consistent performance and long operational lifetimes, organic semiconductors must be processed with precise control over their purity, composition and structure. This is particularly important for high volume solar cell manufacturing where control of materials quality has a direct impact on yield and cost. Ternary blend OPVs containing two acceptor-donor-acceptor (A-D-A)-type NFAs and a donor have proven to be an effective strategy to improve solar spectral coverage and reduce energy losses beyond that of binary blend OPVs. In this chapter, we demonstrate that the purity of such a ternary is compromised during blending to form a homogeneously mixed bulk heterojunction thin film. We find that the impurities originate from end-capping exchange reactions of A-D-A-type NFAs, and that their presence influences both device reproducibility and long-term reliability. The end-capping exchange results in generation of up to four impurity constituents with strong dipolar character that interfere with the photoinduced charge transfer process, leading to reduced charge generation efficiency, morphological instabilities, and an increased vulnerability to photodegradation. As a consequence, the OPV efficiency falls to less than 65% of its initial value within 265 h when exposed to up to

10 suns intensity illumination. Our study reveals new insights to understand the reproducibility as well as reliability of ternary OPVs.

3.1 Introduction

An essential feature of all high-performance photovoltaic devices that exhibit an acceptable level of reproducibility and a long operational lifetime, is that the materials of which they are comprised are of high purity.¹ In crystalline Si photovoltaic cells, the chemical purity of Si has been an important limiting factor in their performance. The introduction of extrinsic impurities can result in significant changes in conductivity by creating lattice strain or by forming interstitial and substitutional defects. As a consequence, the precise control of source material purity is a common strategy for improving the efficiency and reliability of photovoltaics.

In contrast to inorganic photovoltaics, understanding the effects of impurities on OPVs has received little attention despite their potentially profound impact on performance. In fact, the molecular contaminants left over from synthesis, or that result from decomposition during device operation, can dramatically impact the intrinsic optical and electrical properties of pristine OPV materials.²⁻⁴ One example is the emergence of photoinduced dimerized products of the fullerene acceptor, C₆₀, during OPV operation, which reduces the exciton lifetime and diffusion length, leading to a significant decrease in device lifetime.⁵ Beyond these changes, impurities can disrupt the crystalline order in molecular solids,⁶ thereby reducing the charge carrier mobility and cell PCE. Therefore, considerable care must be taken to remove contaminants from the source materials and avoid material decomposition during device preparation and operation.

Ternary blend OPVs comprising one donor and two acceptors, or one acceptor and two donors have attracted great interest in recent years.⁷⁻¹¹ Compared with conventional binary

component devices, the introduction of a third molecular species into the BHJ layer can increase solar spectral coverage, reduce the energy loss, and significantly improve OPV efficiency. In particular, the rapid development of A-D-A type NFAs has led to ternary blend OPVs comprising two NFAs and a polymer donor with PCE approaching 20% under 1 sun intensity, AM1.5G illumination.^{12–15}

In this work, we find that device fabrication employing ternary blends can result in the generation of impurities that affect both the reproducibility of the performance and long-term reliability of the cells. In particular, we find that the vinyl groups linking the D and A moieties can dissociate at room temperature by the exchange of the end-capping groups between two NFAs^{16–22} during the mixing of the blend used in forming the BHJ thin film, the generality of the interaction is illustrated in Fig. 3.1.

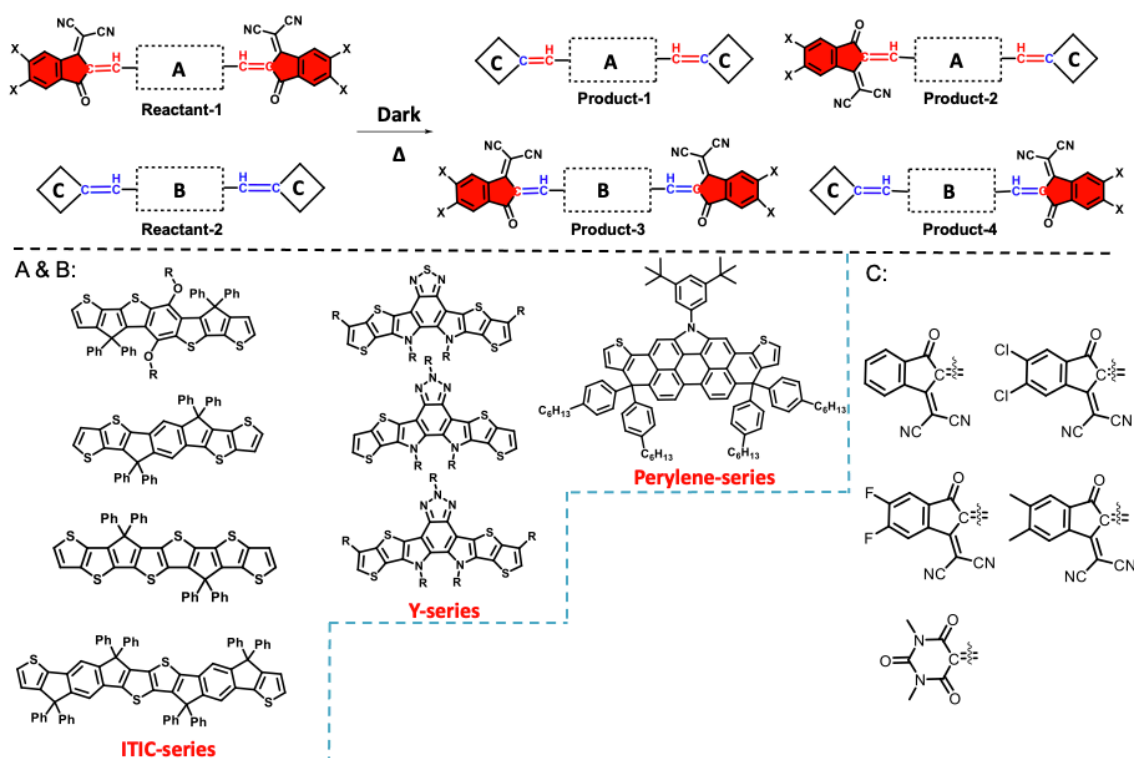


Figure 3.1 Generality of end-capping exchange reaction between A-D-A non-fullerene acceptors (NFAs). The top panel displays the end-capping exchange reaction between two A-D-A type NFAs. The vinyl groups linking the D and A moieties can dissociate at elevated temperature used during the mixing of the blend prior to forming the BHJ thin film. The exchange process results in both asymmetric and symmetric reaction products.

This exchange process results in reaction products with both asymmetric dipolar and symmetric non-polar molecular structures. As a consequence, ternary-blend OPVs based on one donor and two NFAs can unintentionally comprise up to seven chemical species. These impurities participate in photoinduced charge transfer, affecting cell performance and reproducibility of devices produced in different processing batches. Additionally, the asymmetric dipolar molecules introduce packing disorder and instabilities that make the blend vulnerable to photodegradation.

3.2 Characterization of End-capping Exchange Reaction

3.2.1 Experimental Methods

The pure materials solutions and hot ternary blend solution was prepared by the mixture of BT-IC:BTIC-4Cl(F) (1:1, w/w) in chlorobenzene (CB) at 65°C for 15 h with a concentration of 16 mg/ml. For reaction dynamics study, the mixture solutions were blended at temperatures ranging from 0°C to 100°C for 24 hours. Then the solvent was removed, and the crude mixture was dissolved in deuterated chloroform (CDCl₃) and analyzed by nuclear magnetic resonance (NMR). The NMR spectra of pure materials and blends were collected using a Varian MR400 spectrometer (400 MHz, ¹H; 101 MHz, ¹³C; 376 MHz, ¹⁹F) with trimethylsilane (TMS) as reference.

In addition, matrix-assisted laser desorption ionization with time-of-flight mass spectrometry (MALDI-TOF-MS) were collected using a Bruker AutoFlex Speed MALDI-TOF instrument. The instrument was calibrated with Peptide Calibration Standard II purchased from Bruker. The samples used for MS measurements were prepared with 1 mg/ml dichloromethane solvent. Matrix was used in the sample preparation. Acid matrix was prepared with *a*-cyano hydrocinnamic acid and basic matrix was prepared with 1,5-diamino naphthalene.

3.2.2 Interaction between Archetype NFAs: BT-IC and BT-CIC

We primarily base our studies of end-capping exchange on two archetype NFAs shown in Fig. 3.2(a), namely BT-IC and BT-CIC (BTIC-4Cl), which are among the best-performing materials systems for semitransparent organic solar cells.^{16,17,23–25} Both BT-IC and BTIC-4Cl have C₂ symmetry about their molecular backbones, and thus have small dipole moments (1.1 D). The OPV devices are typically prepared by spin coating mixtures of donor and acceptor materials to form the bulk heterojunction. CB is a common solvent for such solutions. Stirring a CB solution of BT-IC and BTIC-4Cl at 65°C in ultrapure N₂ gas (with O₂ < 0.1 ppm and H₂O < 0.1 ppm) for 15 h leads to the unintentional formation of a new compound.

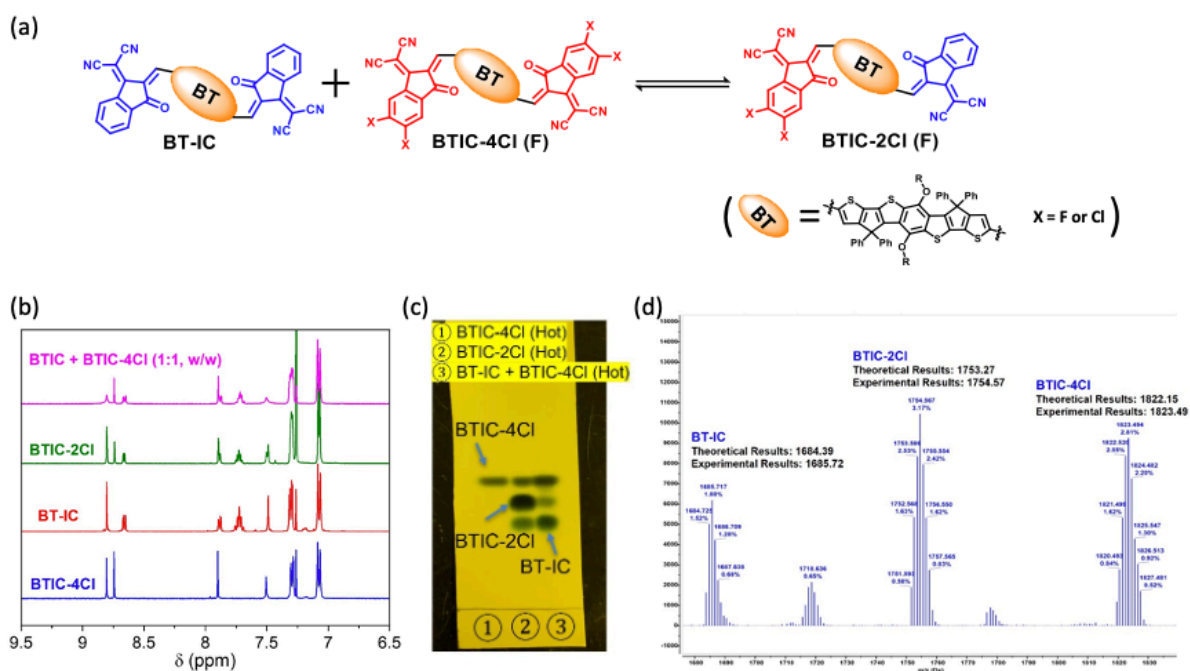


Figure 3.2 End-capping exchange reaction between archetype NFAs BT-IC and BTIC-4Cl.

(a) The exchange reaction between BT-IC and BTIC-4Cl(F) in chlorobenzene (CB) solution. (b) Comparison of the ¹H nuclear magnetic resonance (NMR) spectra of neat BT-IC, BTIC-4Cl, BTIC-2Cl vs. the physical blend solution of BT-IC:BTIC-4Cl (1:1, w/w). (c) Thin layer chromatography (TLC) of BTIC-4Cl, BTIC-2Cl and BT-IC:BTIC-4Cl mixture. (d) Matrix-assisted laser desorption ionization with time-of-flight mass spectrometry (MALDI-TOF-MS) analysis of BT-IC:BTIC-4Cl blend solutions.

To verify the chemical composition of the blend, the product was isolated via column chromatography and characterized by NMR spectroscopy, MALDI-TOF-MS, and thin layer

chromatography (TLC), with results shown in Figs. 3.2(b)-(d). The product of the reaction of BT-IC and BTIC-4Cl is BTCIC-IC (BTIC-2Cl), Fig. 3.2(a), the result of exchanging end groups between the two reactants. BTIC-2Cl has a significantly larger dipole moment (4.8 D) than the two precursor materials due to chlorination of only a single end group. We find that this reaction occurs in a mixture containing only BT-IC and BTIC-4Cl, as well as in solutions where a donor polymer has been added to the mixture, suggesting that the end-capping exchange reaction is an intrinsic property of A-D-A type NFAs. Furthermore, a solution of the asymmetric BTIC-2Cl was stirred at 65°C for 15 h, thereby producing BT-IC and BTIC-4Cl were produced (Fig. 3.2(c)), suggesting that the exchange reaction is reversible. Note that the reaction occurs even at room temperature after stirring in CB for over 3h in the dark.

3.2.3 Reaction Conditions

Since the ^1H NMR spectrum of BTIC-2Cl resembles a superposition of the BT-IC and BTIC-4Cl spectra, it is impossible to distinguish the product from the blend of the reactants. Therefore, we use fluorinated materials (BTIC-4F and BTIC-2F) to quantitatively characterize the reaction conditions via $^{19}\text{F}\{^1\text{H}\}$ NMR spectroscopy. As shown in Fig. 3.3(a), BTIC-2F is identified by two distinct doublet fluorine (F) peaks (panel 2) that are distinguished from those of BTIC-4F found down field (panel 1).

We investigated whether this reaction can occur in the solid film by preparing a BT-IC:BTIC-4F blend film obtained from a $T = 0^\circ\text{C}$ solution. Rather than the 65°C CB solution mixture that generates BTIC-2F with $r = 33\%$ (panel 3), no BTIC-2F is detected in the BT-IC:BTIC-4F blend film prepared at low temperature after aging 72 h at 100°C under nitrogen (see Fig. 3.3(a), panel 4), indicating that the exchange process is largely suppressed in the solid state.

Furthermore, the reaction kinetics of the end-capping exchange are also studied by $^{19}\text{F}\{^1\text{H}\}$ NMR spectroscopy. The BT-IC is blended with BTIC-4F in a CB solution for 24h at temperatures ranging from 0°C to 100°C . As shown in Fig. 3.3(b), the conversion ratio (r) increases monotonically with temperature, from $r = 0$ at $T = 0^\circ\text{C}$, to 17% at $T = 25^\circ\text{C}$, increasing to 88% at $T = 100^\circ\text{C}$. Thus, the end-capping exchange reaction is suppressed at low temperatures.

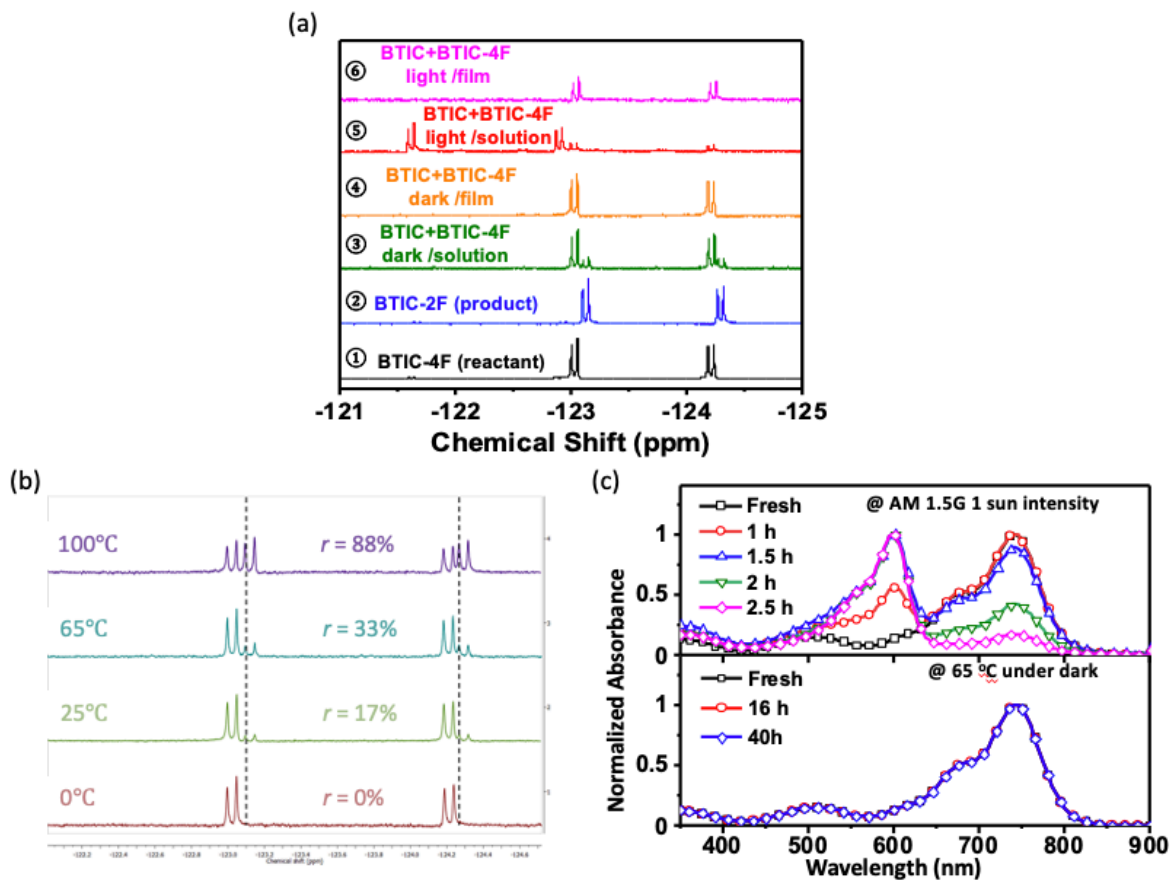


Figure 3.3 Reaction conditions of end-capping exchange.

(a) $^{19}\text{F}\{^1\text{H}\}$ NMR spectra of purified BTIC-4F (panel 1) and BTIC-2F (2), compared to those of BT-IC: BTIC-4F (1:1, w/w) blend solutions and films under different conditions: (3) BT-IC blended with BTIC-4F in the CB solution at $T = 65^\circ\text{C}$ in the dark, (4) the film obtained from the 0°C solution during blending, then aged at 72 h at 100°C under nitrogen; (5) BT-IC blended with BTIC-4F under one sun intensity, simulated AM1.5G illumination at $T = 0^\circ\text{C}$ for 2.5 h; (6) blend film obtained from the 0°C solution, then aged 48 h under sun intensity, simulated AM1.5 G illumination.

(b) Comparison of the $^{19}\text{F}\{^1\text{H}\}$ NMR spectra of the BT-IC:BTIC-4F (1:1, w/w) mixture after stirring in chlorobenzene for 24h at temperatures ranging from 0°C to 100°C .

(c) Absorption spectra vs. exposure time in the dark, at $T = 65^\circ\text{C}$ or one sun intensity, simulated AM1.5G illumination at 0°C .

The influence of illumination on the reaction is studied by exposing both the BT-IC:BTIC-

4F blend film and solution to one sun intensity, simulated AM1.5G illumination at 0°C for 48h and 2.5h, respectively. Surprisingly, in addition to the peaks of BTIC-2F, two new doublets emerge in the $^{19}\text{F}\{^1\text{H}\}$ NMR spectra from the exposed BT-IC:BTIC-4F solution (Fig. 3.3(a), panel 5), indicating that a chemical reaction process other than end-group exchange has occurred. It has been reported that this new reaction may be an intramolecular electrocyclic reaction between the end-group and the thienyl backbone²⁶. In contrast, no new chemical species are detected after illuminating the blend film (panel 6). This conclusion is further supported by the evolution of the absorption spectra of a BT-IC:BTIC-4F solution over time, as shown in Fig. 3.3(c). Light soaking for 2.5h significantly bleaches the BT-IC:BTIC-4F mixture whose absorption peak is centered at a wavelength of 750 nm. Again, the spectral shape and intensity of the mixture show no changes after 40h in the dark at 65°C, although its composition changes due to the end-capping exchange.

3.2.4 Generality of Reaction

A number of representative NFA molecules are selected to investigate the influence of molecular structure on the end-capping exchange reaction and the validity of the generality shown in Fig. 3.1. We find that the reaction can occur in the most efficient A-D-A NFA families reported thus far, independent of the composition of the central fused aromatic ring units, and that of the end-capping moieties. For example, a mixture of IT-IC¹⁸ and BTIC-4F generates the four expected constituents (ITIC-2F,²⁷ ITIC-4F,²⁸ BTIC-2F and BT-IC¹⁷) upon end-capping exchange after stirring at 65°C for 24h under ultrapure N₂, as shown in Fig. 3.4. Analogously, the same results are obtained for Y-series and perylene-series NFAs with detailed characterization data are provided in the Fig. 3.5.

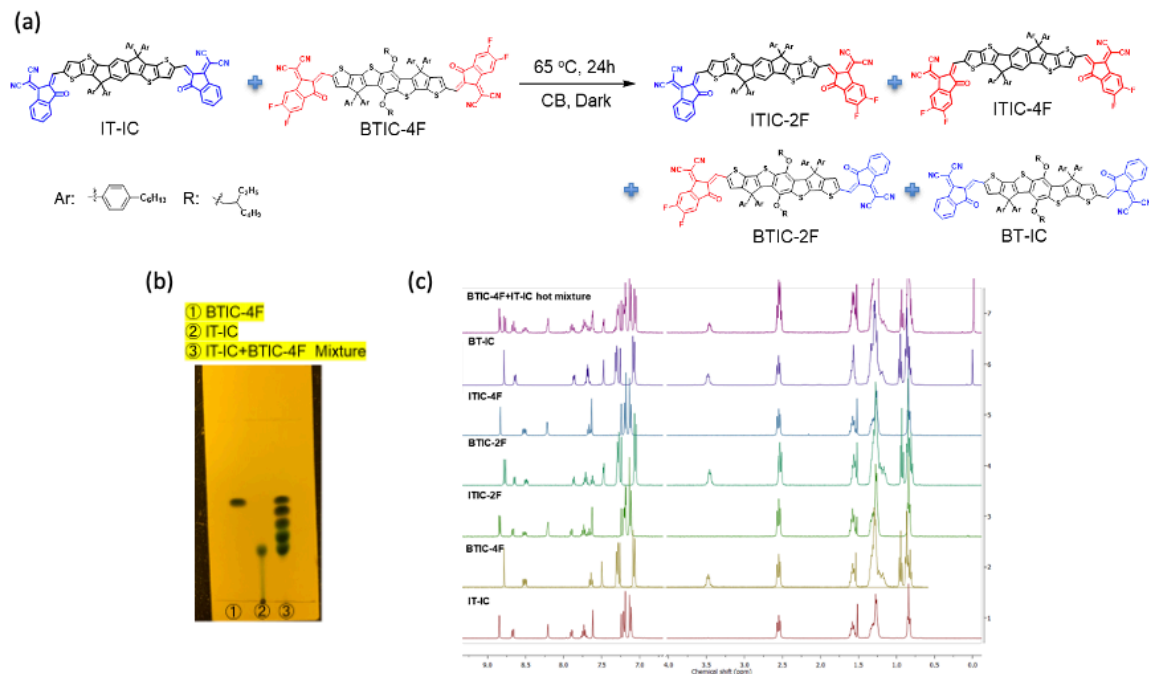


Figure 3.4 End-capping exchange between IT-IC and BTIC-4F with 4 reaction products.

(a) The exchange reaction between IT-IC and BTIC-4F. (b) TLC of BTIC-4F, IT-IC and IT-IC:BTIC-4F hot mixture. (c) ¹H NMR spectra of IT-IC, BTIC-4F, BTIC-2F, ITIC-2F, ITIC-4F, BT-IC and the IT-IC:BTIC-4F hot blend solution.

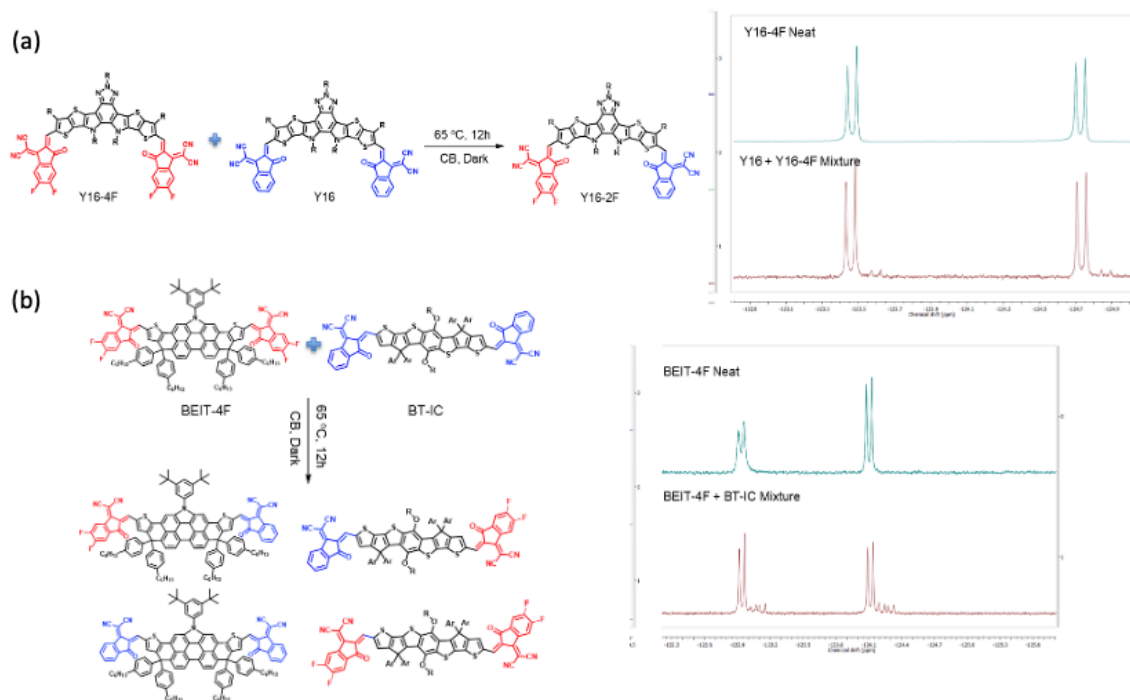


Figure 3.5 End-capping exchange reaction of Y-series and perylene-series NFAs.

(a) End-capping exchange between Y16 and Y16-4F. Comparison between the ¹⁹F NMR spectra of neat Y16-4F vs. Y16:Y16-4F hot mixture. (b) End-capping exchange between BEIT-4F and BT-IC and ¹⁹F NMR spectra of neat BEIT-4F vs. BT-IC:BEIT-4F hot mixture. The products can be identified by the distinct doublet fluorine (F) peaks.

3.3 Impact of End-capping Exchange on Ternary OPVs

3.3.1 Experimental Methods

Device fabrication

Ternary OPVs were fabricated with the device structure: indium tin oxide (ITO) / ZnO (30 nm) / PCE-10:BT-IC:BTIC-4Cl (1:0.75:0.75, w/w/w, 80 nm) / MoO_x (10 nm) / Ag (100 nm). For reliability test devices, C₇₀ and IC-SAM buffer layers are inserted between the BHJ and charge transporting layers to prevent chemical changes known to occur at the organic/inorganic interfaces over time.²³

Prior to device deposition, pre-patterned ITO-coated glass substrates were detergent- and solvent-cleaned, followed by CO₂ snow cleaning and exposure to ultraviolet-ozone for 15 min. The ZnO layer (ca. 30 nm) was spin cast from a ZnO precursor solution onto the substrates and then thermally annealed at 160°C for 30 min in air. The IC-SAM was dissolved in methanol with a concentration of 1 mg/ml and spin-coated at 4000 rpm for 60s, followed by thermal annealing at 110°C for 10 min. Then, the IC-SAM coated substrate was washed with methanol to remove the residues. The “hot” ternary blend active layer solution was prepared by the mixture of PCE-10:BT-IC:BTIC-4Cl (1:0.75:0.75, w/w/w) in CB at 65°C for 15h with a concentration of 20 mg/ml. The solution was cooled to room temperature and filtered once with a 0.45 μm polytetrafluoroethylene (PTFE) syringe filter prior to use, and then spin-coated onto the substrate at 2000 rpm for 90s to achieve a thickness of 80-90 nm. The “cold” ternary blend active layer solution was prepared by dissolving PCE-10 in a hot CB solution and then cooling to room temperature and mixing with BT-IC and BTIC-4Cl in a 1:0.75:0.75 ratio. Noted that the solution was stirring for about an hour and filtered with filter before fabricating the OPV device. The samples were transferred into the

vacuum chamber connected to glove boxes filled with ultrapure N₂ (O₂, H₂O < 0.1 ppm). The C₇₀, MoO₃ and Al films were deposited at 0.2 Å/s in a high vacuum chamber with a base pressure of 10⁻⁷ torr. The deposition rates and thicknesses were measured using quartz crystal monitors and calibrated post-growth by variable-angle spectroscopic ellipsometry. Device areas of 2 mm × 2 mm were defined by the overlap of the ITO anode and the Al cathode that is deposited through a shadow mask.

Device characterization

The *J-V* characteristics and EQE of the cells were measured in a glovebox filled with ultrapure N₂ (O₂ < 0.1 ppm, H₂O < 0.1 ppm). For the *J-V* measurements, light from a Xe lamp filtered to achieve a simulated AM1.5G spectrum (ASTM G173-03), whose 1 sun intensity was calibrated by a Si reference cell with traceable certification of National Renewable Energy Laboratory (NREL). The EQE measurements were performed with devices underfilled by a 200 Hz-chopped monochromated and focused beam from a Xe lamp. The current output from the devices as well as from a reference National Institute of Standards and Technology (NIST)-traceable Si detector were recorded using a lock-in amplifier. The *J_{SC}* were calculated from the EQE spectrum, with < 7% relative mismatch of the measured *J_{SC}* from *J-V* characteristics.

Device stability test

All devices were encapsulated by bonding a glass cover slide to the substrate in a glovebox filled with high purity nitrogen, using an ultraviolet-curable epoxy.

High-intensity illumination from LEDs operating at various intensities was concentrated onto the OPVs with Ag-coated reflective light pipes. The LED intensity that produced a photocurrent equivalent to *J_{SC}* under AM1.5G illumination (*J_{SC, AM1.5G}*) was equivalent to 1-sun intensity. To calibrate higher LED intensities, a neutral-density filter was used to ensure that the

OPVs remained in their linear regime. The neutral-density filter was 10% transmissive, thus the equivalent solar intensity (in units of suns) of the LEDs was calculated using the following equation:^{23,29}

$$\text{Equivalent solar intensity} = \frac{10 J_{\text{photon,LED}}}{J_{\text{SC,AM1.5G}}}. \quad (3.1)$$

All aging in the light soaking chamber were performed on the encapsulated devices in air under 10 ± 1.2 suns illumination intensity. To avoid excessive heating at high intensity, the OPV cells were actively water-cooled with a closed-loop chiller to $33 \pm 5^\circ\text{C}$.

Grazing incidence wide angle X-ray scattering (GIWAXS) measurements

The thin film samples were spin-coated onto Si wafers in a similar manner to the BHJ of devices. The thin films were measured at Beamline 11 of National Synchrotron Light Source II (NSLS-II), Brookhaven National Lab (BNL). The X-ray energy was 13.5 keV and the scattering patterns were recorded on a 2D image plate (Pilatus 800K) with a beam size of 200 μm . The samples were ~ 10 mm long in the direction of the beam path, and the detector was located at a distance of 259 mm from the sample center (distance calibrated by a AgB reference). The incidence angle was 0.1° and exposure time was 20s.

Resonant soft X-ray scattering (RSoXS) measurements

For the RSoXS samples preparation, PEDOT:PSS films were casted on top of Si substrates followed by organic films. The samples were emerged in DI water, dissolving away the PEDOT:PSS film. The floated organic films were then picked up by a 2 mm \times 2 mm SiN_x membrane window (Norcada NX5200C) and mounted onto an aluminum rack. The carbon-edge RSoXS profiles of the samples were measured at beamline 11.0.1.2 at the Advanced Light Source (ALS), Lawrence Berkeley National Lab (LBNL).

Electroluminescence (EL) measurements

The EL spectra were measured under 2V forward bias for fresh devices and under 10mA injection current for EL degradation study. The spectra were collected using a fiber-coupled monochromator (Princeton Instruments SP-2300i) equipped with a Si charge-coupled device (CCD) (PIXIS:400) for spectra between 700 nm and 950 nm and an InGaAs photodiode array (PyLoN-IR:1024) for spectra from 950 nm to 1400 nm.

3.3.2 Impact on Device Reproducibility

To systematically study the effects of impurities produced by the end-capping exchange reaction, devices with structure illustrated in Fig. 3.6(a) were fabricated with different reaction times, i.e., different time the blend solution is held at elevated temperature. The constituents in one group of OPVs (“hot”) were blended at $T = 65^{\circ}\text{C}$ for different reaction times, while a second, identical group of cells (“cold”) were prepared at $T = 25^{\circ}\text{C}$ for 0.5h to impede the reaction. Note that the hot solution is cooled to room temperature before fabricating the OPVs.

As expected, impurities in the BHJ increase with reaction time, where the presence of BTIC-2Cl is clearly detected in the active layer mixture after 24h, as shown in Fig. 3.6(b). The evolution of the solar cell performance parameters vs. blend solution reaction time for both cold and hot devices are plotted in Fig. 3.6(c). Here, the cold device corresponds to a reaction time of $t = 0\text{h}$. Contrary to expectations, the V_{OC} of hot ternary OPVs is pinned to the same value even though unintended reaction products are present in the BHJ layer. However, there is a decrease in PCE and FF for the hot ternary OPV devices. Compared to the cold device, the hot OPV shows a decreased FF (0.645 ± 0.004 vs. 0.673 ± 0.005) and PCE ($9.65 \pm 0.30\%$ vs. $10.21 \pm 0.30\%$) after blending for 24h.

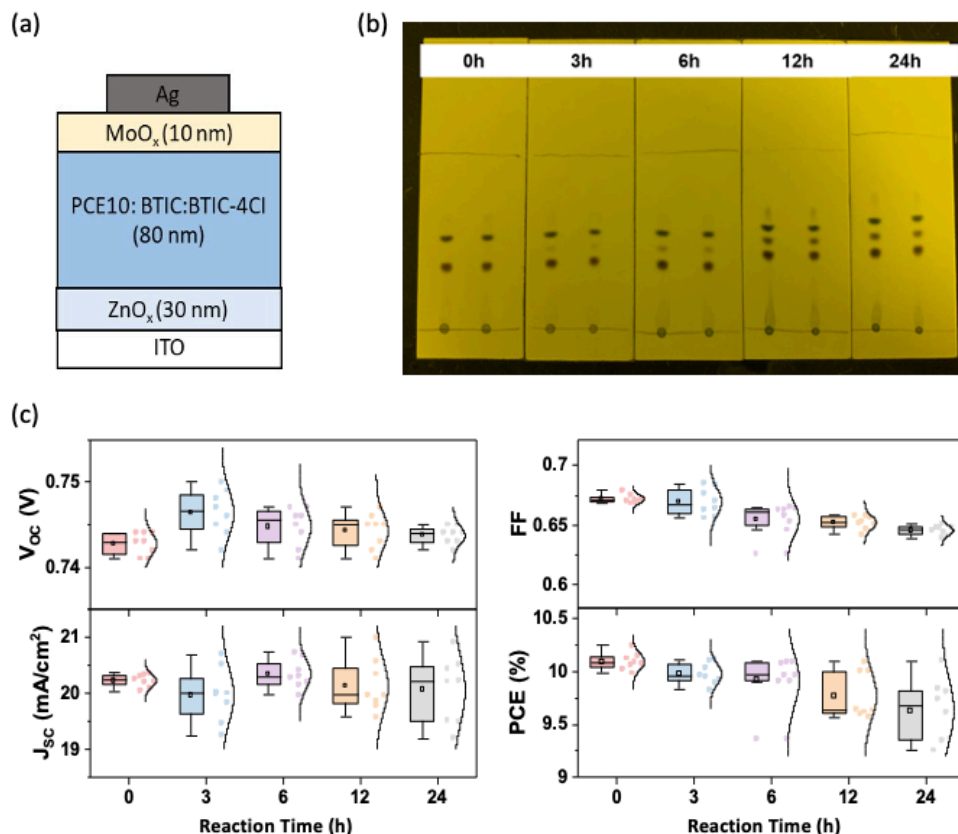


Figure 3.6 Impact of end-capping exchange reaction on archetype ternary OPV device reproducibility. (a) Schematic of device structure for reaction time study. (b) TLC of PCE-10:BT-IC:BTIC-4Cl active layer blend solution with different reaction times. (c) Power conversion efficiency, PCE, open-circuit voltage, V_{OC} , short-circuit current density, J_{SC} , and fill factor, FF , vs. reaction time.

Ternary blend OPVs based on PCE-10:IT-IC:BTIC-4F (1:1:1, w/w/w) and PCE-10:IT-IC:Y16-4F (1:1:1, w/w/w) were also evaluated versus reaction time to test the generality of the impact of impurities on their performance, with results shown in Fig 3.7. In contrast to the BT-IC:BTIC-4Cl mixture which produced only a single impurity molecule, both the IT-IC:BTIC-4F and IT-IC:Y16-4F mixtures generate multiple reaction products. As a consequence, a significant decrease in both PCE ($10.13 \pm 0.25 \%$ vs. $8.46 \pm 0.16 \%$ for PCE-10:IT-IC:BTIC-4F; and $10.32 \pm 0.41 \%$ vs. $9.38 \pm 0.59\%$ for PCE-10:IT-IC:Y16-4F) and FF (0.665 ± 0.006 vs. 0.544 ± 0.009 ; and 0.621 ± 0.004 vs. 0.605 ± 0.008) are observed, while the J_{SC} and V_{OC} remain unchanged.

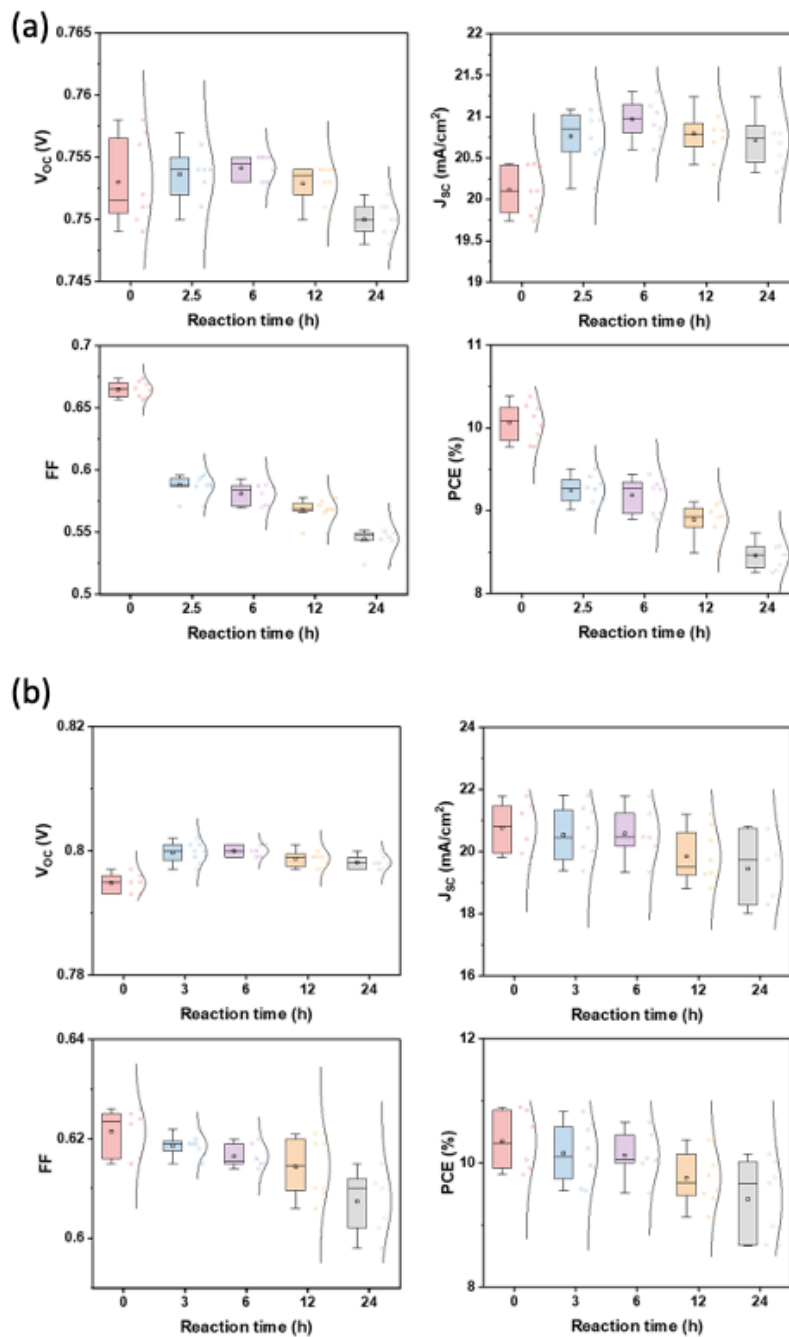


Figure 3.7 Generality of the impact of impurities on ternary device reproducibility.

The evolution of solar cell performance parameters over reaction time of (a) PCE-10:IT-IC:BTIC-4F (1:1:1, w/w/w) and (b) PCE-10:IT-IC:T16-4F (1:1:1, w/w/w) ternary blend BHJs.

Previous studies have attributed the changes in performance as well as in other electronic and physical properties in ternary OPVs that differ from its constituent binaries to the formation of “molecular alloys” or “organic co-crystals”. In contrast to earlier reports, here we have shown

that there is a thermally induced, solution-phase end-capping exchange reaction occurring between NFAs during materials preparation and device fabrication. This reaction contaminates the source materials, thereby altering the electronic and physical properties of the resulting films.

To understand the effects of impurities on hot ternary OPVs, we characterized the molecular packing and crystallization of the blend film GIWAXS. The two-dimensional (2D) diffraction patterns, and 1D line cuts of several films are provided in Fig. 3.8. The neat films of three individual acceptors show significantly different diffraction patterns due to the influence of the chlorination on molecular packing and crystallization. BT-IC (Fig. 3.8(a), panel 1) exhibits a rich diffraction pattern, indicating long range crystalline order. In contrast, the neat, dipolar BTIC-2Cl film (panel 2) shows considerably less well-defined diffraction features than BT-IC, with BTIC-4Cl (panel 3), exhibiting intermediate ordering. BTIC-2Cl and BTIC-4Cl both exhibit a pronounced and broad out-of-plane scattering feature at high q indicative of out-of-plane π - π stacking. On the other hand, the GIWAXS patterns of the hot and cold blend films of BT-IC:BTIC-4Cl (1:1, w/w) are remarkably different. In the absence of chemical reactions, the packing structure of the cold blend film (panel 4) is dominated by BT-IC, as evident by the similar (h00) in-plane diffraction peaks of BT-IC at 0.69, 0.97, 1.37 and 1.68 \AA^{-1} shown in Fig. 3.8(b). In contrast, the hot blend film (panel 5) shows several diffraction features found only in BTIC-2Cl (highlighted with white arrows) ascribed to the BTIC-2Cl generated in the reaction. This is further supported by the azimuthal distribution analysis of the diffraction feature at $q = 0.54 \text{\AA}^{-1}$ shown in Fig. 3.8(c), where the two intense peaks appearing at radial angles $\chi = \pm 26^\circ$ are only observed in the neat BTIC-2Cl and the hot blend films. Also, BTIC-2Cl appears to dominate the crystalline phase in the blends. The introduction of an equivalent amount of BTIC-2Cl into a cold mixture of BT-IC:BTIC-4Cl (1:1, w/w) (panel 6) shows the same pattern as neat BTIC-2Cl, indicating that this

asymmetric molecule is source of disorder, which is also confirmed by RSoXS measurement results shown in Fig. 3.8(d).

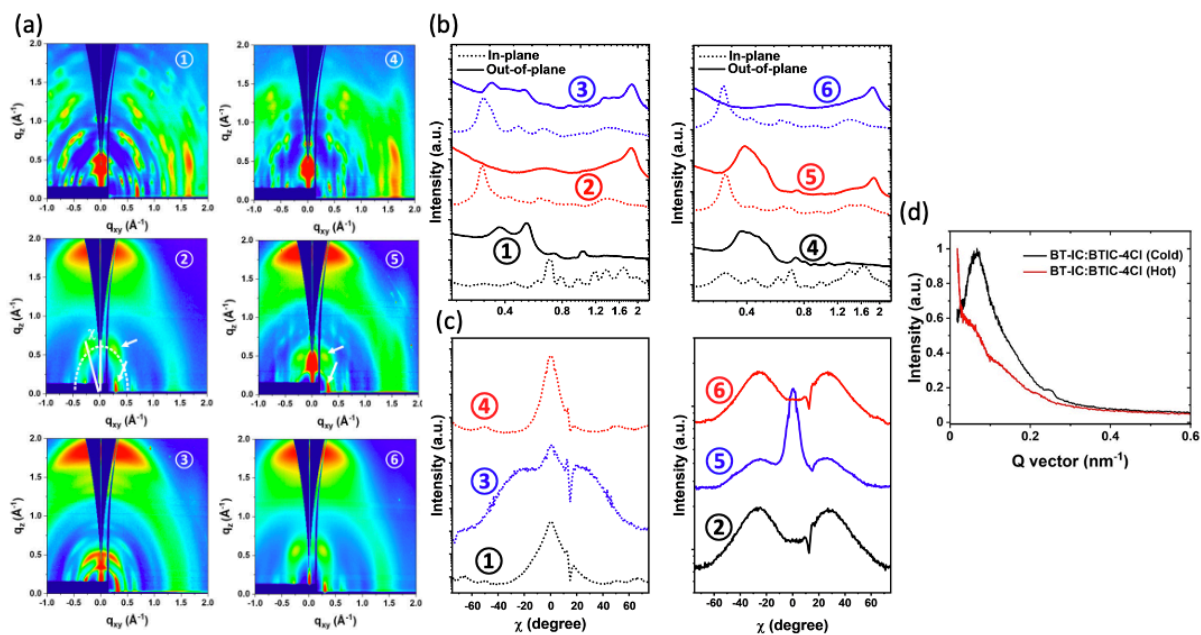


Figure 3.8 Morphologies of neat and blend films.

(a) Two-dimensional (2D) grazing incidence wide-angle X-ray scattering (GIWAXS) patterns of BT-IC (panel 1), BTIC-2Cl (2), and BTIC-4Cl (3) neat films prepared from cold solutions, BT-IC:BTIC-4Cl (1:1, by wt.) blend film prepared from cold solution (4) and from hot solution (5), and BT-IC:BTIC-2Cl:BTIC-4Cl (1:1:1, by wt.) blend film prepared from cold solution (6).

(b) In-plane (dotted line) and out-of-plane (solid line) X-ray scattering profiles extracted from 2D GIWAXS data.

(c) Azimuthal intensity distributions along $q = 0.54 \pm 0.05$ extracted from 2D GIWAXS data. (d) Resonant soft X-ray scattering (RSoXS) of BT-IC:BTIC-4Cl cold and hot blends.

Since the frontier molecular orbital of BTIC-2Cl differs from both BT-IC and BTIC-4Cl, its presence is expected to influence the CT processes of the blends, and thus the charge photogeneration properties of OPVs in which these compounds are employed. To investigate the CT state energetics, the EL spectra of PCE-10:BT-IC (1:1.5 by wt.), PCE-10:BTIC-2Cl (1:1.5 by wt.) and PCE-10:BTIC-4Cl (1:1.5 by wt.) were measured to find individual binary CT state emission, as shown in Figs. 3.9(a)-(c). The EL spectra due to CT \rightarrow S₀ transitions of cold and hot blends of PCE-10:BT-IC:BTIC-4Cl (1:0.75:0.75 by wt.)-based ternary OPVs are shown in Figs. 3.9(d) and (e), respectively. The ternary EL spectra are fit with linear combinations of the binary

CT spectra by maintaining their same peak positions and FWHM, while adjusting only their relative intensities, detailed fitting parameters are listed in Table 3.1. The EL spectrum of the cold ternary OPV is fit with two Gaussian peaks: one due to the PCE-10:BT-IC binary CT state at 1.36 ± 0.02 eV, and the other due to the PCE-10:BTIC-4Cl binary CT state at 1.15 ± 0.01 eV. On the other hand, three Gaussian peaks are required to fit the hot ternary OPV EL spectrum comprising both the PCE-10:BT-IC and PCE-10:BTIC-4Cl binary CT peaks, as well as an additional PCE-10:BTIC-2Cl binary CT peak at 1.23 ± 0.01 eV produced by the end capping reaction, suggesting the reaction product is active in photogeneration in the hot ternary OPV. The change in CT properties of hot ternary OPVs is attributed to the linear superposition of the constituent binary molecules, rather than the emergence of new electronic states due to the generation of deep levels or the formation of molecular alloys.³⁰

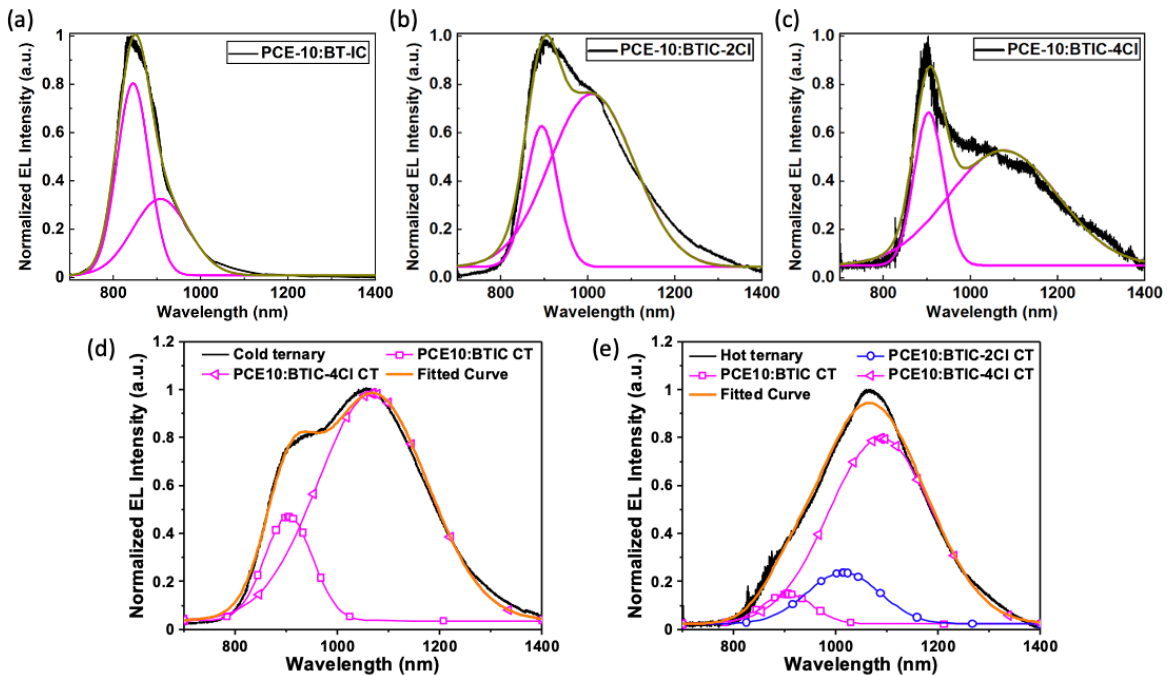


Figure 3.9 EL spectra of binary and ternary OPVs.

EL spectra of (a) PCE-10:BT-IC binary OPV with Gaussian fits using BT-IC exciton and binary CT peak, (b) PCE-10:BTIC-4Cl with Gaussian fits of BTIC-4Cl exciton and binary CT peak, (c) PCE-10:BTIC-2Cl with Gaussian fits of BTIC-2Cl exciton peak and binary CT peak, (e) cold PCE-10:BT-IC:BTIC-4Cl ternary OPV with Gaussian fits using two binary CT state emission peaks. (B) Hot ternary device with Gaussian fits to three binary CT state emission peaks.

Table 3.1 Charge transfer states emission peaks in binary and ternary OPVs.

Binary CT state	CT peak position (eV)	CT peak FWHM (eV)	Intensity fraction in cold ternary	Intensity fraction in hot ternary
PCE-10:BT-IC	1.36 ± 0.02	0.17 ± 0.01	16.7%	6.3%
PCE-10:BTIC-4Cl	1.15 ± 0.01	0.28 ± 0.02	83.3%	78.4%
PCE-10:BTIC-2Cl	1.22 ± 0.01	0.23 ± 0.01	-	15.4%

3.3.3 Impact on Device Reliability

The influence of impurities on the reliability of ternary blend OPVs was studied by exposing both the hot and cold devices with structure illustrated in Fig. 3.10(a) to white light illumination at an intensity as high as 10 suns (10 kW/m^2). Compared to the cold ternary device where PCE is reduced by 15% from its initial value after 265h, that of the hot ternary device falls to less than 65% over the same period due to a rapid decrease in J_{sc} and FF , as shown in Fig. 3.10(b). This is consistent with previous results where the presence of impurities in OPVs were implicated in exciton quenching, leading to correspondingly shorter device operational lifetimes.^{2,3}

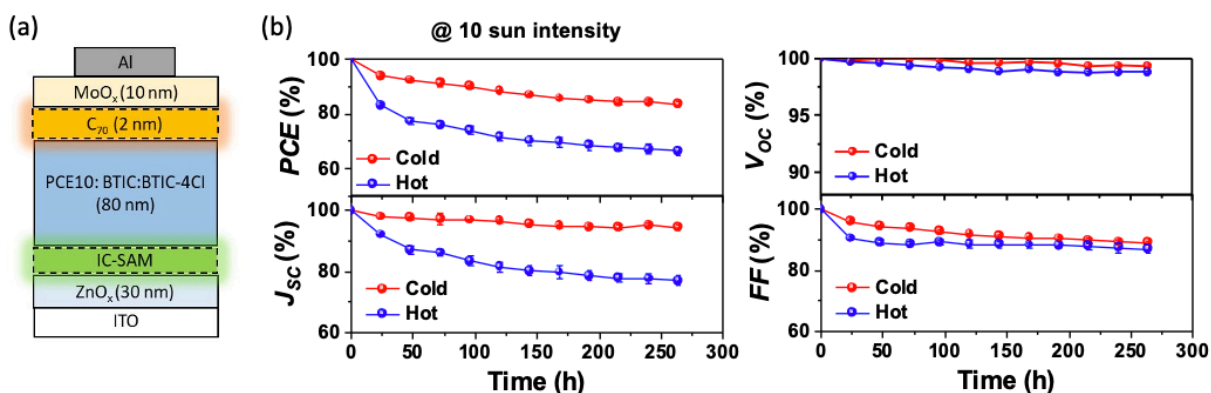


Figure 3.10 Impact of end-capping exchange reaction on archetype ternary OPV device reliability.

(a) Schematic of device structure for reliability study. (b) Normalized PCE, J_{sc} , V_{oc} , and FF vs. aging time under white-light illumination at 10 suns intensity.

To investigate the impact of impurities on reliability, the morphological stability of cold and hot ternary blend films of PCE-10:BT-IC:BTIC-4Cl (1:0.75:0.75, w/w/w) after aging for 48h under 10 sun intensity was studied via GIWAXs. As shown in Fig. 3.11, white light illumination shows no significant changes in their GIWAXS patterns of the cold film. In contrast, significant degradation is observed for the hot film due to the emergence of dipolar reaction products, resulting in the disappearance of the (010) peak at 1.8 \AA^{-1} .

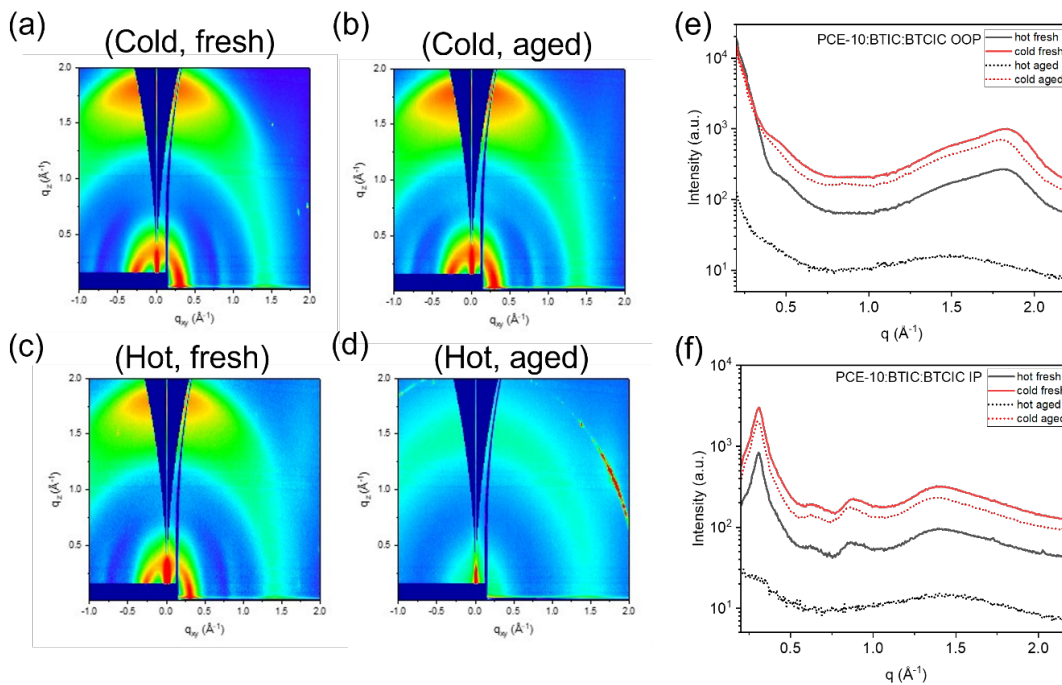


Figure 3.11 Morphological changes of cold and hot ternary blend films over aging.

The 2D GIWAXS patterns of PCE-10:BT-IC:BTIC-4Cl (a) cold, fresh, (b) cold, aged (c) hot, fresh and (d) hot, aged blend films. (e) In-plane and (f) out-of-plane sector-averaged profiles extracted from 2D GIWAXS data.

The asymmetric dipolar products of the end-capping exchange reaction have large polarizabilities; i.e. $\alpha = 1.25 \times 10^{-21} \text{ cm}^3$ for BTIC-2Cl, $\alpha = 4.56 \times 10^{-22} \text{ cm}^3$ for BT-IC, and $\alpha = 2.90 \times 10^{-22} \text{ cm}^3$ for BTIC-4Cl. This may result in dipoles reorientation over time that decreases the electric field across the BHJ, and hence reduces the charge extraction efficiency. The voltage-dependent photocurrent before and after 265h aging under illumination intensity of 10

suns, normalized to the photocurrent at $V = 0$, are shown in Fig. 3.13(a). A significant increase in the voltage-dependence of charge extraction is observed in the hot devices after aging. Additionally, the charge-extraction efficiency at $V = 0$ was calculated over the aging period and plotted in Fig. 3.13(b). The hot ternary device experienced a $16.3 \pm 1.8\%$ decrease in charge-extraction efficiency, whereas only a $2.0 \pm 1.2\%$ decrease is observed in the cold ternary device. Therefore, the J_{SC} and FF of hot ternary device decreased after aging owing to the loss in charge-extraction efficiency.^{32,33} A more complete analysis of the effect of reorientation on charge extraction efficiency will be discussed in Chapter 4.

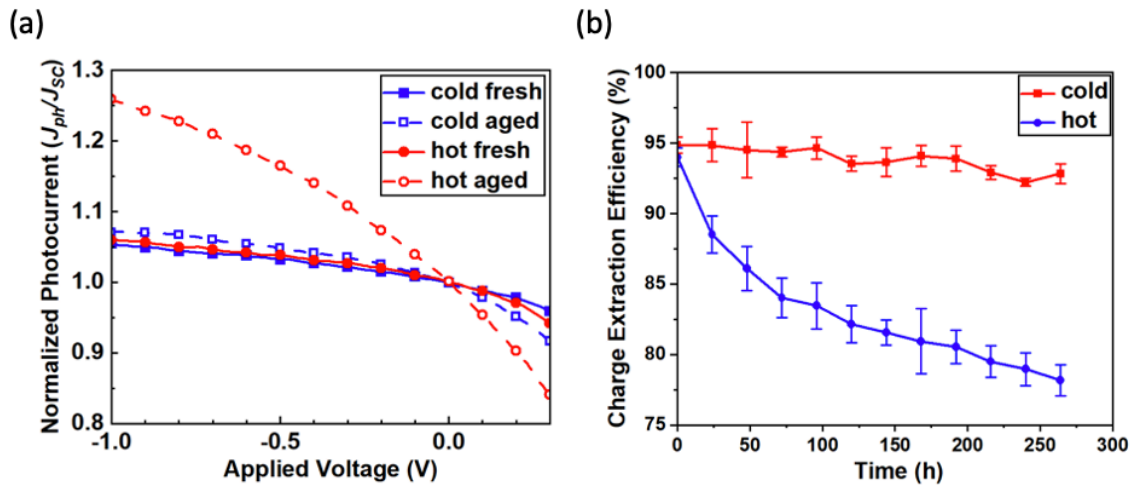


Figure 3.12 Change in charge extraction of cold and hot ternary OPVs over aging.

(a) Normalized voltage-dependent photocurrent of cold and hot ternary devices before and after aging for 265 h under white-light illumination at 10 suns intensity. (b) Charge-extraction efficiency at $V = 0$ (extracted from the reverse-bias photocurrent data) plotted against aging time.

3.4 Degradation of CT State Electroluminescence and V_{OC}

3.4.1 Relationship between CT State EL and V_{OC} Degradation

Three mechanisms that determine the magnitude of V_{oc} are: (i) radiative recombination of optically generated excited states, or excitons, within the donor or acceptor regions; (ii) radiative recombination due to CT state relaxation; and (iii) non-radiative recombination due to defect states or other diode non-idealities. This latter process may result in a voltage loss over time. To quantify

these effects, the non-radiative voltage loss, ΔV_{nr} , is defined as the difference between the open-circuit voltage in the presence of only radiative processes (the radiative limit), V_{oc}^{rad} , and the actual V_{oc} of the cell, viz.³³:

$$\Delta V_{nr} = V_{oc}^{rad} - V_{oc} = \frac{kT}{q} \ln \left(\frac{J_{sc}}{J_0^{rad}} \right) - V_{oc}, \quad (3.2)$$

where J_{sc} is the short circuit current density, J_0^{rad} is the dark saturation current density in the radiative limit (i.e. in the absence of non-radiative effects), k is the Boltzmann constant, T is the temperature, and q is the elementary charge. Previously, detailed balance has been invoked to relate ΔV_{nr} to the forward-biased external emission efficiency. Other works have, incorrectly, assumed that the external emission efficiency is equal to the EL external quantum efficiency, η_{EL} , and asserted that in the radiative limit $\eta_{EL} = 1$.^{34–38} For an organic device where emission is dominated by the CT state, however, the current resulting from non-radiative recombination will be exactly zero when the emissive CT state efficiency, η_{CT} , is unity, which is not equivalent to $\eta_{EL} = 1$. Rather, the measured EL efficiency is dependent on several factors given by:

$$\eta_{EL} = \gamma \chi_{em} \eta_{CT}, \quad (3.3)$$

where γ is the charge balance factor (i.e. the ratio of photons emitted to electrons that radiatively recombine with holes at the HJ).^{1,39} The ratio of emissive CT states formed by electrical injection, χ_{em} , depends on whether the states reside in the singlet or triplet manifold. That is, if the emissive CT states are singlets, $\chi_{em} = 0.25$, whereas if they are triplets or a mixed state, the ratio may assume a value as high as 1, depending on whether the triplets are emissive phosphorescent states, respectively. Thus, η_{EL} must account for χ_{em} , and γ when determining the magnitude of η_{CT} .

Under open-circuit conditions, the ideal diode equation for an OPV is written as:⁴⁰

$$J_0 \left(\exp \left(\frac{qV_{oc}}{nkT} \right) - \frac{k_{PPd}}{k_{PPd,eq}} \right) = -J_{ph}, \quad (3.4)$$

where J_0 is the dark saturation current, n is the ideality factor (which is well-defined only for purely diffusion, $n = 1$, and mid-gap recombination, $n = 2$, currents), k_{PPd} is the polaron pair dissociation rate at V_{oc} , $k_{PPd,eq}$ is the polaron pair dissociation rate in thermal equilibrium, and J_{ph} is the photocurrent. An OPV in thermal equilibrium requires that the photocurrent due to thermal excitation is balanced by current injection leading to recombination at the CT state. Thus, in the dark:

$$J_{out}(V_{oc}) = J_0^{rad} \left(\exp\left(\frac{qV_{oc}}{nkT}\right) - 1 \right) \approx J_0^{rad} \left(\exp\left(\frac{qV_{oc}}{nkT}\right) \right), \quad (3.5)$$

where J_0^{rad} is the saturation current due to excitation due to a room temperature blackbody, and J_{out} is the radiative recombination current density generated from the CT state. For simplicity, we assume $k_{PPd} \approx k_{PPd,eq}$ in Eq. 3.5. Returning to η_{EL} , which is defined as the number of photons emitted per electrons injected, we can write:

$$\eta_{EL} = \frac{J_{out}(V_{oc})}{J_{inj}(V_{oc})} \gamma \chi_{em}, \quad (3.6)$$

where J_{inj} is the injected current density resulting from the applied forward voltage. Equation 3.3 provides a physical understanding for the origin of OLED efficiency, while Eq. 3.6 is defined in terms of measurable quantities from the OPV cell operated as an OLED. The open circuit condition requires that the total current is zero. Therefore, $J_{inj}(V_{oc})$ must be balanced by an equal and opposite photocurrent, i.e. $J_{inj}(V_{oc}) = J_{ph}(V_{oc})$; an equality that allows us to relate η_{EL} to V_{oc} . For OPVs, it cannot be assumed that $J_{ph}(V_{oc}) = J_{sc}$, because J_{ph} is dependent on voltage. This is due to the fact that in an ideal junction, k_{PPd} is dependent on electric field at the heterojunction. Thus,

$$J_{inj}(V_{oc}) = J_{ph}(V_{oc}) = J_{sc} - J_{\Delta}, \quad (3.7)$$

where J_{Δ} accounts for the difference between $J_{ph}(V_{oc})$ and J_{sc} .

Combining Eq. 3.4, Eq. 3.5, and Eq. 3.6, and solving for V_{oc} gives the following expressions:

$$V_{oc} = \frac{kT}{q} \ln \frac{J_{sc} - J_{\Delta}}{J_0^{rad}} + \frac{mkT}{q} \ln \left(\frac{\eta_{EL}}{\gamma \chi_{em}} \right), \quad (3.8)$$

$$V_{oc} = V_{oc}^{rad} + \frac{kT}{q} \ln \frac{J_{ph}(V_{oc})}{J_{sc}} + \frac{mkT}{q} \ln \eta_{CT}. \quad (3.9)$$

Because η_{CT} already accounts for non-idealities resulting within the heterojunction, we have introduced the factor, m , in Eq. 3.8 to account for nonradiative losses occurring *outside* the HJ. The first term of Eq. 3.9 does not include the m -factor because nonradiative losses occurring both within and external to the HJ are not present in the radiative limit. The lower bound for this factor is, therefore, $m = 1$, which is defined by the ideal diode equation in the absence of traps.⁴⁰ In this limit, all recombination is radiative, leading to $\eta_{CT} = 1$ and $m = 1$. The second term of Eq. 3.9 accounts for the voltage dependence of J_{ph} , and the third term is equivalent to ΔV_{nr} , which accounts for all nonradiative losses. Losses that are not already contained within η_{CT} are quantified by the empirical value of $m > 1$.

Equation 3.8 and 3.9 can be used to locate the sources that lead to OPV efficiency losses of over time. The ratio, χ_{em} , is independent of changes in the device properties and, therefore, is time independent. Hence, the change in V_{oc} is given by:

$$\begin{aligned} \Delta V_{oc} &= V_{oc}(t) - V_{oc}(0) \\ &= [V_{oc}^{rad}(t) - V_{oc}^{rad}(0)] + \frac{kT}{q} \left[\ln \frac{J_{ph}(V_{oc},t) J_{sc}(0)}{J_{ph}(V_{oc},0) J_{sc}(t)} \right] + \frac{mkT}{q} \left[\ln \frac{\eta_{EL}(t)\gamma(0)}{\eta_{EL}(0)\gamma(t)} \right], \end{aligned} \quad (3.10)$$

where m can be found by fitting Eq. 3.10 to the observed value of ΔV_{oc} .

3.4.2 CT State EL and V_{oc} Degradation of Ternary OPVs

To track the non-radiative recombination in the ternary OPVs over aging, the EL spectra are periodically collected for both cold and hot devices aged under white light illumination at 10 suns intensity. As shown in Figs. 3.13(a) and (b), the EL intensity of the hot ternary OPV degrades

by 25%, which is faster compared to cold device (16%). Additionally, the peak intensity decays rapidly within the first 96 h, qualitatively matching the initial losses observed in V_{OC} and FF .

As shown in Fig. 3.13(c), by fitting (dashed lines) Eq. 3.10 to the changes in η_{EL} and ΔV_{OC} over time (data points),⁴¹ we obtain $m = 1.00 \pm 0.05$ for both cold and hot devices. This suggests that the increased nonradiative recombination loss in hot ternary devices occurs solely in the BHJ. This loss, originating from the reaction products generated in hot ternary BHJ, leads to fast V_{OC} degradation.

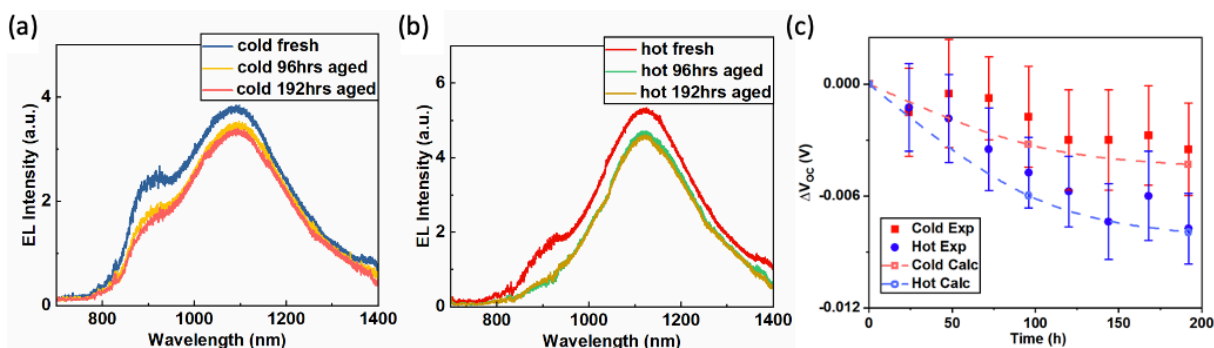


Figure 3.13 Non-radiative recombination loss during cold and hot ternary devices aging.

EL spectra of (a) cold and (b) hot ternary devices based on PCE-10: BT-IC: BTIC-4Cl (1:0.75:0.75, by wt.) before and after aged for 192h under illumination at 10 suns intensity. (c) Measured changes in open-circuit voltage (ΔV_{oc}) over time for cold and hot ternary devices (data points) along with ΔV_{oc} calculated from the loss in EL intensity.

3.5 Conclusion

In summary, we find that ternary blend OPVs consisting of two A-D-A type NFAs and a donor are susceptible to end-capping exchange reactions between NFAs during material blending prior to film deposition, even at room temperature in the dark. The reactions are considerably accelerated at elevated temperatures customarily used in material preparation. Additionally, the reaction products feature significant ground state dipole moments that are linked to a decrease in the crystallization of the BHJ nanostructure, and that increase non-radiative charge recombination when employed in OPVs, thereby reducing both the device reproducibility and long-term stability.

Our results provide new insights for understanding and improving the performance of a large and general class of materials when used in ternary blend OPVs.

Chapter 3

Bibliography

1. Forrest, S. R. *Organic Electronics: Foundations to Applications*. (Oxford University Press, 2020).
2. Mateker, W. R. *et al.* Improving the long-term stability of PBDTTPD polymer solar cells through material purification aimed at removing organic impurities. *Energy Environ. Sci.* **6**, 2529–2537 (2013).
3. Salzman, R. F. *et al.* The effects of copper phthalocyanine purity on organic solar cell performance. *Org. Electron.* **6**, 242–246 (2005).
4. Tetreault, A. R., Holst, D. P., Josey, D. S. & Bender, T. P. Impure sexithiophene: The reality of supplied materials for organic electronic applications. *Org. Electron.* **92**, 106091 (2021).
5. Wang, N., Tong, X., Burlingame, Q., Yu, J. & Forrest, S. R. Photodegradation of small-molecule organic photovoltaics. *Sol. Energy Mater. Sol. Cells* **125**, 170–175 (2014).
6. Forrest, S. R., Kaplan, M. L. & Schmidt, P. H. Organic-on-inorganic semiconductor contact barrier diodes. II. Dependence on organic film and metal contact properties. *J. Appl. Phys.* **56**, 543–551 (1984).
7. Lu, L., Xu, T., Chen, W., Landry, E. S. & Yu, L. Ternary blend polymer solar cells with enhanced power conversion efficiency. *Nat. Photonics* **8**, 716–722 (2014).
8. Gasparini, N., Salleo, A., McCulloch, I. & Baran, D. The role of the third component in ternary organic solar cells. *Nat. Rev. Mater.* **4**, 229–242 (2019).
9. Yu, R. *et al.* Recent Progress in Ternary Organic Solar Cells Based on Nonfullerene Acceptors. *Adv. Energy Mater.* **8**, 1702814 (2018).

10. Li, Y. *et al.* Vacuum-Deposited Biternary Organic Photovoltaics. *J. Am. Chem. Soc.* **141**, 18204–18210 (2019).
11. Li, Y. *et al.* Near-Infrared Ternary Tandem Solar Cells. *Adv. Mater.* **30**, 1804416 (2018).
12. Cui, Y. *et al.* Single-Junction Organic Photovoltaic Cell with 19% Efficiency. *Adv. Mater.* **33**, 2102420 (2021).
13. Zuo, L. *et al.* Dilution effect for highly efficient multiple-component organic solar cells. *Nat. Nanotechnol.* **17**, 53–60 (2022).
14. Zhan, L. *et al.* Manipulating Charge Transfer and Transport via Intermediary Electron Acceptor Channels Enables 19.3% Efficiency Organic Photovoltaics. *Adv. Energy Mater.* **12**, 2201076 (2022).
15. Hultmark, S. *et al.* Suppressing Co-Crystallization of Halogenated Non-Fullerene Acceptors for Thermally Stable Ternary Solar Cells. *Adv. Funct. Mater.* **30**, 2005462 (2020).
16. Li, Y. *et al.* High Efficiency Near-Infrared and Semitransparent Non-Fullerene Acceptor Organic Photovoltaic Cells. *J. Am. Chem. Soc.* **139**, 17114–17119 (2017).
17. Li, Y. *et al.* A near-infrared non-fullerene electron acceptor for high performance polymer solar cells. *Energy Environ. Sci.* **10**, 1610–1620 (2017).
18. Lin, Y. *et al.* An Electron Acceptor Challenging Fullerenes for Efficient Polymer Solar Cells. *Adv. Mater.* **27**, 1170–1174 (2015).
19. Dai, S. *et al.* Enhancing the Performance of Polymer Solar Cells via Core Engineering of NIR-Absorbing Electron Acceptors. *Adv. Mater.* **30**, 1706571 (2018).
20. Yuan, J. *et al.* Enabling low voltage losses and high photocurrent in fullerene-free organic photovoltaics. *Nat. Commun.* **10**, 570 (2019).

21. Liu, Q. *et al.* Narrow electroluminescence linewidths for reduced nonradiative recombination in organic solar cells and near-infrared light-emitting diodes. *Joule* **5**, 2365–2379 (2021).
22. Huang, X. *et al.* 15.9% organic tandem solar cell with extended near-infrared absorption. *Appl. Phys. Lett.* **116**, 153501 (2020).
23. Li, Y. *et al.* Non-fullerene acceptor organic photovoltaics with intrinsic operational lifetimes over 30 years. *Nat. Commun.* **12**, 1–9 (2021).
24. Huang, X., Fan, D., Li, Y. & Forrest, S. R. Multilevel peel-off patterning of a prototype semitransparent organic photovoltaic module. *Joule* **6**, 1581–1589 (2022).
25. Li, Y., Huang, X., Sheriff, H. K. M. & Forrest, S. R. Semitransparent organic photovoltaics for building-integrated photovoltaic applications. *Nat. Rev. Mater.* **8**, 186–201 (2022).
26. Che, Y., Niazi, M. R., Izquierdo, R. & Perepichka, D. F. Mechanism of the Photodegradation of A-D-A Acceptors for Organic Photovoltaics**. *Angew. Chemie Int. Ed.* **60**, 24833–24837 (2021).
27. Li, M., Zhou, Y., Zhang, J., Song, J. & Bo, Z. Tuning the dipole moments of nonfullerene acceptors with an asymmetric terminal strategy for highly efficient organic solar cells. *J. Mater. Chem. A* **7**, 8889–8896 (2019).
28. Zhao, W. *et al.* Molecular Optimization Enables over 13% Efficiency in Organic Solar Cells. *J. Am. Chem. Soc.* **139**, 7148–7151 (2017).
29. Burlingame, Q. *et al.* Intrinsically stable organic solar cells under high-intensity illumination. *Nature* **573**, 394–397 (2019).
30. Huang, X., Liu, X., Ding, K. & Forrest, S. R. Is there such a thing as a molecular organic

- alloy? *Mater. Horiz.* **7**, 244–251 (2020).
31. Bartesaghi, D. *et al.* Competition between recombination and extraction of free charges determines the fill factor of organic solar cells. *Nat. Commun.* **6**, 1–10 (2015).
 32. Dibb, G. F. A., Jamieson, F. C., Maurano, A., Nelson, J. & Durrant, J. R. Limits on the fill factor in organic photovoltaics: Distinguishing nongeminate and geminate recombination mechanisms. *J. Phys. Chem. Lett.* **4**, 803–808 (2013).
 33. Rau, U. Reciprocity relation between photovoltaic quantum efficiency and electroluminescent emission of solar cells. *Phys. Rev. B* **76**, 085303 (2007).
 34. Liu, X. *et al.* Efficient Organic Solar Cells with Extremely High Open-Circuit Voltages and Low Voltage Losses by Suppressing Nonradiative Recombination Losses. *Adv. Energy Mater.* **8**, 1801699 (2018).
 35. Xia, Y., Xu, X. & Inganäs, O. Photovoltage loss in semi-transparent organic photovoltaic devices. *Org. Electron.* **74**, 37–40 (2019).
 36. Benduhn, J. *et al.* Intrinsic non-radiative voltage losses in fullerene-based organic solar cells. *Nat. Energy* **2**, 1–6 (2017).
 37. Vandewal, K., Tvingstedt, K., Gadisa, A., Inganäs, O. & Manca, J. V. On the origin of the open-circuit voltage of polymer–fullerene solar cells. *Nat. Mater.* **8**, 904–909 (2009).
 38. Deibel, C. *et al.* Role of the Charge Transfer State in Organic Donor–Acceptor Solar Cells. *Adv. Mater.* **22**, 4097–4111 (2010).
 39. Forrest, S. R., Bradley, D. D. C. & Thompson, M. E. Measuring the Efficiency of Organic Light-Emitting Devices. *Adv. Mater.* **15**, 1043–1048 (2003).
 40. Giebink, N. C., Wiederrecht, G. P., Wasielewski, M. R. & Forrest, S. R. Ideal diode equation for organic heterojunctions. I. Derivation and application. *Phys. Rev. B* **82**, 1–12

(2010).

41. Arneson, C. *et al.* Relationship between charge transfer state electroluminescence and the degradation of organic photovoltaics. *Appl. Phys. Lett.* **118**, 63301 (2021).

Chapter 4

Impact of Dipolar Molecules on the Reliability of Ternary Organic Photovoltaic Cells

In Chapter 3, we have shown that blending two non-fullerene acceptors (NFAs) to form bulk heterojunctions (BHJs) in ternary OPVs leads to an end-capping exchange reaction that results in the generation of several, new dipolar species whose impact on OPV operational stability remains uncertain. In this chapter, we investigate the reliability of a ternary OPV system intentionally blended with dipolar NFA molecules that are among the end-capping exchange reaction products. We reveal that an intrinsic contribution to OPV degradation is the reorganization and reorientation of the dipolar molecules during operation, which leads to an increased dielectric constant (ϵ_r). The ϵ_r of a BHJ lacking dipolar NFAs is relatively stable over 240 h under illumination at 10 suns intensity, while a BHJ with 50% dipolar NFAs shows a $7.7 \pm 0.8\%$ increase. Consequently, the electric field across the BHJ with dipolar molecules decreases compared to that of a non-dipolar BHJ under the same applied voltage, leading to an $8.3 \pm 0.9\%$ reduction in charge collection efficiency, while the decrease is only $2.2 \pm 0.4\%$ in devices containing only nonpolar molecules. This result has implications on the stability of a range of organic electronic devices containing dipolar molecules.

4.1 Introduction

By introducing dipolar molecules in the BHJs of OPVs, the PCE can be improved due to the change of intramolecular electron-hole separation as well as a modified molecular packing.¹⁻⁴ The past few decades have witnessed substantial developments in employing dipolar materials in OPVs such as donor-acceptor-acceptor' (d-a-a') type small molecule donors,^{2,5-9} and asymmetric NFAs.^{1,4,10-14} However, it has been shown in Chapter 3 that end-capping reactions between two acceptor-donor-acceptor (A-D-A) type NFAs in ternary OPVs can generate dipolar reaction products that reduce the device operational stability.¹⁵

In this chapter, we explore the impact of dipolar molecules on device reliability by studying a ternary OPV system intentionally blended with dipolar molecules that are among the products of end-capping exchange reactions. We find that the devices with a higher ratio of dipolar constituents show a larger decrease in charge collection efficiency (η_{CC}) and PCE after aging compared to devices with fewer or no dipolar components. Here, η_{CC} is the ratio between the photocurrent, J_{ph} (V), at voltage, V , and the saturated photocurrent, $J_{ph,sat}$, at large reverse bias. We attribute these changes to an increase in the relative dielectric constant (ϵ_r) in the dipolar BHJ, which in turn, leads to a decrease in the internal electric field. Measurements suggest that the ϵ_r of the BHJ (ϵ_{BHJ}) containing only nonpolar molecules remains stable after 240h aging under white light illumination at 10 suns intensity, while it significantly increases under the same conditions when the medium contains dipolar molecules. To understand the origin of the change in ϵ_r , we performed Monte Carlo simulations of dipoles orientations that indicate the dipolar molecules tend to aggregate and align anti-parallel to neighboring molecules, which accurately predicts the change in η_{CC} , and hence the PCE, during extended periods of device operation.

4.2 Theoretical Calculation of Dipolar Molecules Reorganization

4.2.1 Theory

When the devices undergo aging, dipolar molecules in the BHJ can reorganize and reorient to reach lower energy configurations,¹⁶ see Fig. 4.1(a). The energy due to dipole-dipole interactions is calculated using the dipole interaction energy:

$$E = \sum \frac{1}{4\pi\epsilon_r\epsilon_0 r_{ij}^3} [\vec{p}_i \cdot \vec{p}_j - 3(\vec{p}_i \cdot \hat{r}_{ij})(\vec{p}_j \cdot \hat{r}_{ij})], \quad (4.1)$$

where ϵ_r is the relative dielectric constant of the medium, ϵ_0 is the vacuum permittivity, r_{ij} is the distance between the i^{th} and j^{th} molecules, \hat{r}_{ij} is the unit vector between them, and \vec{p}_i and \vec{p}_j are their dipole moments. The total dipole moment is the sum of permanent, \vec{p}_0 , and induced dipoles, $\vec{p} = \vec{p}_0 + \alpha\vec{F}$, with polarizability, α , and electric field, \vec{F} . The reorganization of dipoles within a layer over time results in a change in the screening of electric field, which is reflected by a change in the dielectric constant.

As shown in Fig. 4.1(b), assuming a uniform electric field within each layer, and the normal displacement field is constant across the layer interfaces, the voltage V across the OPV is described by:

$$V = \frac{\Delta E_{HL}}{q} - F_{BHJ}d_{BHJ} - F_{HTL}d_{HTL} - F_{ETL}d_{ETL} - \delta_{e1} - \delta_{e2} - \delta_{h1} - \delta_{h2}, \quad (4.2)$$

and
$$\epsilon_{HTL}F_{HTL} = \epsilon_{BHJ}F_{BHJ} = \epsilon_{ETL}F_{ETL}, \quad (4.3)$$

where ΔE_{HL} is the energy offset between the HOMO of the donor and the LUMO of the acceptor, q is the electron charge, F_{BHJ} , F_{HTL} , F_{ETL} are the normal electric fields across the BHJ, hole transporting layer (HTL), and electron transporting layer (ETL), respectively, d_{BHJ} , d_{HTL} and d_{ETL} are the thicknesses of the corresponding three layers, ϵ_{BHJ} , ϵ_{HTL} and ϵ_{ETL} are their relative dielectric constants, and δ_{e1} , δ_{e2} , δ_{h1} and δ_{h2} are the voltages across various interfaces in Fig. 4.1(b) whose

dependence on V is negligible in the absence of large density of interfacial trap states.^{17,18} When there is no electric field across the BHJ, the probability for photocurrent generation is low due to lack of driving force to help photogenerated charges overcome Coulomb attraction and guide them towards electrodes. Therefore, we approximate that the photocurrent density, $J_{ph}=0$, when $F_{BHJ} = F_{HTL} = F_{ETL} = 0$.¹⁸ Then, Eq. 4.2 becomes:

$$V|_{J_{ph}=0} = \frac{\Delta E_{HL}}{q} - \delta_{e1} - \delta_{e2} - \delta_{h1} - \delta_{h2}. \quad (4.4)$$

Therefore, F_{BHJ} is given by:

$$F_{BHJ} = \left(V|_{J_{ph}=0} - V \right) / \left(\frac{\varepsilon_{BHJ}}{\varepsilon_{HTL}} d_{HTL} + d_{BHJ} + \frac{\varepsilon_{BHJ}}{\varepsilon_{ETL}} d_{ETL} \right). \quad (4.5)$$

It is apparent from Eq. 4.5 that an increased ε_{BHJ} can reduce the electric field across the BHJ, leading to a reduced η_{CC} .

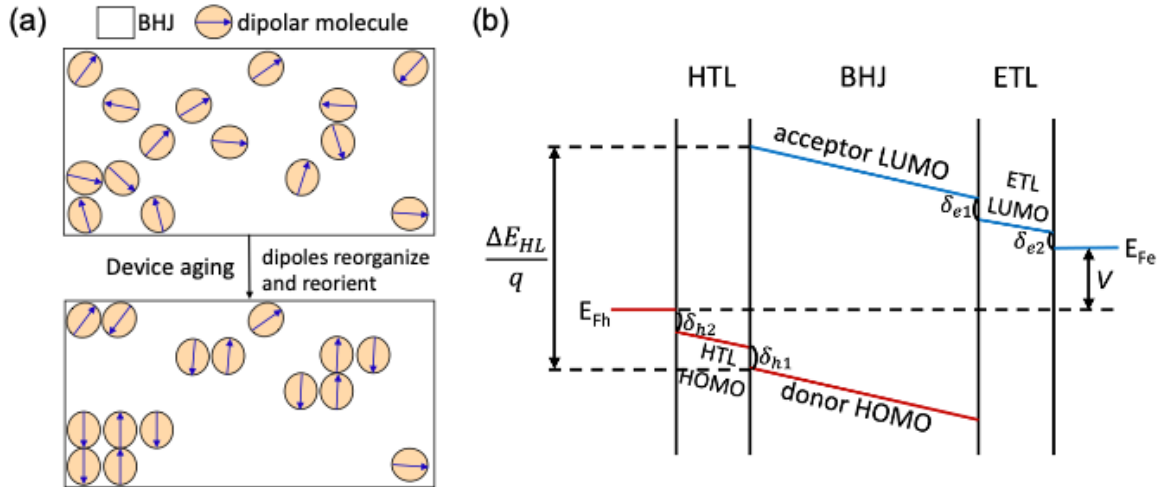


Figure 4.1 Dipolar molecules reorganization and electric field distribution in OPVs.

(a) Illustration of dipolar molecule reorganization in the BHJ of OPV during device operation to reach lower energy configurations. (b) Energy level diagram of an OPV at applied voltage V , including voltage drops across the BHJ, the charge transporting layers, and various interfaces.

4.2.2 Simulated Reorganization of Dipoles

A Monte Carlo-based simulated annealing (SA) protocol is used to model dipolar

reorganization in the thin film of acceptor blends.^{19–23} The simulation begins with a random distribution and orientation of dipolar molecules, and performs step-wise trial moves and rotations on the dipoles. Each step that lowers the system energy is accepted, whereas the probability for endothermic steps is weighted by a Boltzmann factor.²⁴ The simulation assumes that the molecules are located at the grid points of simple cubic lattice comprising $30 \times 30 \times 100$ sites with lattice constant of 1 nm and periodic boundary conditions. The molecular dipoles are approximated as point dipoles. Thermal equilibrium is approached after millions of Monte Carlo steps of trial dipole translations and rotations to reach system energy fluctuation of $< 1\%$.

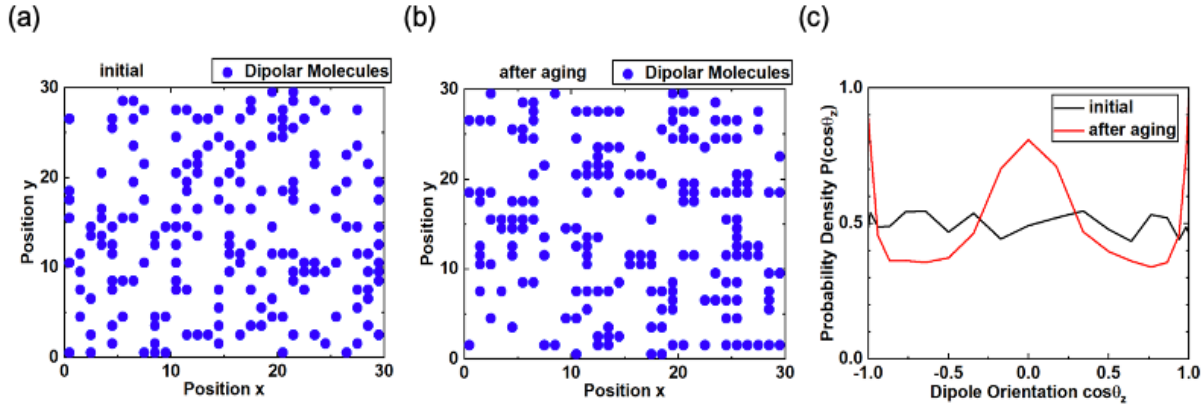


Figure 4.2 Simulated morphology of an acceptor blend containing dipolar molecules.

The plan view of the simulated distribution of 20% dipolar molecules in an acceptor blend (a) before and (b) after aging. (c) Simulated probability density distribution of dipole orientations before and after aging.

Figures 4.2(a) and (b) show the simulated morphology of an acceptor blend with 20% dipolar molecules before and after aging, respectively. The plan views are taken halfway through the solid at location $z = 50$. Figure 4.2(a) is the plan view of the initial distribution of dipoles, whereas the dipoles form clusters after the system approaches equilibrium following SA, as shown in Fig. 4.2(b). The normalized probability density distribution of the dipolar orientation, defined by the angle between the dipole moment and the substrate normal, θ_z , before and after SA is illustrated in Fig. 4.2(c). The orientation of dipoles after aging shows higher probability at $\theta_z =$

0 , $\pm \frac{\pi}{2}$ and π , due to anti-parallel dipole alignment between neighboring molecules.

4.2.3 Calculation of Dielectric Constant Change

The dielectric constant is calculated by treating the acceptor blend as a parallel plate capacitor. We assume an initial relative dielectric constant $\epsilon_{r,0} = 3$ in the absence of dipoles. The capacitive device is charged by an external voltage V_{ext} , after which it is disconnected from the power source, and the dipoles are allowed to reorient. This generates an internal voltage, V_{int} , which reduces the electric field across the acceptor blend of magnitude $V_{acc} = V_{ext} - V_{int}$. Therefore, by calculating the relationship between V_{int} and V_{acc} , the relative dielectric constant, ϵ_r , of the blend containing dipolar molecules is obtained using: $\epsilon_r/\epsilon_{r,0} = V_{ext}/V_{acc} = 1 + V_{int}/V_{acc}$. Therefore, the change in the dielectric constant over time, t , is given by $(\epsilon_r(t) - \epsilon_{r,0})/(\epsilon_r(0) - \epsilon_{r,0}) = V_{int}(t)/V_{int}(0)$, where $\epsilon_{r,0}$ is the relative dielectric constant of the non-dipolar medium, and $V_{int}(t)$ is the internal voltage due to the addition of dipoles.

The change in ϵ_r is then found by calculating V_{int} induced by dipoles based on the dipolar configurations illustrated in Fig. 4.2. As shown in Fig. 4.3(a), the NFA blend with 20% dipolar content experiences 5.6% increase in ϵ_r . As ϵ_r of the polymer donor (40 wt.% in the BHJ) is unchanged, ϵ_{BHJ} is increased by only 3.3%. With higher ratio of dipolar contents, similar calculations result in an increase of 5.0% in ϵ_{BHJ} for a 33% dipolar concentration and 7.0% increase for a 50% dipolar concentration.

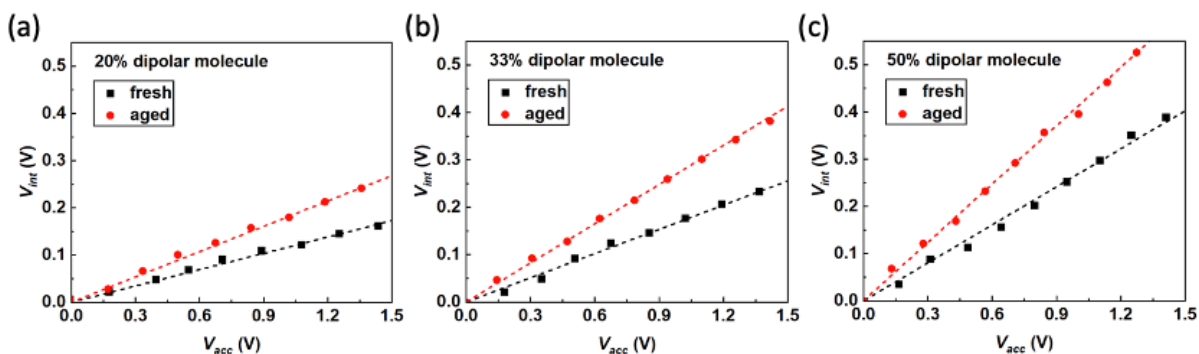


Figure 4.3 Calculation of internal voltages induced by dipolar molecules.

Relationship between the internal voltage (V_{int}) and the voltage across the NFA blends (V_{acc}) containing (a) 20%, (b) 33% and (c) 50% of dipolar molecules BTCIC-IC.

4.3 Impact of Dipolar Molecules on Ternary OPVs Reliability

4.3.1 Experimental Methods

To systematically investigate the impact of dipolar molecules on device stability, we fabricated ternary OPVs comprising one polymer donor, PCE-10, and two nonpolar NFAs, BT-IC and BT-CIC. Their end-capping exchange product, the dipolar molecule BTCIC-IC,¹⁵ is blended into the NFAs with ratios of 0%, 20%, 33% and 50%. As shown quantitatively in the previous chapter, such concentrations of dipolar products are in fact present in NFA based ternary devices. The devices employ ITO as bottom cathode, ZnO as ETL, MoOx as HTL and Al as top anode, the C₇₀ and IC-SAM buffer layers are inserted between the BHJ and charge transporting layers to prevent chemical reactions at interfaces.²³

Glass substrates with pre-patterned ITO were detergent- and solvent-cleaned followed by CO₂ snow cleaning and exposure to ultraviolet-ozone for 15 min. A ZnO precursor solution was spin-coated onto the substrate at 3000 rpm after filtration through a 0.45 μm pore polytetrafluoroethylene (PTFE) filter, and then baked at 160°C in air for 30 min. The samples were then transferred into a N₂ glovebox (O₂ < 0.1 ppm, H₂O < 0.1 ppm). The IC-SAM was dissolved

in methanol with a concentration of 1 mg/ml and spin coated at 4000 rpm for 60s, followed by thermal annealing at 110°C for 10 min. Then, the IC-SAM was washed with methanol to remove residues. The active layer solution was prepared by dissolving PCE-10 in a hot chlorobenzene solution at 65°C overnight, and then cooling to room temperature and mixing with BT-IC, BT-CIC and BTCIC-IC in a donor:acceptor = 1:1.5 ratio with a total concentration of 18 mg/mL. The solution was similarly filtered before spin-coated onto the substrate at 2000 rpm for 90s to achieve a thickness of 80 nm. Active layers for capacitance-voltage ($C-V$) measurements were spin-coated at 1000 rpm to achieve a film thickness of 95 nm. The samples were then transferred into a high vacuum chamber (base pressure $\sim 10^{-7}$ Torr) for thermal evaporation of 2 nm C_{70} , 15 nm MoO_3 and 100 nm Al at a rate of 0.2 Å/s. All devices were encapsulated before characterization by bonding a cover glass to the substrate with an ultraviolet-curable epoxy bead around the device periphery. The $J-V$ characteristics and EQE of the cells were measured in a glovebox, with procedures same as in previous chapters. The $C-V$ characteristics were measured in the dark from 0 to 6V reverse bias at 0.05V step with 50mV, 10kHz AC measurement potential (Keithley SCS-4200 Semiconductor Analyzer). The device stability test was performed under white LED at equivalent solar intensity was 10 suns and the OPV cells were actively water-cooled to $35 \pm 5^\circ\text{C}$ during aging.

4.3.2 Impact on Dielectric Constant

Figure 4.4 shows the capacitance-voltage ($C-V$) characteristics of a device with 0% (BT-IC:BT-CIC:BTCIC-IC = 1:1:0), 20% (BT-IC:BT-CIC:BTCIC-IC = 2:2:1), 33% ((BT-IC:BT-CIC:BTCIC-IC = 1:1:1) and 50% (BT-IC:BT-CIC:BTCIC-IC = 1:1:2) dipolar molecules before and after 240 h aging under white light illumination at 10 suns intensity.

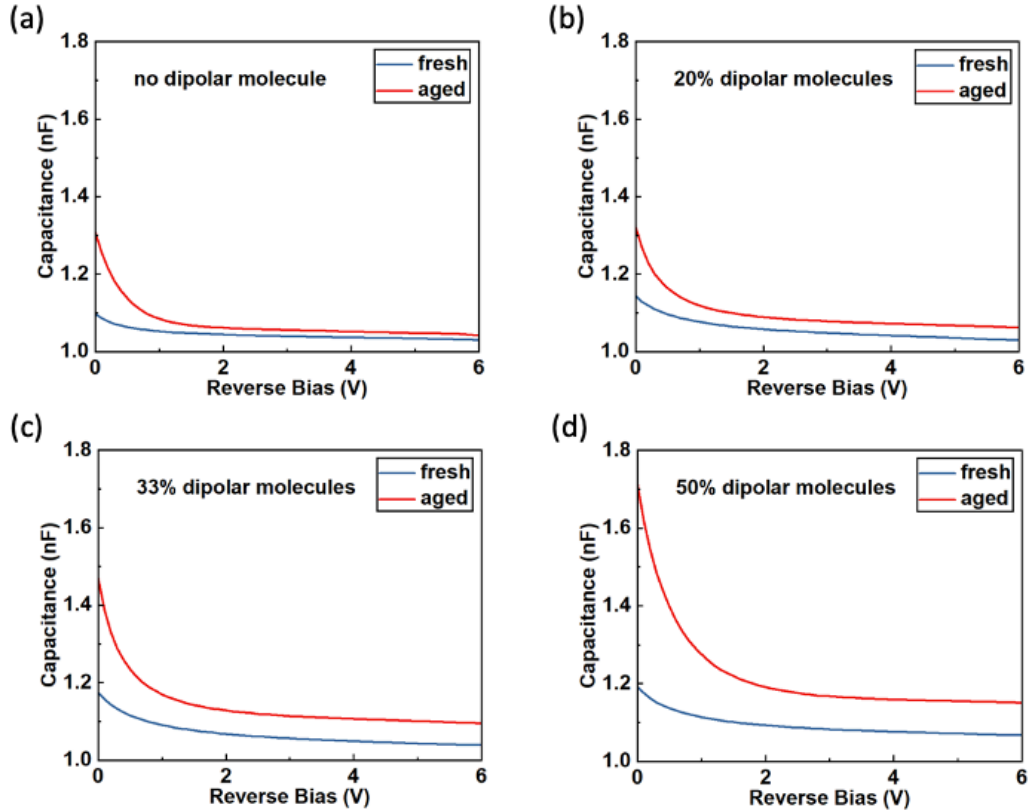


Figure 4.4 Capacitance-voltage (C - V) characteristics of devices with different ratios of dipolar molecules. Capacitance-voltage characteristics of OPV devices before and after 240h aging under illumination at 10 suns intensity with BT-IC:BT-CIC:BTCIC-IC ratios of (a) 1:1:0, no dipolar molecule, (b) 2:2:1, 20% dipolar molecules, (c) 1:1:1, 33% dipolar molecules, and (d) 1:1:2, 50% dipolar molecules.

Figure 4.5(a) summarizes the capacitance of devices containing different NFA compositions before and after aging. The dielectric constant is determined assuming the fully depleted reverse-biased diodes (at $-6V$) are parallel plate capacitors. When there is no dipolar component in the BHJ (BT-IC:BT-CIC:BTCIC-IC = 1:1:0), C (and hence, ϵ_{BHJ}) before and after aging is unchanged at 1.03 ± 0.01 nF, while ϵ_{BHJ} increases by $7.7 \pm 0.8\%$ for a dipolar concentration of 50%. In Fig. 4.5(b), the dashed line represents the simulated increase in ϵ_{BHJ} vs. dipolar concentration, which is consistent with that obtained from the C - V measurements, indicating that the changes in ϵ_{BHJ} can primarily be attributed to the reorganization and reorientation of dipolar molecules over time.

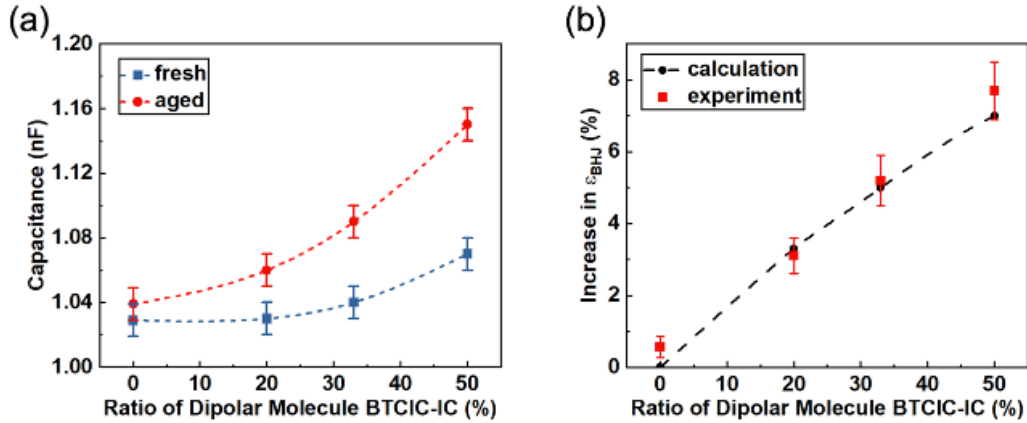


Figure 4.5 Summary of capacitance and relative dielectric constant before and after aging.
 (a) Capacitance of OPVs vs. dipolar NFA concentration, before and after 240h aging. (s) Calculated and measured (from C - V data) increase in the relative dielectric constants (ϵ_r) of BHJs vs. BTCIC-IC ratio.

In addition, as shown in Fig. 4.6, the carrier density calculated from C - V measurements at 0V of the device containing 50% dipolar molecules decreases by $21 \pm 3\%$ compared to that without dipolar content, suggesting that the dipolar molecules may trap charges in the BHJ.

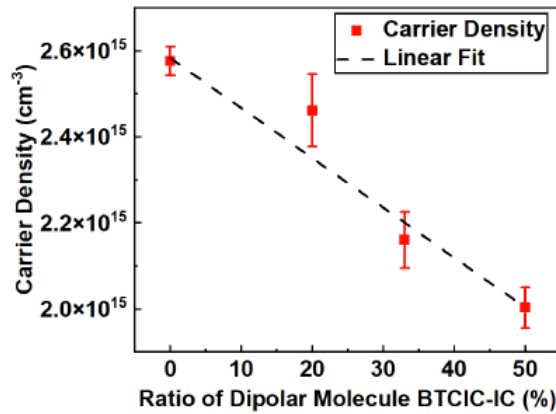


Figure 4.6 Carrier densities of OPV devices with different ratios of dipolar molecules.
 Carrier densities of devices containing different blend ratios of dipolar NFAs after 240h aging under white light illumination at 10 suns intensity, the dashed line is the linear fit of carrier density vs. dipolar ratio.

4.3.3 Impact on Device Reliability and Charge Collection Efficiency

The evolution of device performance under white light illumination at 10 suns intensity is shown in Figs. 4.7(a)-(d). The aging under high intensity illumination accelerates the degradation to distinguish differences between devices stability in a reasonable amount of time. The

degradation under such condition was found to accurately reflect the degradation under AM1.5G illumination with appropriate acceleration factor.^{25–27} Compared to the device lacking dipolar content where PCE is reduced by $15.5 \pm 0.8\%$ after 240h, the devices comprising 20%, 33% and 50% dipolar NFAs show reductions of $18.9 \pm 1.2\%$, $21.1 \pm 1.1\%$ and $23.2 \pm 1.4\%$, respectively. While the open-circuit voltage (V_{OC}) remains relatively constant, the short-circuit current (J_{SC}) and fill factor (FF) decrease more in devices containing dipolar molecules. Figure 4.7(e) shows the decrease of η_{CC} (at $V = 0$) where devices with 20%, 33% and 50% dipolar molecules experience a $4.2 \pm 0.5\%$, $6.2 \pm 0.4\%$ and $8.3 \pm 0.9\%$ decrease in η_{CC} (at $V = 0$) over the aging period, whereas only a $2.2 \pm 0.4\%$ reduction is observed in the nonpolar device.

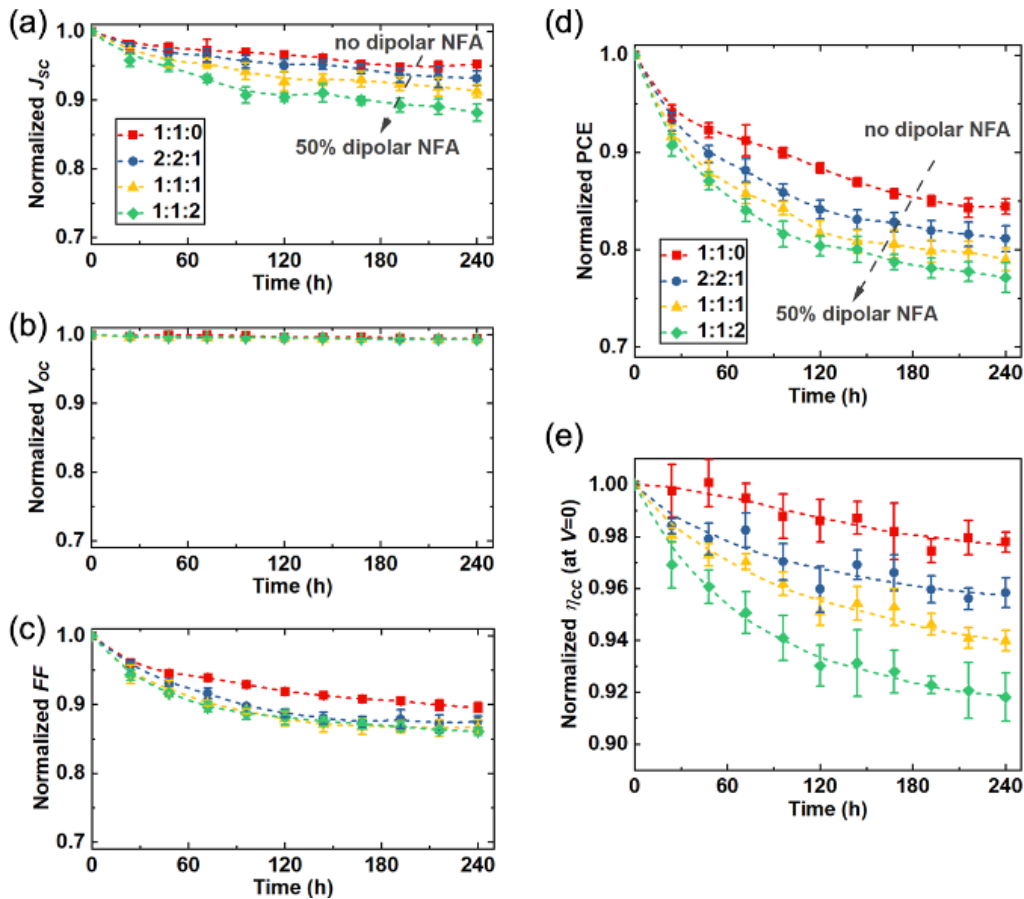


Figure 4.7 Device performance degradation under 10 suns intensity illumination.

Degradation in (a) J_{sc} , (b) V_{oc} , (c) FF , (d) PCE and (e) charge collection efficiency (η_{CC} , at $V=0$) of OPV devices with different blend ratios BT-IC:BT-CIC:BTCIC-IC over 240h aging under white light illumination at 10 suns intensity.

Figure 4.8(a) shows the measured as-grown and aged η_{CC} vs. V of a device with 20% BTCIC-IC, as well as the calculated reduction in η_{CC} using Eq. 4.5 based on increased dielectric constant over time. Here, we assume the reduction of η_{CC} is the same for all devices with and without dipolar molecules at the same F_{BHH} . The calculated η_{CC} vs. V of OPVs with 20% dipolar molecule is shown as dashed lines, which is consistent with measurement. Figure 4.8(b) summarizes the measured and calculated changes in η_{CC} (at $V=0$) vs. dipolar concentration. The agreement between calculation and experiment indicates that the loss in η_{CC} of devices containing dipolar molecules is primarily due to the increased ϵ_{BHH} and the corresponding reduction in F_{BHH} .

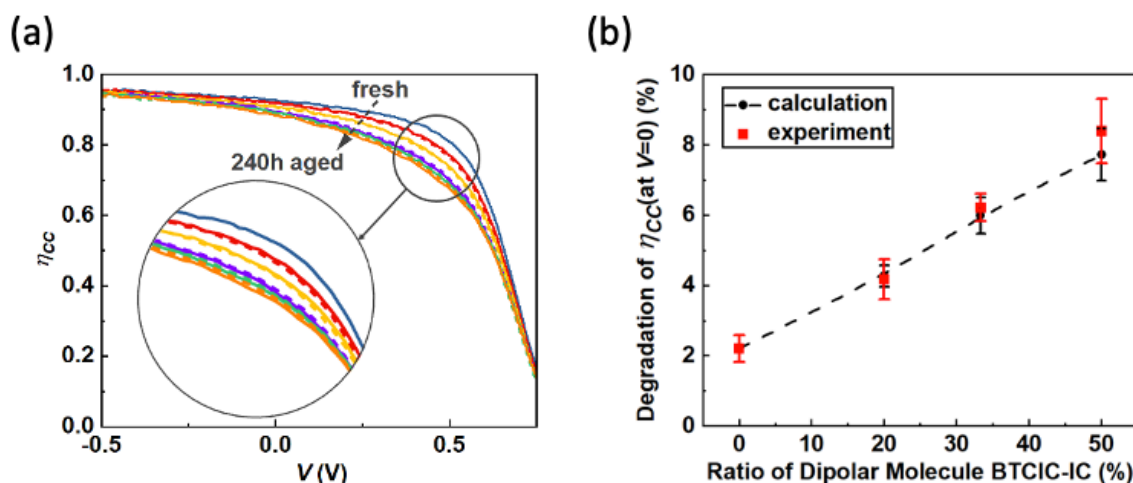


Figure 4.8 Evolution of charge extraction efficiency under 10 suns intensity illumination.

(a) Measured η_{CC} vs. V (solid lines) of OPVs comprising 20% dipolar NFA with time, along with calculated characteristics (dashed lines) of the aged device. The inset is a magnified view of the curves around the maximum power point. (b) Measured and calculated degradation in η_{CC} (at $V = 0$) after 240h aging of OPVs vs. ratios of dipolar BTCIC-IC.

Recently, studies of multilayer OLEDs have also revealed polarization-induced charge accumulation at layer interfaces resulting from the presence of dipolar molecules,^{25–32} as well as the reorientation of dipoles during operation and its effect on device stability.^{33–35} Those investigations have primarily focused on the exciton-polaron quenching and charge injection at interfaces dominated by interfacial charges. In contrast, our work reveals that dipolar molecules

affect the electric field distribution in the bulk of the OPVs. In both cases, our work suggests that dipolar reorganization can result in unstable performance in a range of organic electronic devices.

It should be noted here that we demonstrated the impact of dipolar molecules on OPV reliability, while this is not the only mechanism contributing to reduced device performance over time. For example, the constituents arising from end-capping exchange might lead to faster degradation compared to the intentionally blended molecules discussed in this work, even though they have the same dipolar components.¹⁶ This indicates that the interactions between NFAs during solution preparation may lead to other degradation mechanisms than those studied here. Moreover, the stability comparison between different material systems should not be based solely on the concentration of dipole moments. Other aspects such as chemical or thermal stability may also play important role on device reliability.

4.4 Conclusion

In this chapter, we demonstrated that dipolar molecules in the BHJ of OPVs aggregate and align anti-parallel to neighboring molecules during device aging, resulting in increased dielectric constant, which in turn, reduces the electric field across the BHJ. This change manifests itself in a decreased charge collection, and hence power conversion efficiency of the OPV. With higher ratio of dipolar molecules in the BHJ, the increase in ϵ_r as well as the loss in η_{CC} and PCE are intensified. The forgoing analysis suggests that dipolar molecules in organic electronic devices can negatively impact their operational stability due to their time-dependent reorientation that affects the electric field within the thin films of which they are comprised.

Chapter 4

Bibliography

1. Song, J. & Bo, Z. Asymmetric molecular engineering in recent nonfullerene acceptors for efficient organic solar cells. *Chinese Chem. Lett.* 108163 (2023).
doi:10.1016/J.CCLET.2023.108163
2. Griffith, O. L. *et al.* Charge transport and exciton dissociation in organic solar cells consisting of dipolar donors mixed with C₇₀. *Phys. Rev. B - Condens. Matter Mater. Phys.* **92**, 085404 (2015).
3. Liu, X., Li, Y., Ding, K. & Forrest, S. Energy loss in organic photovoltaics: Nonfullerene versus fullerene acceptors. *Phys. Rev. Appl.* **11**, 024060 (2019).
4. Li, D., Sun, C., Yan, T., Yuan, J. & Zou, Y. Asymmetric Non-Fullerene Small-Molecule Acceptors toward High-Performance Organic Solar Cells. *ACS Cent. Sci.* **7**, 1787–1797 (2021).
5. Che, X., Li, Y., Qu, Y. & Forrest, S. R. High fabrication yield organic tandem photovoltaics combining vacuum- and solution-processed subcells with 15% efficiency. *Nat. Energy* **3**, 422–427 (2018).
6. Che, X. *et al.* Donor–Acceptor–Acceptor’s Molecules for Vacuum-Deposited Organic Photovoltaics with Efficiency Exceeding 9%. *Adv. Energy Mater.* **8**, 1703603 (2018).
7. Liu, F. *et al.* Efficient Polymer Solar Cells Based on a Low Bandgap Semi-crystalline DPP Polymer-PCBM Blends. *Adv. Mater.* **24**, 3947–3951 (2012).
8. Lin, L.-Y. *et al.* A Low-Energy-Gap Organic Dye for High-Performance Small-Molecule Organic Solar Cells. *J. Am. Chem. Soc.* **133**, (2011).
9. Zhang, T. *et al.* Impact of Thermal Annealing on Organic Photovoltaic Cells Using

- Regioisomeric Donor-Acceptor-Acceptor Molecules. *ACS Appl. Mater. Interfaces* **9**, 25418–25425 (2017).
10. Zhan, L. *et al.* Desired open-circuit voltage increase enables efficiencies approaching 19% in symmetric-asymmetric molecule ternary organic photovoltaics. *Joule* **6**, 662–675 (2022).
 11. He, C. *et al.* Compromising Charge Generation and Recombination with Asymmetric Molecule for High-Performance Binary Organic Photovoltaics with Over 18% Certified Efficiency. *Adv. Funct. Mater.* **32**, 2112511 (2022).
 12. Tang, C. *et al.* High-Performance Ladder-Type Heteroheptacene-Based Nonfullerene Acceptors Enabled by Asymmetric Cores with Enhanced Noncovalent Intramolecular Interactions. *Angew. Chemie Int. Ed.* **60**, 19314–19323 (2021).
 13. He, C. *et al.* Asymmetric electron acceptor enables highly luminescent organic solar cells with certified efficiency over 18%. *Nat. Commun. 2022 131* **13**, 1–11 (2022).
 14. Wang, J. *et al.* An acceptor with an asymmetric and extended conjugated backbone for high-efficiency organic solar cells with low nonradiative energy loss. *J. Mater. Chem. A* **10**, 16714–16721 (2022).
 15. Li, Y. *et al.* Interactions between non-fullerene acceptors lead to unstable ternary organic photovoltaic cells. *Proc. Natl. Acad. Sci.* **120**, e2301118120 (2023).
 16. Burlingame, Q., Ball, M. & Loo, Y. L. It's time to focus on organic solar cell stability. *Nat. Energy* **5**, 947–949 (2020).
 17. Bhattacharya, P. *Semiconductor Optoelectronic Devices*. (Prentice Hall, 1997).
 18. Ding, K., Huang, X., Li, Y. & Forrest, S. R. Photogeneration and the bulk quantum efficiency of organic photovoltaics. *Energy Environ. Sci.* **14**, 1584–1593 (2021).

19. Kirkpatrick, S., Gelatt, C. D. & Vecchi, M. P. Optimization by Simulated Annealing. *Science (80-.)*. **220**, 671–680 (1983).
20. Neumann, T., Danilov, D., Lennartz, C. & Wenzel, W. Modeling disordered morphologies in organic semiconductors. *J. Comput. Chem.* **34**, 2716–2725 (2013).
21. Friederich, P., Coehoorn, R. & Wenzel, W. Molecular Origin of the Anisotropic Dye Orientation in Emissive Layers of Organic Light Emitting Diodes. *Chem. Mater.* **29**, 9528–9535 (2017).
22. Coehoorn, R., Lin, X., Weijtens, C. H. L., Gottardi, S. & Van Eersel, H. Three-Dimensional Modeling of Organic Light-Emitting Diodes Containing Molecules with Large Electric Dipole Moments. *Phys. Rev. Appl.* **16**, 034048 (2021).
23. Groves, C. & Greenham, N. C. Monte Carlo Simulations of Organic Photovoltaics. *Top Curr Chem* **352**, 257–278 (2013).
24. Metropolis, N., Rosenbluth, A. W., Rosenbluth, M. N., Teller, A. H. & Teller, E. Equation of State Calculations by Fast Computing Machines. *J. Chem. Phys.* **21**, 1087 (2004).
25. Haillant, O., Dumbleton, D. & Zielnik, A. An Arrhenius approach to estimating organic photovoltaic module weathering acceleration factors. *Sol. Energy Mater. Sol. Cells* **95**, 1889–1895 (2011).
26. Li, Y. *et al.* Non-fullerene acceptor organic photovoltaics with intrinsic operational lifetimes over 30 years. *Nat. Commun.* **12**, 1–9 (2021).
27. Burlingame, Q. *et al.* Intrinsically stable organic solar cells under high-intensity illumination. *Nature* **573**, 394–397 (2019).
28. Afolayan, E. O. *et al.* Reducing Spontaneous Orientational Polarization via Semiconductor Dilution Improves OLED Efficiency and Lifetime. *Phys. Rev. Appl.* **17**,

- L051002 (2022).
29. He, S., Pakhomenko, E. & Holmes, R. J. Process Engineered Spontaneous Orientation Polarization in Organic Light-Emitting Devices. *ACS Appl. Mater. Interfaces* **15**, (2022).
 30. Pakhomenko, E. & Holmes, R. J. The role of OLED emissive layer polarization in sub-turn-on charge accumulation. *Proc. SPIE 12208, Org. Hybrid Light Emit. Mater. Devices XXVI* **122080A**, (2022).
 31. Esaki, Y., Tanaka, M., Matsushima, T. & Adachi, C. Active Control of Spontaneous Orientation Polarization of Tris(8-hydroxyquinolato)aluminum (Alq3) Films and Its Effect on Performance of Organic Light-Emitting Diodes. *Adv. Electron. Mater.* **7**, 2100486 (2021).
 32. Noguchi, Y., Brütting, W. & Ishii, H. Spontaneous orientation polarization in organic light-emitting diodes. *Jpn. J. Appl. Phys.* **58**, SF0801 (2019).
 33. Noguchi, Y. *et al.* Charge accumulation at organic semiconductor interfaces due to a permanent dipole moment and its orientational order in bilayer devices. *J. Appl. Phys.* **111**, 114508 (2012).
 34. Pakhomenko, E., He, S. & Holmes, R. J. Polarization-Induced Exciton–Polaron Quenching in Organic Light-Emitting Devices and Its Control by Dipolar Doping. *Adv. Opt. Mater.* **10**, 2201348 (2022).
 35. Baldo, M. A. & Forrest, S. R. Interface-limited injection in amorphous organic semiconductors. *Phys. Rev. B* **64**, 085201 (2001).
 36. Schmidt, T. D., Jäger, L., Noguchi, Y., Ishii, H. & Brütting, W. Analyzing degradation effects of organic light-emitting diodes via transient optical and electrical measurements. *J. Appl. Phys.* **117**, 215502 (2015).

37. Scholz, S., Kondakov, D., Lüssem, B. & Leo, K. Degradation mechanisms and reactions in organic light-emitting devices. *Chem. Rev.* **115**, 8449–8503 (2015).
38. Yamada, T., Zou, D., Jeong, H., Akaki, Y. & Tsutsui, T. Recoverable degradation and internal field forming process accompanied by the orientation of dipoles in organic light emitting diodes. *Synth. Met.* **111–112**, 237–240 (2000).

Chapter 5

Ternary Tandem Organic Photovoltaic with Extended Near-infrared Absorption

Stacking single-junction organic solar cells is effective in increasing the PCE by reducing the thermalization loss and increasing the open circuit voltage. Recent developments of non-fullerene acceptors (NFAs) offer a range of materials whose energy gaps are suited for absorbing relatively narrow slices of the solar spectrum, thus easing requirements for current balance between sub-elements in the multi-junction stacks. In this chapter, we demonstrate a solution-processed tandem organic solar cell comprising a binary, visible-absorbing sub-cell and a ternary near-infrared (NIR) absorbing sub-cell. The ternary NIR sub-cell utilizes a narrow energy gap NFA acceptor that enables broadened and increased absorption compared to a binary NIR sub-cell. An isopropanol surface treatment is developed to connect the hydrophilic-hydrophobic surfaces in the charge recombination zone (CRZ) located between the sub-cells. The nearly optically and electrically lossless CRZ combined with an anti-reflection coating results in a tandem OPV with $\text{PCE} = 15.9 \pm 0.2 \%$ under AM1.5G simulated illumination.

5.1 Introduction

OPVs are considered a promising means for solar energy harvesting due to their potential for low-cost, lightweight, transparency and flexibility.¹⁻⁴ By stacking wide and narrow energy gap cells into multi-junction devices, the PCE can exceed the thermodynamic limit of single-junction devices due to their broader absorption spectral range with less thermalization losses and increased open circuit voltage.⁵⁻¹⁰ Solution processed NFAs based on conjugated thiophene backbones have also provided a variety of molecules with spectral coverage useful for achieving current balance in multi-junction solar cells while being compatible with a diversity of donor molecules.¹¹⁻¹⁴ In this work, we demonstrate a high efficiency tandem OPV structure that comprises one binary and one ternary solution-processed sub-cell. The development of NIR absorbing NFA molecules with long wavelength (>1000 nm) cutoffs is critical to achieving a high PCE.^{8,15-19} Here, we utilize a narrow energy gap NFA BEIT-4F that provides absorption at wavelengths up to 1050 nm when combined with donor PCE-10, which enables the tandem solar cell to achieve broad spectral coverage from the blue to the NIR. We introduce a surface treatment with isopropanol to improve wetting without the need to add surfactant into the poly(3,4-ethylenedioxythiophene):poly(styrenesulfonate) (PEDOT:PSS) in the charge recombination zone (CRZ).²⁰ The tandem cell device achieves PCE = 15.2 ± 0.2 % under AM1.5G simulated illumination. In addition, an anti-reflection coating (ARC) is deposited on the glass substrate to further increases the efficiency to 15.9 ± 0.2 %.

5.2 Materials Absorption

The tandem OPV is composed of two sub-cells absorbing in different regions of solar spectrum. For the visible-absorbing sub-cell, we employ a wide energy gap NFA SFT8-4F

combined with the polymer donor, PM6. Figure 5.1(a) presents the normalized thin film absorption spectra of these two molecules. As shown, the absorption of SFT8-4F peaks at 750 nm, after which it decreases rapidly.

The ternary NIR absorbing sub-cell comprises a single donor PCE-10 and two acceptors BT-CIC and BEIT-4F. N-annulated perylene and dithienopicenocarbazole-based derivatives have been successfully applied in efficient dye-sensitized and organic solar cells due to their planar frameworks and electron-donating capabilities.^{16,21–23} As shown in Fig. 5.1(b), the strong electron-donating motif dithienopicenocarbazole was incorporated into the BEIT-4F molecule to shift its absorption into the NIR, which is complementary to the absorption of SFT8-4F. The thin film absorption spectra of the three materials in Fig. 5.1(b) shows that the narrow energy gap NFA BEIT-4F has absorption spectrum which is 50 nm red-shift compared to BT-CIC.

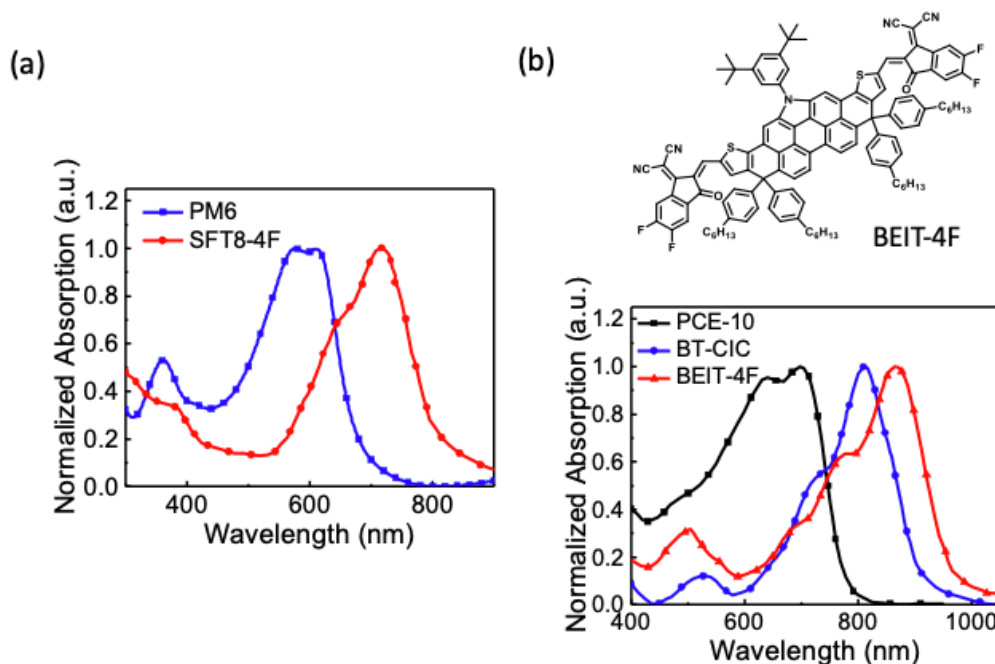


Figure 5.1 Absorption spectra of materials.

(a) Absorption spectra of donor PM6 and acceptor SFT8-4F used in the visible-absorbing sub-cell. (b) Molecular structure of NIR absorbing acceptor BEIT-4F and absorption spectra of donor PCE-10 and acceptors BT-CIC and BEIT-4F of NIR-absorbing sub-cell.

5.3 Ternary NIR Absorbing Sub-cell

5.3.1 Experimental Methods

Device fabrication

The OPVs were grown on a detergent- and solvent-cleaned, 145 nm thick film of ITO, patterned into 2 mm wide stripes on a glass substrate. The ZnO precursor solution was spin-coated onto the substrate at 3000 rpm and baked at 160°C in air for 30 min. The PCE-10:BT-CIC:BEIT-4F solutions with different blend ratios were prepared in CB with 10% chloroform (CF) at a concentration of 16 mg/mL. The solutions were stirred overnight at 65°C at 300 rpm. The active layer was spin-coated on top of ZnO at 2000 rpm for 90s in an ultrapure nitrogen environment ($O_2 < 0.1$ ppm, $H_2O < 0.1$ ppm). The samples were then transferred into a high vacuum chamber (base pressure $\sim 10^{-7}$ Torr) for deposition of a 10 nm thick film MoO_3 at 0.5 Å/s, and a 100 nm Ag was deposited at 0.6 Å/s. The device areas of 2 mm \times 2 mm were defined by the overlap of the patterned ITO anode and the Al cathode that is deposited through a shadow mask.

Device characterization

The $J-V$ and EQE characteristics were measured in a glovebox filled with ultrapure nitrogen. The $J-V$ characteristics were measured through a 4 mm² mask to define illuminated area. Other measurement details are the same as in previous chapters.

PL and EL measurements

The ternary devices were encapsulated with epoxy in an ultrapure nitrogen environment to measure PL and EL in air. For PL measurements, the samples were excited at $\lambda = 442$ nm using a continuous wave He-Cd laser. The spectra were collected using a fiber-coupled monochromator (Princeton Instruments, NJ, USA, Model SP-2300i) equipped with a Si charge-coupled device (CCD) (PIXIS:400). The charge transfer state EL spectra were measured under 3V forward-bias,

collected using a fiber-coupled monochromator equipped with a Si CCD and an InGaAs photoreceiver with sensitivity from $\lambda = 800$ to 1700 nm (Newport, CA, USA, Model 2153). The EL spectra were fit with Gaussian distributions using OriginPro 2017.

5.3.2 Ternary Device Performance

The J - V characteristics under simulated AM1.5G illumination and EQE spectra of ternary devices with different blend ratios are shown in Fig. 5.2(a) and 5.2(b), with detailed device performance data listed in Table 5.1, note that the J_{SC} values are integrated from EQE spectra and reference AM1.5G spectrum to ensure accuracy. Compared to PCE-10:BT-CIC, the PCE-10:BEIT-4F binary OPV shows broader EQE spectrum that absorbs up to 1050 nm, a higher $V_{OC} = 0.754$ V \pm 0.005 V vs. 0.695 V \pm 0.004 V and a lower $FF = 0.56 \pm 0.01$ vs. 0.71 ± 0.01 . As shown in Figs. 5.2(b) and 5.2(c), adjusting the ratio of the two binary heterojunctions gives rise to EQE , V_{OC} and FF that fall between those of the binaries, and change monotonically with the blend ratio.

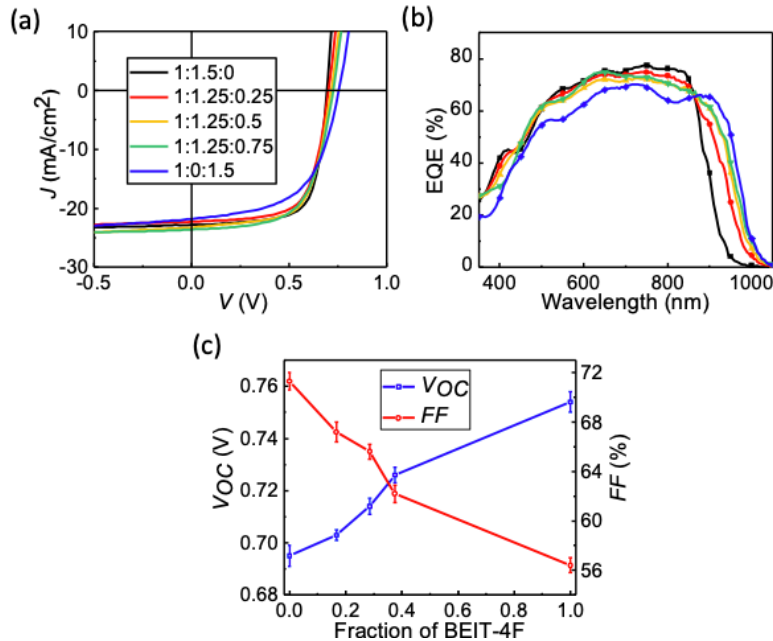


Figure 5.2 Performance of ternary OPVs based on PCE-10:BT-CIC:BEIT-4F with different blend ratios. (a) J - V characteristics under 1 sun, simulated AM1.5G illumination and (b) EQE spectra of ternary cells with different PCE-10:BT-CIC:BEIT-4F blend ratios. (c) V_{OC} and FF as a function of BEIT-4F blend ratio.

Table 5.1 Performance of PCE-10:BT-CIC:BEIT-4F ternary OPVs with different blend ratios under simulated AM1.5G illumination.

PCE-10:BT-CIC:BEIT-4F	J_{sc}^a (mA/cm ²)	V_{oc} (V)	FF	PCE (%)
1:1.5:0	22.5 ± 0.2	0.695 ± 0.004	0.71 ± 0.01	11.0 ± 0.1
1:1.25:0.25	22.2 ± 0.3	0.703 ± 0.003	0.67 ± 0.01	10.5 ± 0.2
1:1.25:0.5	22.6 ± 0.2	0.715 ± 0.003	0.65 ± 0.01	10.9 ± 0.1
1:1.25:0.75	22.5 ± 0.2	0.726 ± 0.004	0.62 ± 0.01	10.4 ± 0.2
1:0:1.5	22.0 ± 0.3	0.754 ± 0.005	0.56 ± 0.01	9.3 ± 0.1

a: the J_{sc} values are integrated from EQE spectra.

5.3.3 Electronic States in the Ternary OPV

To systematically study the photogeneration mechanism in the ternary blends, we investigated their electronic states. Figure 5.3(a) presents the PL spectra of the ternary PCE-10:BT-CIC:BEIT-4F active region of the NIR sub-cell at different blend ratios. The PCE-10:BT-CIC binary exhibits the 0-0 transition peak of PCE-10 at 1.73 ± 0.01 eV, and for BT-CIC, at 1.39 ± 0.01 eV. The PCE-10:BEIT-4F binary and all ternary mixtures at different blend ratios have a BEIT-4F 0-0 transition at 1.32 ± 0.01 eV. In the ternary mixtures, excitons generated on BT-CIC rapidly transfer to BEIT-4F, which accounts for the absence of BT-CIC exciton peak in the PL spectra. Thus, the excited states in the ternary blends are not influenced by the mixture composition. Figure 5.3(b) shows the EL spectrum of PCE-10:BT-CIC binary blend. The spectrum comprises a BT-CIC exciton peak at 1.37 ± 0.02 eV and a PCE-10:BT-CIC charge transfer (CT) peak at 1.10 ± 0.02 eV. In Fig. 5.3(c) the EL spectrum of PCE-10:BEIT-4F binary blend is fit with a BEIT-4F exciton peak at 1.30 ± 0.02 eV and a PCE-10:BEIT-4F CT peak at 1.15 ± 0.02 eV. The small energy offset between the HOMO of PCE-10 and BEIT-4F gives rise to hole transfer from the PCE-10 to the BEIT-4F HOMO. Hence, there is a prominent BEIT-4F exciton peak in the EL spectrum. Figure

5.3(d) presents the EL spectrum of a PCE-10:BT-CIC:BEIT-4F (1:1.25:0.5, w/w/w) ternary blend, which comprises BEIT-4F, PCE-10:BT-CIC CT and PCE-10:BEIT-4F CT exciton peaks, which are the same as those in the binaries. A similar fitting procedure is applied to this ternary system with different acceptor blend ratios. The spectral features fit well with the electronic states of the binaries. With these results, we infer that the ternary OPV operates as the combination of two, parallel-connected binary heterojunctions,²⁴ which is consistent with the observed ternary device performance parameters that are between those of binaries and change monotonically with blend ratio.

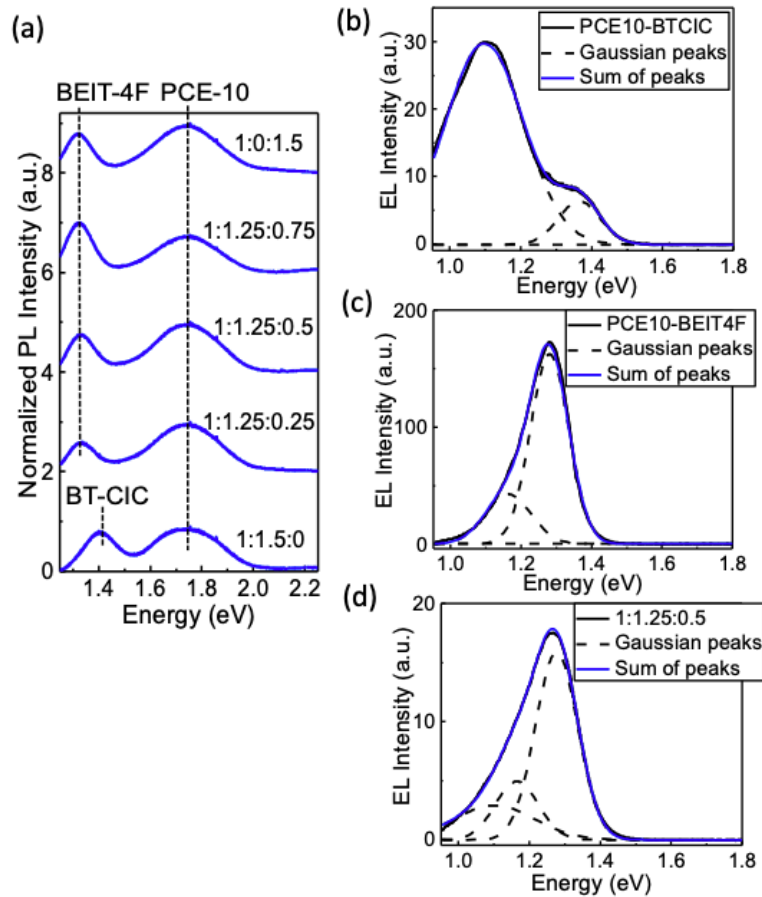


Figure 5.3 Electronic states in PCE-10:BT-CIC:BEIT-4F ternary OPVs.

(a) PL spectra of PCE-10:BT-CIC:BEIT-4F blends at different blend ratios. (b) EL spectrum of 1:1.5 PCE-10:BT-CIC binary cell, with Gaussian peaks fit (dashed lines) and their sum (blue line). (c) EL spectrum of 1:1.5 PCE-10:BEIT-4F with fits as in (b). (d) EL spectrum of 1:1.25:0.5 PCE-10:BT-CIC:BEIT-4F with fits as in (b).

5.4 Tandem Solar Cell

5.4.1 Tandem OPV Structure

To construct an optimized tandem OPV, the optical field was simulated to determine layer thicknesses and positions within the tandem cell required to achieve current balance. The lack of metal anode reflection of the PM6:SFT8-4F front sub-cell (i.e. the sub-cell adjacent to the transparent ITO cathode) requires a thicker active layer to compensate for the reduced absorption, with the optimized structure shown in Fig. 5.4(a). The front sub-cell absorbs primarily between wavelengths of $\lambda = 350$ nm and 750 nm, whereas the back sub-cell which is adjacent to the reflective anode, absorbs primarily at $\lambda > 750$ nm. A nearly optically and electrically lossless CRZ was introduced between the sub-cells consisting of a polymer layer PEDOT:PSS sandwiched between a MoO₃ layer and a ZnO nanoparticle layer. To improve wetting between hydrophobic and hydrophilic surfaces, a thin layer of MoO₃ was thermal evaporated, and then precoated with a thin layer of isopropanol to initiate PEDOT:PSS deposition. As shown in Fig. 5.4(b), this treatment significantly reduces the contact angle of PEDOT:PSS from 98.7° to 21.7°, and thus improves the fabrication yield.

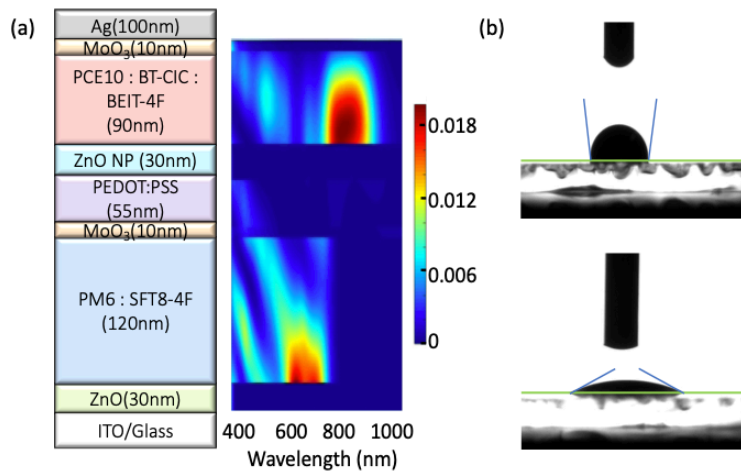


Figure 5.4 Design of tandem OPV.

(a) Tandem device structure with optimized layer thicknesses and corresponding simulated optical field intensity distribution. (b) The contact angle of PEDOT:PSS when deposited before and after surface treatment.

5.4.2 Experimental Methods

Tandem device fabrication

The tandem cells were grown on similarly prepared substrates as the single junction OPVs. The ZnO precursor was spin-coated onto the substrate at 3000 rpm and was baked at 160°C in air for 30 min before the samples were transferred into the ultrapure nitrogen environment. The PM6:SFT8-4F solution was prepared in CB at total concentration 20 mg/mL and stirred overnight at 65°C at 300 rpm. The solution was spin-coated at 2000 rpm for 90s to form a 120 nm thick film on top of ZnO. A 10 nm thick film of MoO₃ was thermally evaporated in vacuum at 0.25 Å/s. The samples were then transferred to the ultrapure nitrogen environment and an IPA layer was spin-coated at 300 rpm for 45s followed by spin-coating filtered PEDOT:PSS (filtered through a Whatman™ 0.45 µm nylon filter w/glass micro fiber) at 5000 rpm. ZnO nanoparticles were synthesized as previously²⁵ and dissolved in 15 mL 1-butanol, with a drop of butylamine added to help the solids disperse. The solution was spin-coated on the PEDOT:PSS at 3000 rpm, followed by spin-coating the back cell active layer at 2000 rpm, and thermally annealed at 120°C for 8 min. The PCE-10:BT-CIC:BEIT-4F solution was prepared in CB with 10% CF at 18 mg/mL and stirred overnight at 65°C at 300 rpm before spin-coating. The samples were transferred into a high vacuum chamber for MoO₃ thermal evaporation at 0.5 Å/s for a 10 nm thick film and a 100 nm film of Ag deposited at 0.6 Å/s. The ARC was grown onto the glass substrate after the devices were complete. The 120 nm MgF₂ film ($n_{\text{MgF}_2}=1.38\pm 0.01$) was thermally evaporated, and the 130 nm SiO₂ film was grown by electron-beam deposition with the substrate at an angle of 85° to the beam direction to achieve a low refractive index $n_{\text{SiO}_2}=1.12\pm 0.03$.^{26,27}

Tandem device characterization

The J - V characteristics were measured similar as the single-junction devices. The EQE of the individual sub-cells in the tandem devices were measured using both optical and electrical bias.²⁸ The continuous illumination from a LED was coupled with chopped monochromated light to provide bias illumination. The front sub-cell EQE was measured with bias illumination provided by a LED emitting at 780 nm (Thorlabs, NJ, USA, Model M780LP1), and under a forward bias voltage of 0.6V to compensate the voltage of the back cell. The back sub-cell EQE was measured with bias illumination provided by a fiber-coupled LED at 455 nm (Thorlabs M455F1) and a forward bias voltage of 0.8V. The electrical bias was measured for the sub-cells under corresponding illumination.

5.4.3 Device Performance

Figures 5.5(a) and (b) presents the J - V characteristics and EQE spectra of the single-junction and tandem devices, with details listed in Table 5.2. The PM6:SFT8-4F (1:1.5, w/w, 80 nm) single junction device reaches $PCE = 12.1 \pm 0.3 \%$ with $J_{SC} = 18.4 \pm 0.3 \text{ mA/cm}^2$, $V_{OC} = 0.98 \pm 0.01 \text{ V}$ and $FF = 0.67 \pm 0.01$. The trade-off between V_{OC} and FF in PCE-10:BT-CIC:BEIT-4F ternary NIR cell results in the highest PCE at a blend ratio 1:1.25:0.5 (w/w/w). Furthermore, the active layer was thermal annealed at 120°C for 8 min to optimize the active layer morphology. The NIR absorbing device with 75 nm active layer thickness has $PCE = 11.7 \pm 0.3\%$ with absorption up to 1050 nm. This is 7% higher than the PCE of a PCE-10:BT-CIC binary device.

The optimized tandem OPV with 120 nm PM6:SFT8-4F front active layer and 90 nm PCE-10:BT-CIC:BEIT-4F back active layer exhibits $J_{SC} = 13.5 \pm 0.2 \text{ mA/cm}^2$, $V_{OC} = 1.66 \pm 0.01 \text{ V}$, $FF = 0.68 \pm 0.01$ and $PCE = 15.2 \pm 0.2\%$ under simulated AM1.5G illumination. To reduce the optical loss, an ARC consisting of a 120 nm MgF_2 layer (index of refraction $n_{\text{MgF}_2} = 1.38 \pm 0.01$) and a 130

nm low-refractive-index SiO_2 layer²⁶ ($n_{\text{SiO}_2}=1.12\pm 0.03$) was deposited on the glass substrate, which reduced the reflection of glass substrate between 400 and 1000 nm for approximately 4%.²⁷ The tandem device with the ARC has an increased J_{SC} and a correspondingly increased PCE. As shown in Fig. 5.5(b), the tandem solar cell absorbs from 350 nm to 1050 nm. The reduced absorption of the front sub-cell is due to the lack of electrode reflection and back sub-cell absorption within the same wavelength region. This provides for current balance between sub-cells, along with a concomitant reduction in J_{SC} compared to that of the single junction PM6:SFT8-4F device. The integration of the EQE spectra gives a balanced front sub-cell $J_{SC} = 14.2 \text{ mA/cm}^2$ and back sub-cell current of $J_{SC} = 14.1 \text{ mA/cm}^2$. The tandem device with an ARC reaches $\text{PCE} = 15.9 \pm 0.2\%$. Detailed performance parameters are listed in Table 5.2.

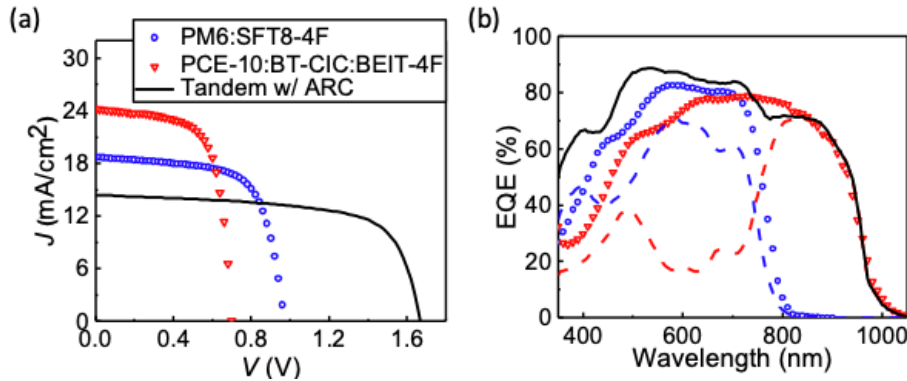


Figure 5.5 Ternary tandem OPV performance.

(a) J - V characteristics of single-junction and tandem devices. (b) EQE of single-junction and tandem cells. The symbols are for discrete single-junction devices, whereas the dashed and solid lines are for sub-cells in the stack and their sum, colors represent the same sub-cells as in (a).

Table 5.2 Discrete sub-cells and tandem devices performances under simulated AM1.5G illumination.

Device	J_{SC}^a (mA/cm ²)	V_{OC} (V)	FF	PCE (%)
PM6:SFT8-4F=1:1.5	18.4 ± 0.3	0.98 ± 0.01	0.67 ± 0.01	12.1 ± 0.3
PCE-10:BT-CIC:BEIT-4F = 1:1.25:0.5, TA	24.3 ± 0.4	0.70 ± 0.01	0.68 ± 0.01	11.7 ± 0.3
Tandem w/o ARC	13.5 ± 0.2	1.66 ± 0.01	0.68 ± 0.01	15.2 ± 0.2
Tandem w/ ARC	14.1 ± 0.2	1.66 ± 0.01	0.68 ± 0.01	15.9 ± 0.2

a: J_{SC} calculated from integrated EQE.

With rapid development in material synthesis, single-junction OPV has reached over 19% efficiency.^{13,14,29,30} Multijunction solar cells can exceed the single-junction thermodynamic limit due to their benefits of lower currents (and hence reduced series resistance losses), which suggests that there is still potential to improve the tandem OPV efficiency.

5.5 Conclusion

To conclude, we demonstrate a high efficiency tandem OPV structure with a NIR-absorbing PCE-10:BT-CIC:BEIT-4F ternary back sub-cell combined with a visible-absorbing binary PM6:SFT8-4F front sub-cell. The NIR-absorbing NFA BEIT-4F extends the absorption of the back sub-cell to 1050 nm and results in current balance with the shorter wavelength absorbing binary front sub-cell. A nearly optically and electrically lossless CRZ comprising a hydrophilic PEDOT:PSS layer sandwiched between MoO₃ and ZnO nanoparticle layers is constructed using an isopropanol surface treatment. The tandem device on an ARC-coated glass substrate reaches a maximum PCE = 15.9 ± 0.2 % under AM1.5G simulated illumination.

Chapter 5

Bibliography

1. Li, Y. *et al.* Enhanced Light Utilization in Semitransparent Organic Photovoltaics Using an Optical Outcoupling Architecture. *Adv. Mater.* **1903173**, 1903173 (2019).
2. Li, Y., Xu, G., Cui, C. & Li, Y. Flexible and Semitransparent Organic Solar Cells. *Adv. Energy Mater.* **8**, 1–28 (2018).
3. Li, Y. *et al.* High Efficiency Near-Infrared and Semitransparent Non-Fullerene Acceptor Organic Photovoltaic Cells. *J. Am. Chem. Soc.* **139**, 17114–17119 (2017).
4. Qu, B. & Forrest, S. R. Continuous roll-to-roll fabrication of organic photovoltaic cells via interconnected high-vacuum and low-pressure organic vapor phase deposition systems. *Appl. Phys. Lett.* **113**, (2018).
5. Che, X., Li, Y., Qu, Y. & Forrest, S. R. High fabrication yield organic tandem photovoltaics combining vacuum- and solution-processed subcells with 15% efficiency. *Nat. Energy* **3**, 422–427 (2018).
6. Che, X., Xiao, X., Zimmerman, J. D., Fan, D. & Forrest, S. R. High-Efficiency, Vacuum-Deposited, Small-Molecule Organic Tandem and Triple-Junction Photovoltaic Cells. *Adv. Energy Mater.* **4**, 1400568 (2014).
7. Gilot, J., Wienk, M. M. & Janssen, R. A. J. Double and triple junction polymer solar cells processed from solution. *Appl. Phys. Lett.* **90**, 88–91 (2007).
8. Li, Y. *et al.* Near-Infrared Ternary Tandem Solar Cells. *Adv. Mater.* **30**, 1804416 (2018).
9. Gilot, J., Wienk, M. M. & Janssen, R. A. J. Optimizing Polymer Tandem Solar Cells. *Adv. Mater.* **22**, E67–E71 (2010).
10. Di Carlo Rasi, D. & Janssen, R. A. J. Advances in Solution-Processed Multijunction

- Organic Solar Cells. *Adv. Mater.* **31**, 1806499 (2019).
11. Li, Y. Molecular design of photovoltaic materials for polymer solar cells: Toward suitable electronic energy levels and broad absorption. *Accounts of Chemical Research* **45**, 723–733 (2012).
 12. Fan, Q. *et al.* Overcoming the energy loss in asymmetrical non-fullerene acceptor-based polymer solar cells by halogenation of polymer donors. *J. Mater. Chem. A* **7**, 15404–15410 (2019).
 13. Yuan, J. *et al.* Single-Junction Organic Solar Cell with over 15% Efficiency Using Fused-Ring Acceptor with Electron-Deficient Core. *Joule* **3**, 1140–1151 (2019).
 14. Pan, M. A. *et al.* 16.7%-efficiency ternary blended organic photovoltaic cells with PCBM as the acceptor additive to increase the open-circuit voltage and phase purity. *J. Mater. Chem. A* **7**, 20713–20722 (2019).
 15. Meng, L. *et al.* Organic and solution-processed tandem solar cells with 17.3% efficiency. *Science* **361**, 1094–1098 (2018).
 16. Yao, Z. *et al.* Dithienopicenocarbazole as the kernel module of low-energy-gap organic dyes for efficient conversion of sunlight to electricity. *Energy Environ. Sci.* **8**, 3192–3197 (2015).
 17. Xiao, Z. *et al.* 26 mA cm⁻² Jsc from organic solar cells with a low-bandgap nonfullerene acceptor. *Sci. Bull.* **62**, 1494–1496 (2017).
 18. Xiao, Z., Jia, X. & Ding, L. Ternary organic solar cells offer 14% power conversion efficiency. *Sci. Bull.* **62**, 1562–1564 (2017).
 19. Liu, F. *et al.* Efficient Semitransparent Solar Cells with High NIR Responsiveness Enabled by a Small-Bandgap Electron Acceptor. *Adv. Mater.* **29**, 1606574 (2017).

20. Yeh, P. N., Liao, S. H., Li, Y. L., Syue, H. R. & Chen, S. A. Large active area inverted tandem polymer solar cell with high performance via alcohol treatment on the surface of bottom active layer P3HT:ICBA. *Sol. Energy Mater. Sol. Cells* **128**, 240–247 (2014).
21. Li, X. *et al.* Enhanced Photocurrent Density by Spin-Coated NiO Photocathodes for N-Annulated Perylene-Based p-Type Dye-Sensitized Solar Cells. *ACS Appl. Mater. Interfaces* **8**, 19393–19401 (2016).
22. Jiang, W., Li, Y. & Wang, Z. Heteroarenes as high performance organic semiconductors. *Chem. Soc. Rev.* **42**, 6113–6127 (2013).
23. Yao, Z. *et al.* Dithienopicenocarbazole-Based Acceptors for Efficient Organic Solar Cells with Optoelectronic Response over 1000 nm and an Extremely Low Energy Loss. *J. Am. Chem. Soc.* **140**, 2054–2057 (2018).
24. Huang, X., Liu, X., Ding, K. & Forrest, S. R. Is there such a thing as a molecular organic alloy? *Mater. Horizons* (2019). doi:10.1039/c9mh01351b
25. Beek, W. J. E., Wienk, M. M., Kemerink, M., Yang, X. & Janssen, R. A. J. Hybrid zinc oxide conjugated polymer bulk heterojunction solar cells. *J. Phys. Chem. B* **109**, 9505–9516 (2005).
26. Xi, J.-Q. *et al.* Very low-refractive-index optical thin films consisting of an array of SiO₂ nanorods. *Opt. Lett.* **31**, 601 (2006).
27. Slootsky, M. & Forrest, S. R. Enhancing waveguided light extraction in organic LEDs using an ultra-low-index grid. *Opt. Lett.* **35**, 1052 (2010).
28. Gilot, J., Wienk, M. M. & Janssen, R. A. J. Measuring the external quantum efficiency of two-terminal polymer tandem solar cells. *Adv. Funct. Mater.* **20**, 3904–3911 (2010).
29. Cui, Y. *et al.* Single-Junction Organic Photovoltaic Cell with 19% Efficiency. *Adv. Mater.*

33, 2102420 (2021).

30. Zhan, L. *et al.* Manipulating Charge Transfer and Transport via Intermediary Electron Acceptor Channels Enables 19.3% Efficiency Organic Photovoltaics. *Adv. Energy Mater.* **12**, 2201076 (2022).

Chapter 6

Semitransparent Organic Photovoltaic Module with Minimal Resistance Loss

Recent developments in semitransparent organic photovoltaics (ST-OPVs) with potential applications to building integrated power generating windows have shown substantial increase in PCE and average photopic transmission (APT) at the laboratory scale. However, less attention has been paid to the area scaling of ST-OPV cells. In this chapter, we investigate the scalability of ST-OPV cells from 4 mm² to 1 cm², as well as 9 cm² active area prototype module. By integrating both top and bottom metal grids onto the transparent electrodes, the series resistance loss of 1 cm² ST-OPV cell is significantly reduced and is comparable to that of the grid-free 4 mm² cell. Nine 1 cm² cells are then connected in a series-parallel circuit to realize a prototype ST-OPV module. A 100% fabrication yield with only 5% PCE deviation among discrete cells is achieved. The semitransparent module shows PCE = 7.2 ± 0.1% under simulated AM1.5G illumination at 1 sun intensity, which exhibits no connection resistance loss compared to that of the individual cells. The ST-OPV module exhibits an APT = 38.1 ± 1.1%, which enables a light utilization efficiency, LUE = 2.74 ± 0.09%. The method demonstrates a promising way for ST-OPV modules to scale without compromising performance.

6.1 Introduction

Building integrated photovoltaics (BIPV) that employ transparent solar cells on window panes provide a space-efficient and attractive solution to solar energy harvesting.¹⁻⁵ Unlike conventional inorganic semiconductors, organic semiconductors have relatively narrow excitonic absorption spectra that allow for OPV featuring transparency across visible spectrum, while selectively absorbing in the NIR.⁶⁻⁸ In this regard, OPVs are an attractive BIPV technology that can simultaneously achieve a high PCE along with a high average photopic transmission (APT). Over the past few years, OPVs have been demonstrated with impressive PCE and exceptional intrinsic stability.⁹⁻¹³ Furthermore, with the development of NIR-absorbing materials and optical structures, ST-OPVs have realized remarkable improvements in light utilization efficiency (LUE = PCE x APT) up to 5.0%.¹⁴⁻²² Starting from this promising performance, an estimated cost of 0.47 - 1.6 \$/W_p has been reported,²³ which motivates practical and widespread deployment of ST-OPVs in BIPV applications.

It remains questionable, however, whether these highly efficient laboratory-scale, small-area ST-OPVs can maintain their performance when translated to larger modules. To date, research on OPV modules has primarily focused on multi-junction strategies and improved material design in opaque devices,^{24,25} while less attention has been paid to the scalability of ST-OPVs.²⁶⁻³⁴ Compared to opaque OPVs with one thick, highly conductive metal electrode, ST-OPVs require both electrodes to be transparent, which doubles the overall series resistance loss, and significantly limits their scalability. Moreover, the narrow energy gaps of NIR-absorbing materials required in ST-OPVs result in a low V_{OC} , which worsens series resistance losses by reducing the FF and, ultimately, the PCE.^{24,35}

Here, we demonstrate a scalable ST-OPV prototype module with a negligible compromise of efficiency from series resistance losses. The ST-OPVs employ BHJ based on a low energy gap polymer donor, PCE-10, combined with a NIR absorbing acceptor, BT-CIC.⁸ As the active area of the cells scale from 4 mm² to 1 cm², the sheet resistance of the ITO cathode and the thin, semitransparent Ag anode dominates the specific series resistance (R_{SA}), which reduces the FF and PCE. By employing finely patterned metal grids on the two transparent electrodes,³⁶⁻⁴⁰ the series resistance loss of 1 cm² device is significantly reduced, leading to an improved PCE close to that of a 4 mm² device. Based on these findings, nine 1 cm² ST-OPV devices are integrated into a prototype module and connected in a series-parallel circuit configuration²⁴ with a geometric fill factor (GFF) of 65%. A 100% fabrication yield with cell-to-cell PCE variation of < 5% is achieved. The module performance shows no loss from connection resistance compared to the discrete cells. Combined with an optimized visible light outcoupling (OC) structure, the ST-OPV module exhibits LUE = $2.74 \pm 0.09\%$ with APT = $38.1 \pm 1.1\%$ and PCE = $7.2 \pm 0.1\%$ under simulated AM1.5G illumination at 1 sun intensity. With the combination of NIR absorbing BHJ, OC structure and minimized resistance loss in module construction, this is a significant improvement over previous reported ST-OPV module performance.²⁵⁻³⁴

6.2 Impact of Series Resistance on 1 cm² OPV

6.2.1 Experimental Methods

Figure 6.1 shows a schematic illustration of the 1 cm² ST-OPV structure, which employs a 80 nm PCE-10:BT-CIC (1:1.5 w/w) BHJ, with 30 nm thick ZnO and 20 nm thick MoO₃ as electron and hole transporting layers, respectively. The Au surrounding and grids on bottom electrode as well as the Ag grids on top electrodes are employed to reduce series resistance loss.

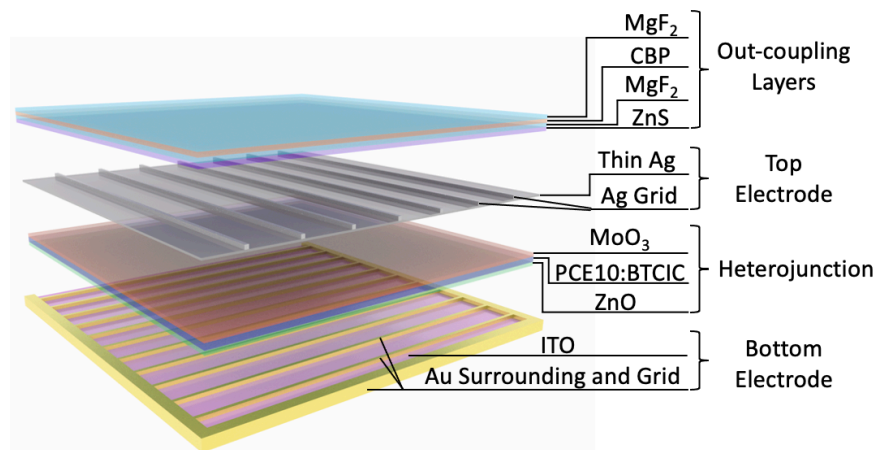


Figure 6.1 Schematic of 1 cm² ST-OPV device structure.

Schematic of the 1 cm² ST-OPV device structure composed of electrodes with integrated grids, heterojunction and optical outcoupling (OC) layers.

Au grids/ITO cathode fabrication

Glass substrates were cleaned with detergent and solvents before deposition. A 150 nm thick ITO layer was sputter-deposited at 1.72 Å/s in a high vacuum chamber (base pressure $\sim 10^{-7}$ Torr) and thermally annealed at 400°C for 5 min in forming gas (5% H₂ + 95% N₂). The ITO was photolithographically patterned and wet etched using HCl:H₂O (3:1) to define the square shaped cathode. The Au surrounding bars (0.5 mm wide, 200 nm thick on a pre-deposited 10 nm thick Ti adhesion layer) are photolithographically patterned along three edges of the ITO cathode, and Au grids (20 μm wide, 400 μm separation, 45 nm thick with a 5 nm thick Ti adhesion layer) are patterned across the entire cathode. All Au and Ti layers were deposited via electron-beam evaporation at 5 Å/s.

Ultrathin Kapton shadow mask preparation

As described in Fig. 6.2, a 25 μm thick E-type Kapton foil is coated with 10 nm thick Ti/500 nm Al using electron-beam evaporation. A 100 μm thick PDMS (Sylgard 184, base-to-curing agent weight ratio = 10:1) membrane is spun at 800 rpm on a 10 cm diameter Si handle and cured at 100°C for 3 h. The Kapton foil with Al layer facing up is then attached to the PDMS

membrane to eliminate curling. The top grid pattern (20 μm wide, 600 μm separation) is photolithographically defined on the foil. The foil is etched using Cl_2 plasma ($\text{H}_2:\text{Cl}_2:\text{Ar} = 12:9:5$ sccm, 10 mTorr chamber pressure, 500 W inductively coupled plasma (ICP) power, 100 W forward power for 1 min) to remove the Ti and Al layers and expose the Kapton. The 25 μm Kapton foil is then etched through using O_2 plasma ($\text{O}_2 = 20$ sccm, 6 mTorr chamber pressure, 500 W ICP power, 100 W forward power for 40 min). Finally, the Kapton foil is detached from the PDMS membrane and soaked in buffered HF for 6 min to remove the remaining Al and Ti.

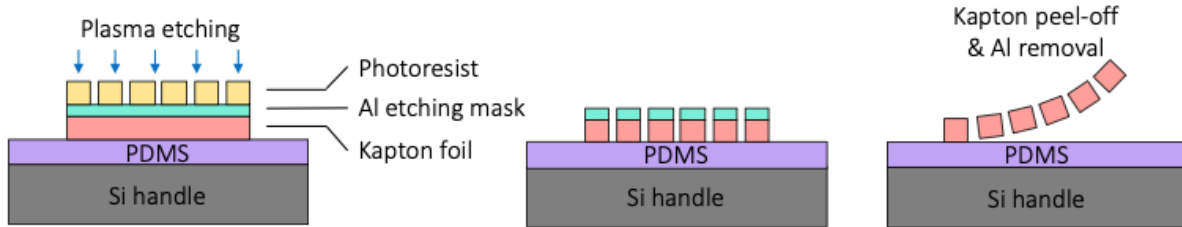


Figure 6.2 Fabrication flow of Kapton shadow mask.

Schematics of the fabrication flow of ultrathin Kapton shadow mask for fine metal grid deposition on top electrode.

Device fabrication

Glass substrates with a patterned cathode (ITO or Au/ITO) were cleaned using detergent and solvents followed by UV ozone exposure for 15 min before growth. The ZnO precursor solution was spin-coated onto the substrate at 3000 rpm and baked at 160°C in air for 30 min. The PCE-10:BT-CIC solution was prepared in chlorobenzene with 10% chloroform at a concentration of 16 mg/mL and stirred overnight at 65°C, 350 rpm. After filtering through a 0.45 μm polytetrafluoroethylene filter, the solution was spin-coated at 2000 rpm on top of ZnO layer in ultrapure N_2 ($\text{O}_2 < 0.1$ ppm, $\text{H}_2\text{O} < 0.1$ ppm). Then the samples were transferred into a high vacuum chamber (base pressure $\sim 10^{-7}$ Torr) for thermal evaporation of 20 nm thick MoO_3 at 0.2 $\text{\AA}/\text{s}$. For 1 cm^2 devices, the MoO_3 layer was deposited through a shadow mask. For the module fabrication, after MoO_3 deposition, the ZnO, BHJ and MoO_3 layers were mechanically scribed into nine units

based on the cathode pattern to separate devices and expose one edge of each cathode for series connection. Then 16 nm thick Ag was thermally evaporated at 0.1 Å/s (100 nm Ag at 0.1-0.6 Å/s, for opaque devices) through a shadow mask followed by 100 nm Ag grid deposition at 0.1-0.6 Å/s through the Kapton shadow mask to construct the anode. The anode has a 1 cm² overlap with the cathode pattern to define the unit device area. The outcoupling structure was thermally evaporated in a high vacuum chamber (base pressure ~10⁻⁷ Torr) at 0.5 Å/s for each layer.

Device characterization

The J - V characteristics and EQE of 4 mm² and 1 cm² devices were measured in a glovebox filled with ultrapure nitrogen similar to previous chapters. The EQE measurements were performed with focused beam that underfills the device area, for the devices with grids the beam can underfill the device area between grids. The transmission spectra were measured using UV-vis spectrometer (Perkin-Elmer 1050). The reflection spectra were measured using an F20 Filmetric thin film measurement instrument integrated with a spectrometer and a light source from 395 nm to 1032 nm.

The average photopic transmission (APT) is calculated using the formula:^{14,15,41}

$$\text{APT} = \frac{\int T(\lambda)P(\lambda)S(\lambda)d\lambda}{\int P(\lambda)S(\lambda)d\lambda}, \quad (6.1)$$

where λ is wavelength, $T(\lambda)$ is the transmission, $P(\lambda)$ is the photopic spectral response of human eyes, and $S(\lambda)$ is the AM1.5G solar irradiance, which is the incident light spectrum of a solar cell. APT has also been referred to as average visible transmission (AVT).^{5,17,18,42-46} However, AVT is also understood as the average transmittance in the visible region.^{18,27,47,48} Hence, APT as defined above eliminates that ambiguity.

6.2.2 1-cm² OPV Performance

To investigate the resistance loss from the bottom ITO cathode with area scaling, we first fabricated opaque OPV devices with 100 nm thick top Ag anode. The J - V characteristics are shown in Fig. 6.3(a), with detailed performance parameters listed in Table 6.1. The 4 mm² opaque device (red line with squares) has $R_{SA} = 1.5 \pm 0.1 \Omega \cdot \text{cm}^2$, however, the R_{SA} increases to $15.4 \pm 0.5 \Omega \cdot \text{cm}^2$ as the active area increases to 1 cm² (blue line with circles) due to the 15 Ω/sq large sheet resistance of ITO, which results in a significant decrease in FF from 0.69 ± 0.01 to 0.39 ± 0.03 . To reduce the R_{SA} from ITO, we integrate a 500 nm thick Au surrounding and 50 nm thick Au grids onto the ITO cathode, as shown for the bottom electrode in Fig. 6.1. The nearly invisible grids are patterned into 20 μm wide stripes with 400 μm separation via photolithography. The grids reduce R_{SA} of the 1 cm² opaque device (yellow line with triangles) to $3.1 \pm 0.4 \Omega \cdot \text{cm}^2$, leading to $FF = 0.65 \pm 0.01$. Although the J_{SC} is decreased from $23.1 \pm 0.7 \text{ mA}/\text{cm}^2$ to $22.0 \pm 0.4 \text{ mA}/\text{cm}^2$ because the Au grids partially block the light incident on the photoactive region, a significant increase in PCE from $5.9 \pm 0.3\%$ to $10.0 \pm 0.2\%$ is realized.

The 1 cm² ST-OPV devices with a 16 nm thick, semitransparent Ag anode was fabricated, with J - V characteristics shown in Fig. 6.3(b) and parameters listed in Table 6.1. Compared to 4 mm² devices (red line with squares) with $R_{SA} = 1.8 \pm 0.1 \Omega \cdot \text{cm}^2$, the 1 cm² ST-OPV with integrated bottom electrode (blue line with circles) shows $R_{SA} = 9.5 \pm 0.3 \Omega \cdot \text{cm}^2$, indicating that the resistance is mainly due to the ultrathin Ag anode which has sheet resistance of 6 Ω/sq . As illustrated in Fig. 6.1, we deposited a layer of 100 nm thick Ag top grids with 20 μm grid width and 600 μm separation patterned using a 25 μm thick Kapton shadow mask. Compared to conventional metal shadow mask, the thin Kapton mask allows for ultrafine resolution patterning. The reflection from the 100 nm Ag grids provides a slight increase in the J_{SC} of 1 cm² ST-OPV

from $16.2 \pm 0.3 \text{ mA/cm}^2$ to $16.5 \pm 0.1 \text{ mA/cm}^2$. The R_{SA} of the 1 cm^2 ST-OPV (yellow line with triangles) is reduced to $4.3 \pm 0.2 \Omega \cdot \text{cm}^2$, which leads to an increase in FF from 0.57 ± 0.01 to 0.65 ± 0.01 , and the PCE from $6.3 \pm 0.2\%$ to $7.3 \pm 0.1\%$.

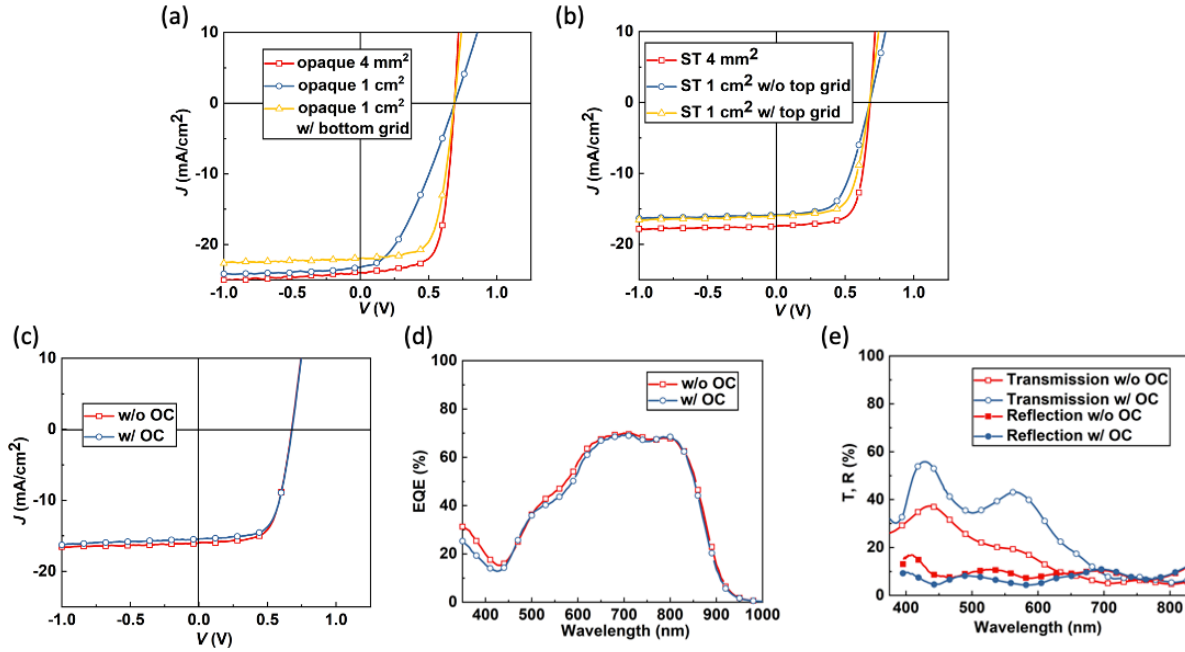


Figure 6.3 Performance of 4 mm^2 and 1 cm^2 OPV devices.

(a) J - V characteristics of 4 mm^2 (red, square), 1 cm^2 (blue, circle), and 1 cm^2 cathode with grids (yellow, triangle) OPV devices. (b) J - V characteristics of 4 mm^2 (red, square), 1 cm^2 (blue, circle) and 1 cm^2 anode with grids (yellow, triangle) ST-OPV devices. (c) J - V characteristics and (d) EQE spectra of 1 cm^2 ST-OPV cells with (blue, circle) and without (red, square) the OC structure. (e) Transmission and reflection spectra of the ST-OPV stack with (blue, circle) and without (red, square) the OC structure.

The 1 cm^2 ST-OPV shown in Fig. 6.1 combines the bottom and top grid electrodes with the 4-layer OC structure comprising ZnS (30 nm)/MgF₂ (100 nm)/CBP (90 nm)/MgF₂ (10 nm) at the top surface to improve visible transmission. The integration of grids on both electrodes occupies 7% of the device active area and blocks the view directly behind the grids. Figures 6.3(c) and (d) show the J - V characteristics and EQE spectra of the 1 cm^2 ST-OPV with and without the OC structure, and the detailed parameters are provided in Table 6.1. The transmission and reflection spectra of the ST-OPV stack with and without the OC layers are plotted in Fig. 6.3(e). The OC

structure significantly increases the transmission of ST-OPV in the visible, which results in an improved APT from $20.0 \pm 1.0\%$ to $38.1 \pm 1.1\%$, while $\text{PCE} = 7.3 \pm 0.1\%$ is maintained.

Table 6.1 Performance of 4 mm² and 1 cm² OPV devices under simulated AM1.5G illumination.

Device	J_{sc} (mA/cm ²)	V_{oc} (V)	FF	PCE (%)	R_{sA} ($\Omega \cdot \text{cm}^2$)	APT (%)
Opaque						
4 mm ²	23.5 ± 0.8	0.69 ± 0.01	0.69 ± 0.01	11.2 ± 0.4	1.5 ± 0.1	-
1 cm ²	23.1 ± 0.7	0.69 ± 0.01	0.39 ± 0.03	5.9 ± 0.3	15.4 ± 0.5	-
1 cm ² w/ bottom grid	22.0 ± 0.4	0.69 ± 0.01	0.65 ± 0.01	10.0 ± 0.2	3.1 ± 0.4	-
Semitransparent (ST)						
4 mm ²	17.5 ± 0.6	0.68 ± 0.01	0.69 ± 0.01	8.2 ± 0.3	1.8 ± 0.1	
1 cm ² w/ bottom grid	16.2 ± 0.3	0.68 ± 0.01	0.57 ± 0.01	6.3 ± 0.2	9.5 ± 0.3	
1 cm ² w/ both grids	16.5 ± 0.1	0.68 ± 0.01	0.65 ± 0.01	7.3 ± 0.1	4.3 ± 0.2	20.0 ± 1.0
1 cm ² w/ both grids and OC	16.3 ± 0.2	0.68 ± 0.01	0.66 ± 0.01	7.3 ± 0.1	-	38.1 ± 1.1

6.3 Prototype ST-OPV Module

6.3.1 Module Design

We then fabricated a small prototype module comprising nine, 1 cm² ST-OPVs cells with both grids and OC structures. As shown in Fig. 6.4, three discrete cells are series connected with a 0.3 cm interconnection distance to form a column, while three columns are separated by 0.25 cm, and are connected in parallel with the contact electrodes to construct the module. This design has a GFF = 65%, which is limited by the width of bottom electrode Au surrounding bar, and the use of mechanical scribing to pattern the heterojunction layers. By increasing the Au side bar thickness, the width can be narrowed without affecting performance. Mechanical scribing can also be replaced with higher resolution laser scribing to further improve the GFF.⁴⁹

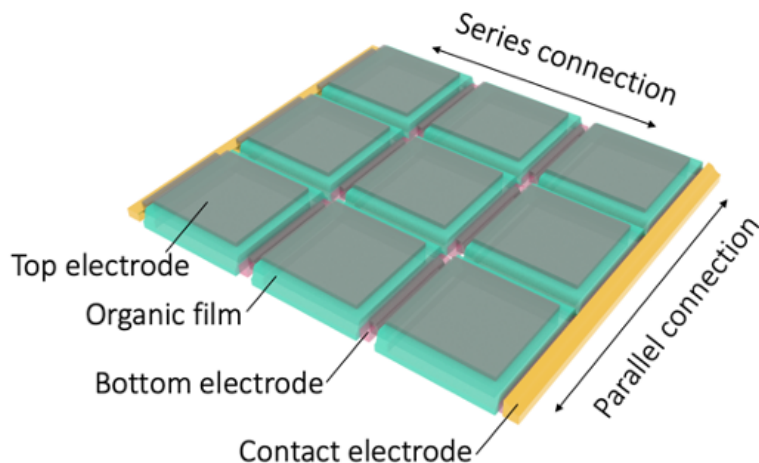


Figure 6.4 Schematic of the design of prototype ST-OPV module.

Illustration of the series-parallel connected prototype ST-OPV module comprising nine sub-cells.

6.3.2 Module Performance

The current-voltage (I - V) characteristics of 9 cm² active area module were measured in air using a solar simulator with a 1000 W Xe lamp with an AM1.5G filter (Oriel Instruments, Model 91191) whose 1 sun intensity was calibrated by a Si reference cell.

The fabrication yield of discrete cells is 100%. Under 1 sun illumination, the nine individual cells exhibit short-circuit currents of $I_{SC} = 16.8 \pm 0.1$ mA, $V_{OC} = 0.67 \pm 0.01$ V, $FF = 0.63 \pm 0.01$. All the parameters have cell-to-cell variations of $< 5\%$. The PCE of the discrete cells ranges within $7.2 \pm 0.2\%$, as shown in Fig. 6.5(a). Figure 6.5(b) shows the I - V characteristics of a discrete cell and the module, with detailed parameters shown in Table 6.2. We obtain a module output power of 65 ± 3 mW under simulated AM 1.5G at 1 sun intensity, with $I_{SC} = 51.1 \pm 1.0$ mA, $V_{OC} = 2.00 \pm 0.01$ V and $FF = 0.63 \pm 0.01$, corresponding to $PCE = 7.2 \pm 0.1\%$ in reference to the active area of the prototype module. The module V_{OC} is 0.5% less than the sum of the V_{OC} of three individual cells, while I_{SC} is within 1.5% deviation from the sum of three individual cells. Also, FF is the same as for the discrete cells, indicating that the resistance losses from electrodes and

interconnections are minimal due to the metal grids and circuit layout. Combined with the optimized transmission $APT = 38.1 \pm 1.1 \%$, we obtain a module $LUE = 2.74 \pm 0.09 \%$. A photograph of the ST-OPV module is shown in the inset of Fig. 6.5(b).

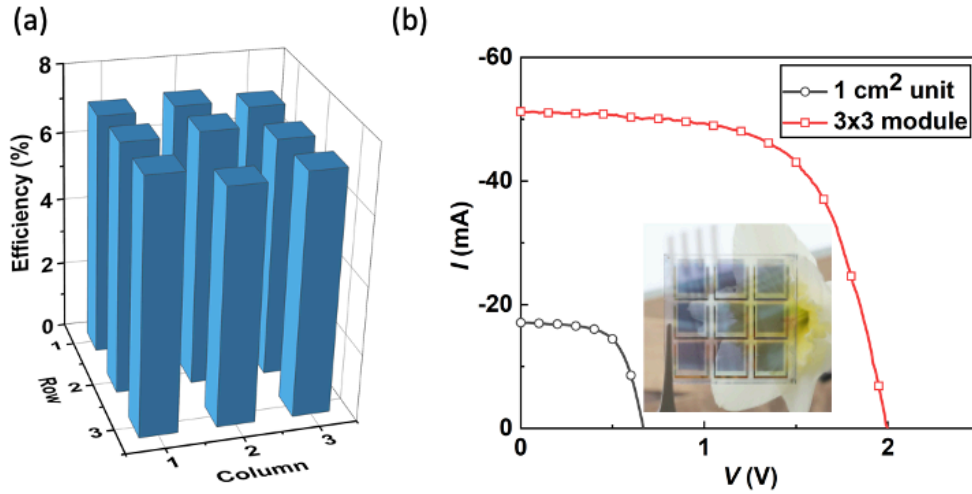


Figure 6.5 Performance of 9 cm² prototype ST-OPV module.

(a) Power conversion efficiencies of the discrete unit cells across the module. (b) I - V characteristics of a discrete cell (black, circle) and the module (red, square) under simulated 1 sun illumination. Inset: Photograph of the prototype ST-OPV module.

Table 6.2 Performance of 9 cm² ST-OPV module under simulated AM1.5G illumination.

Device	I_{sc} (mA)	V_{oc} (V)	FF	PCE (%)	APT (%)
1 cm ² discrete cell	16.8 ± 0.3	0.67 ± 0.01	0.63 ± 0.01	7.2 ± 0.2	38.1 ± 1.1
module	51.1 ± 1.0	2.00 ± 0.01	0.63 ± 0.01	7.2 ± 0.1	38.1 ± 1.1

Note that here we only demonstrate a prototype module as a means to study the effect of scaling on resistance. Our results indicate that if high resolution electrode patterning is used, the GFF can approach unity, in which case the reported $PCE = 7.2 \pm 0.1\%$ would also be achieved in a practical module. Furthermore, note that the ST-OPV module overcomes the efficiency loss from connection resistance as more cells are connected even in opaque OPV modules.^{49,50} Our result

suggests that with the foregoing fabrication process, ST-OPV modules with increased number of columns and rows can have an increased V_{OC} and I_{SC} without degradation of either FF or PCE.

6.4 Conclusion

We investigated the effect of series resistance loss on the scalability of ST-OPV devices. Compared to 4 mm^2 devices, the dominant contribution from ITO cathode and ultrathin Ag anode sheet resistance results in a significantly increased resistive loss in 1 cm^2 ST-OPV cells. By integrating Au grids onto the cathode and Ag grids onto the anode, the R_{SA} is reduced such that the PCE loss is negligible. Furthermore, with the application of a series-parallel circuit layout, we demonstrated a 9 cm^2 active area, prototype ST-OPV module with 100% discrete cell yield and a PCE variation within 5% across the module. The ST-OPV module exhibits $\text{PCE} = 7.2 \pm 0.1\%$, which has no loss compared to discrete cells performance, $\text{APT} = 38.1 \pm 1.1\%$, and $\text{LUE} = 2.74 \pm 0.09\%$. This demonstration provides a promising path for ST-OPV modules to achieve unlimited scalability with uncompromised module performance.

Chapter 6

Bibliography

1. Pagliaro, M., Ciriminna, R. & Palmisano, G. BIPV: Merging the photovoltaic with the construction industry. *Prog. Photovoltaics Res. Appl.* **18**, 61–72 (2010).
2. Yang, R. J. & Zou, P. X. W. Building integrated photovoltaics (BIPV): Costs, benefits, risks, barriers and improvement strategy. *Int. J. Constr. Manag.* **16**, 39–53 (2016).
3. Ferrara, C., Wilson, H. R. & Sprenger, W. Building-integrated photovoltaics (BIPV). in *The Performance of Photovoltaic (PV) Systems: Modelling, Measurement and Assessment* 235–250 (Elsevier Inc., 2017). doi:10.1016/B978-1-78242-336-2.00008-2
4. Heinstein, P., Ballif, C. & Perret-Aebi, L. E. Building integrated photovoltaics (BIPV): Review, potentials, barriers and myths. *Green* **3**, 125–156 (2013).
5. Traverse, C. J., Pandey, R., Barr, M. C. & Lunt, R. R. Emergence of highly transparent photovoltaics for distributed applications. *Nat. Energy* **2**, 849–860 (2017).
6. Lunt, R. R. & Bulovic, V. Transparent, near-infrared organic photovoltaic solar cells for window and energy-scavenging applications. *Appl. Phys. Lett.* **98**, 113305 (2011).
7. Meiss, J., Holzmueller, F., Gresser, R., Leo, K. & Riede, M. Near-infrared absorbing semitransparent organic solar cells. *Appl. Phys. Lett.* **99**, 10–13 (2011).
8. Li, Y. *et al.* High Efficiency Near-Infrared and Semitransparent Non-Fullerene Acceptor Organic Photovoltaic Cells. *J. Am. Chem. Soc.* **139**, 17114–17119 (2017).
9. Che, X., Li, Y., Qu, Y. & Forrest, S. R. High fabrication yield organic tandem photovoltaics combining vacuum- and solution-processed subcells with 15% efficiency. *Nat. Energy* **3**, 422–427 (2018).
10. Meng, L. *et al.* Organic and solution-processed tandem solar cells with 17.3% efficiency.

- Science* **361**, 1094–1098 (2018).
11. Liu, Q. *et al.* 18% Efficiency organic solar cells. *Sci. Bull.* **65**, 272–275 (2020).
 12. Cui, Y. *et al.* Single-Junction Organic Photovoltaic Cells with Approaching 18% Efficiency. *Adv. Mater.* **32**, (2020).
 13. Burlingame, Q. *et al.* Intrinsically stable organic solar cells under high-intensity illumination. *Nature* **573**, 394–397 (2019).
 14. Li, Y. *et al.* Enhanced Light Utilization in Semitransparent Organic Photovoltaics Using an Optical Outcoupling Architecture. *Adv. Mater.* **31**, 1903173 (2019).
 15. Li, Y. *et al.* Color-neutral, semitransparent organic photovoltaics for power window applications. *Proc. Natl. Acad. Sci. U. S. A.* **117**, 21147–21154 (2020).
 16. Bai, Y. *et al.* Interfacial engineering and optical coupling for multicolored semitransparent inverted organic photovoltaics with a record efficiency of over 12%. *J. Mater. Chem. A* **7**, 15887–15894 (2019).
 17. Liu, Q. *et al.* Light Harvesting at Oblique Incidence Decoupled from Transmission in Organic Solar Cells Exhibiting 9.8% Efficiency and 50% Visible Light Transparency. *Adv. Energy Mater.* **10**, 1904196 (2020).
 18. Zuo, L., Shi, X., Fu, W. & Jen, A. K. Y. Highly Efficient Semitransparent Solar Cells with Selective Absorption and Tandem Architecture. *Adv. Mater.* **31**, 1901683 (2019).
 19. Dai, S. & Zhan, X. Nonfullerene Acceptors for Semitransparent Organic Solar Cells. *Adv. Energy Mater.* **8**, 1800002 (2018).
 20. Brus, V. V. *et al.* Solution-Processed Semitransparent Organic Photovoltaics: From Molecular Design to Device Performance. *Adv. Mater.* **31**, 1900904 (2019).
 21. Chen, S. *et al.* A Nonfullerene Semitransparent Tandem Organic Solar Cell with 10.5%

- Power Conversion Efficiency. *Adv. Energy Mater.* **8**, 1–6 (2018).
22. Wang, D. *et al.* High-Performance Semitransparent Organic Solar Cells with Excellent Infrared Reflection and See-Through Functions. *Adv. Mater.* **32**, 2001621 (2020).
 23. Lee, B., Lahann, L., Li, Y. & Forrest, S. R. Cost estimates of production scale semitransparent organic photovoltaic modules for building integrated photovoltaics. *Sustain. Energy Fuels* **4**, 5765–5772 (2020).
 24. Xiao, X., Lee, K. & Forrest, S. R. Scalability of multi-junction organic solar cells for large area organic solar modules. *Appl. Phys. Lett.* **106**, (2015).
 25. Dong, S., Jia, T., Zhang, K., Jing, J. & Huang, F. Single-Component Non-halogen Solvent-Processed High-Performance Organic Solar Cell Module with Efficiency over 14%. *Joule* **4**, 2004–2016 (2020).
 26. Lim, D. C. *et al.* Semi-transparent plastic solar cell based on oxide-metal-oxide multilayer electrodes. *Prog. Photovoltaics Res. Appl.* **26**, 188–195 (2018).
 27. Pascual-San-José, E. *et al.* Towards photovoltaic windows: Scalable fabrication of semitransparent modules based on non-fullerene acceptors via laser-patterning. *J. Mater. Chem. A* **8**, 9882–9895 (2020).
 28. Berny, S. *et al.* Solar Trees: First Large-Scale Demonstration of Fully Solution Coated, Semitransparent, Flexible Organic Photovoltaic Modules. *Adv. Sci.* **3**, 1500342 (2016).
 29. Guo, F. *et al.* Semitransparent organic photovoltaic modules with Ag nanowire top electrodes. in *Organic Photovoltaics XV* (eds. Kafafi, Z. H., Lane, P. A. & Samuel, I. D. W.) **9184**, 91841D (SPIE, 2014).
 30. Guo, F. *et al.* Nanowire Interconnects for Printed Large-Area Semitransparent Organic Photovoltaic Modules. *Adv. Energy Mater.* **5**, 1401779 (2015).

31. Strohm, S. *et al.* P3HT: Non-fullerene acceptor based large area, semi-transparent PV modules with power conversion efficiencies of 5%, processed by industrially scalable methods. *Energy Environ. Sci.* **11**, 2225–2234 (2018).
32. Lucera, L. *et al.* Printed semi-transparent large area organic photovoltaic modules with power conversion efficiencies of close to 5 %. *Org. Electron.* **45**, 209–214 (2017).
33. Jeong, J. H. *et al.* Multi-dimensional interfacial engineering for a practical large-area transparent flexible organic photovoltaics. *Chem. Eng. J.* **419**, 129672 (2021).
34. Lewis, J. E., Lafalce, E., Toglia, P. & Jiang, X. Over 30% transparency large area inverted organic solar array by spray. *Sol. Energy Mater. Sol. Cells* **95**, 2816–2822 (2011).
35. Bube, R. H. & Fahrenbruch, A. L. Photovoltaic Effect. *Adv. Electron. Electron Phys.* **56**, 163–217 (1981).
36. Hauser, J. R. & Dunbar, P. M. Performance Limitations of Silicon Solar Cells. *IEEE Trans. Electron Devices* **ED-24**, 305–321 (1977).
37. Wang, Y. *et al.* Top and bottom electrode optimization enabled high-performance flexible and semi-transparent organic solar cells. *Mater. Chem. Front.* **3**, (2021).
38. Rowell, M. W. & McGehee, M. D. Transparent electrode requirements for thin film solar cell modules. *Energy Environ. Sci.* **4**, 131–134 (2011).
39. Patil, B. R. *et al.* ITO with embedded silver grids as transparent conductive electrodes for large area organic solar cells. *Nanotechnology* **28**, 405303 (2017).
40. Davy, N. C. *et al.* Pairing of near-ultraviolet solar cells with electrochromic windows for smart management of the solar spectrum. *Nat. Energy* **2**, 1–11 (2017).
41. Forrest, S. R. Organic light detectors. in *Organic Electronics* (2020).
doi:10.1093/oso/9780198529729.003.0007

42. Almora, O. *et al.* Device Performance of Emerging Photovoltaic Materials (Version 1). *Adv. Energy Mater.* **11**, 2002774 (2021).
43. Li, Z., Ma, T., Yang, H., Lu, L. & Wang, R. Transparent and Colored Solar Photovoltaics for Building Integration. *Sol. RRL* **5**, 2000614 (2021).
44. Lee, K. *et al.* Neutral-Colored Transparent Crystalline Silicon Photovoltaics. *Joule* **4**, 235–246 (2020).
45. Yang, C., Liu, D., Bates, M., Barr, M. C. & Lunt, R. R. How to Accurately Report Transparent Solar Cells. *Joule* **3**, 1803–1809 (2019).
46. Lee, K. *et al.* The Development of Transparent Photovoltaics. *Cell Reports Phys. Sci.* **1**, 100143 (2020).
47. Chen, K. S. *et al.* Semi-transparent polymer solar cells with 6% PCE, 25% average visible transmittance and a color rendering index close to 100 for power generating window applications. *Energy Environ. Sci.* **5**, 9551–9557 (2012).
48. Godfroy, M. *et al.* Benzothiadiazole-based photosensitizers for efficient and stable dye-sensitized solar cells and 8.7% efficiency semi-transparent mini-modules. *Sustain. Energy Fuels* **5**, 144–153 (2021).
49. Distler, A., Brabec, C. J. & Egelhaaf, H. J. Organic photovoltaic modules with new world record efficiencies. *Prog. Photovoltaics Res. Appl.* **29**, 24–31 (2021).
50. Sun, R. *et al.* A Layer-by-Layer Architecture for Printable Organic Solar Cells Overcoming the Scaling Lag of Module Efficiency. *Joule* **4**, 407–419 (2020).

Chapter 7

Multilevel Peel-off Patterning of Semitransparent Organic Photovoltaic Module

The previous chapter focused on reducing the resistance loss when scaling up ST-OPVs. Another primary loss channel in ST-OPV modules is the large area consumed by cell interconnections, which leads to geometric loss as well as deteriorated appearance. The demonstration of efficient, large-scale ST-OPV modules with a GFF approaching 100%, however, remains a challenge due to the lack of precise and high-resolution patterning methods compatible with a broad range of organic materials. In this chapter, we employ a multilevel peel-off patterning method that can achieve micron-scale resolution without exposing chemically sensitive organic materials to solvents. Eight, 4 cm × 0.4 cm cells are connected in series with 200 μm wide interconnections to realize a prototype ST-OPV module with GFF = 95.8%. The ST-OPV module exhibits PCE = 7.3 ± 0.2% under simulated AM1.5G illumination at 1 sun intensity. With an APT = 41.8 ± 1.4%, the light utilization efficiency is LUE = 3.1 ± 0.1%. In addition, a neutral color ST-OPV module is also demonstrated with LUE = 1.7 ± 0.1% and International Commission on Illumination (CIE) LAB coordinates (L^* , a^* , b^*) = (53.7, -1.9, -3.9). The peel-off method provides

a viable pathway for achieving photolithographic patterning resolution in organic electronic devices.

7.1 Peel-off Patterning Method

Organic semiconductors are being employed for a range of modern photonic and electronic devices due to their distinct advantages of low cost, light weight, flexibility, and environmental compatibility.¹ The past few decades have witnessed remarkable developments in the performance of such devices as OLEDs, OPVs and organic thin film transistors (OTFTs). An essential step to realize high volume production of electronic devices is high-resolution patterning techniques.²⁻⁶ While small, laboratory-scale OPVs have demonstrated high PCE with exceptional stability, OPV modules can also benefit from high-resolution patterning, although this has attracted considerably less attention.⁷⁻¹² In particular, OPVs show considerable promise for use in power generating windows due to their transparency across the visible spectrum along with selective absorption in the NIR; a feature resulting from the relatively narrow excitonic absorption spectra of organic semiconductors.¹³⁻¹⁵ To date, ST-OPVs exhibit a light utilization efficiency of $LUE = PCE \times APT$ as high as 5%, where APT is the average photopic transmission.¹⁶⁻²³ To realize practical applications, scalable fabrication processes of modules with minimal loss in power generation need to be established. Considerable loss in OPV module efficiencies and visible artifacts in ST-OPVs arise from the large area consumed by interconnections between constituent cells. Such deficiencies can be significantly reduced by high-resolution patterning.

Conventional module patterning based on mechanical scribing, shadow masking, gravure printing, slot-die coating, etc.²⁴⁻³¹ often yield interconnection widths at the millimeter scale, and result in a low geometric fill factor, GFF, which is the ratio between the active cell and the total

module areas. In contrast, laser ablation has achieved interconnection widths of hundreds of microns.^{32–38} However, ablation can result in damage to the surrounding and materials comprising the device.^{35,39} Moreover, the illumination wavelength and pulse durations must be tailored to ablate only the targeted materials.^{33,35} As a result of these limitations, the highest efficiency opaque OPV modules fabricated with laser ablation have shown approximately 10% PCE loss compared to laboratory-scale devices.^{35,38,40}

An alternative to these methods is photolithographic patterning. However, commonly used photoresists contain solvents that can degrade chemically sensitive organic materials. Moreover, lithographic patterning and photoresist removal can also employ reactive ion- or solvent-based wet chemical processes that can damage organic semiconductors. Here, we employ a patterning method that combines a non-destructive polymer-based peel-off patterning of ST-OPV modules with photolithographic resolution.^{41–47} The general elements of the peel-off patterning process are provided in Fig. 7.1(a). A polymer is first coated on the substrate and patterned into long, narrow strips with conventional photolithography. The choice of the polymer includes, but is not limited to polyimide (PI), parylene, etc. After photoresist removal, the organic layer to be patterned is deposited and the polymer strips are mechanically peeled off, removing the organic on their surfaces from the module. Figure 7.1(b) shows a microscopic image of the organic blend film on a glass substrate patterned by peeling off a 10 μm wide PI strip. The wedge at the edge of the PI strip is picked up to initiate the peel-off. In the method of Fig. 7.1, peel-off produces large scale features with micron-scale resolution. Moreover, this method is independent of the details of the organic materials system or layering scheme and does not damage the chemically sensitive active layers.

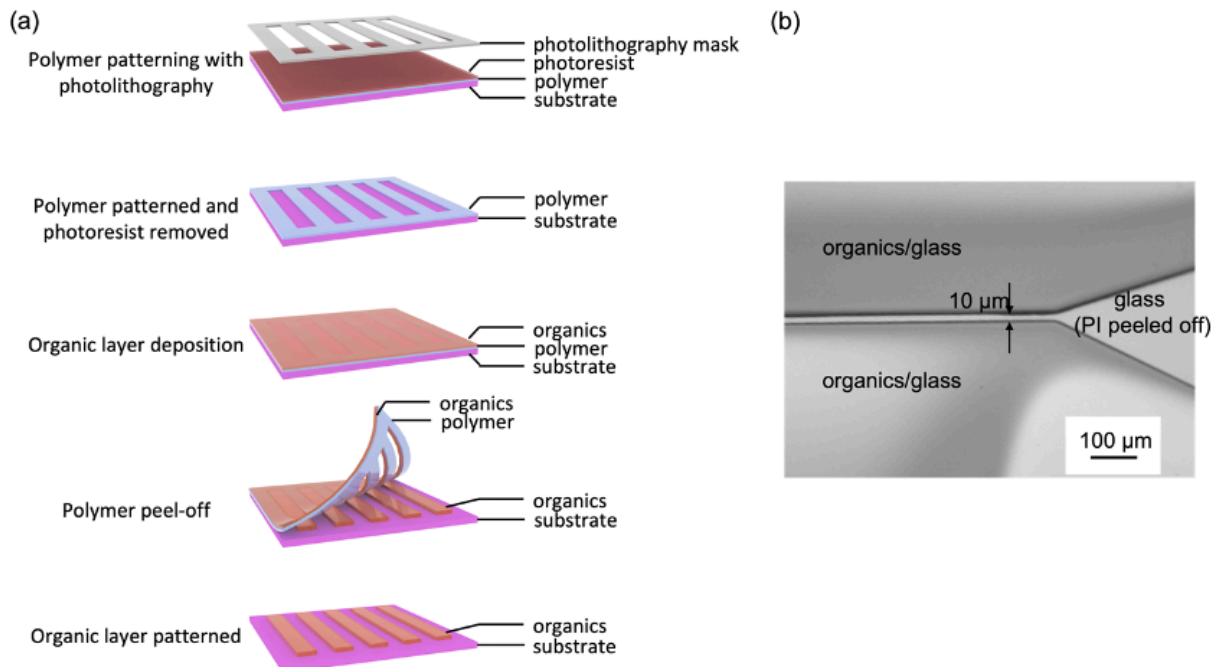


Figure 7.1 Description of the peel-off patterning method.

(a) Schematic illustration of the peel-off patterning procedure. (b) Microscopic image of PCE-10:BT-CIC blend film on a glass substrate patterned by peeling off a 10 μm wide polyimide (PI) strip.

Similar methods have been employed in the patterning of biological materials,^{41–44} organics,^{45,46} and perovskites.⁴⁷ Most of these demonstrations focus primarily on the patterning of micron-scale features with a single level patterning step utilizing one polymer layer to pattern one target layer. To achieve complicated device structures and circuit interconnection in a module, however, multi-step/multilevel peel-off patterning over large substrate areas is essential. In recent work that employs multi-step peel-off patterning, multiple polymer layers are repeatedly deposited and lithographically removed over chemically sensitive materials, which severely degrades the device performance.^{45,47}

In the following sections, we demonstrate multilevel peel-off patterning scheme in the fabrication of prototype opaque and semitransparent OPV mini-modules with GFF = 95.8%. The opaque OPV module reaches PCE = $10.3 \pm 0.3\%$ under simulated AM1.5G illumination at 1 sun intensity, which is only 5% less than an analogous 4 mm² device. Combined with an ultrathin Ag

top electrode and a visible light out-coupling (OC) structure, the ST-OPV module exhibits LUE = $3.1 \pm 0.1\%$ with PCE = $7.3 \pm 0.2\%$ and APT = $41.8 \pm 1.4\%$. The module has a blue-green tint with CIELAB coordinates of $(L^*, a^*, b^*) = (70.9, -11.3, -7.5)$. In addition, a color-neutral ST-OPV module is demonstrated with LUE = $1.7 \pm 0.1\%$ and $(L^*, a^*, b^*) = (53.7, -1.9, -3.9)$.

7.2 Module Fabrication

7.2.1 Multilevel Peel-off to Realize Series Connection

Figure 7.2 details the step-by-step multilevel peel-off patterning procedure to realize series connection between individual OPV cells. The ITO bottom cathode is photolithographically patterned into 4.15 mm wide strips, and a PI layer is coated onto the electrodes. The PI is patterned into parallel, 50 μm and 75 μm wide strips via photolithography. As shown in Fig. 7.2(a), there are pairs of 50 μm and 75 μm PI strips with 50 μm separation at the edge of each cathode strip. Next, the ZnO and MoO₃ charge transport layers as well as the ternary BHJ, comprising a blend of the narrow energy gap polymer donor, PCE-10, and two NIR-absorbing acceptors, BT-CIC and TT-FIC, are deposited, see Fig. 7.2(b).¹⁶ The 75 μm wide strips between two adjacent bottom cathodes are peeled off to separate the charge transport layers and the BHJs of adjacent devices. This exposes a portion of the bottom electrodes to allow series connection between cells, as shown in Fig. 7.2(c). Finally, the Ag anode is deposited, and the remaining 50 μm wide polymer strips are subsequently peeled off to separate the top electrodes of two adjacent devices, see Figs. 7.2(d) and (e). The microscopic image as well as the profilometry profile in Fig. 7.2(e) shows the 200 μm wide interconnection between two individual OPV cells, featuring clean pattern edges.

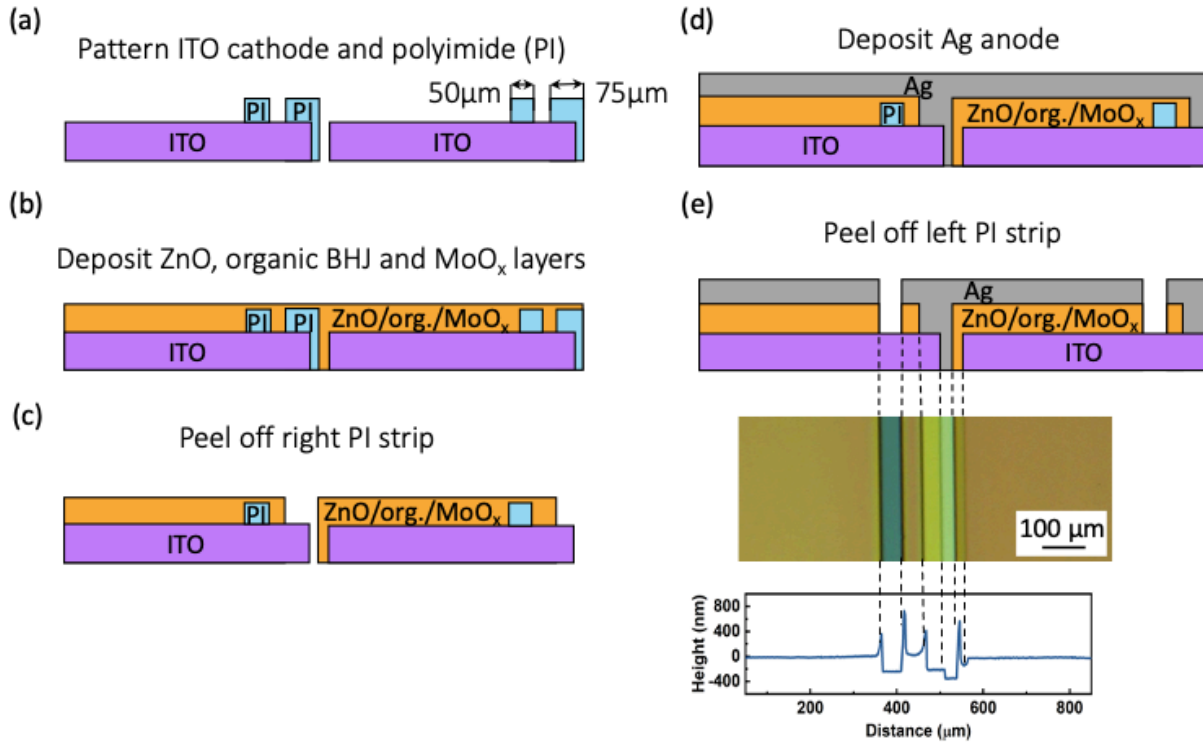


Figure 7.2 Schematic illustration of multilevel peel-off patterning scheme.

(a) to (e) Step-by-step schematic of the fabrication process used to create series cell connection via peel-off patterning. The microscopic image and profilometry profile in (e) shows the interconnection region between two individual ST-OPV cells in a module, with reference to the schematic.

7.2.2 Module Layout Design

In the module, a narrow individual cell width reduces the GFF, while a large width results in increased series resistance loss from the transparent electrodes. Here, the width of individual device is limited to 4 mm to minimize the total loss from both the GFF and series resistance,^{35,48,49} and the length of each cell is 4 cm. The modules comprise eight, series connected 4 cm × 0.4 cm cells separated by 200 µm wide interconnections, resulting in 12.8 cm² active area for a total module area of 13.34 cm² and GFF = 95.8%. A schematic illustration of the completed module is shown in Fig. 7.3(a). Note that, for 10 µm wide PI strips as demonstrated in Fig. 7.1(b), the interconnection distance could potentially be reduced to 40 µm, giving GFF = 99.1%. Furthermore, the resolution and dimension of this patterning method depends on the tensile strength of the

polymer and the stress applied to the strip during peeling, since as it will break if the latter exceeds the former. Therefore, the possibility of failure during peeling is higher when the strip is narrower and longer. These limitations can potentially be circumvented in meter-scale modules patterned at resolutions of tens of microns, for example, by employing a roller to continuously release the stress along the polymer strip during removal, as shown in Fig. 7.3(b).

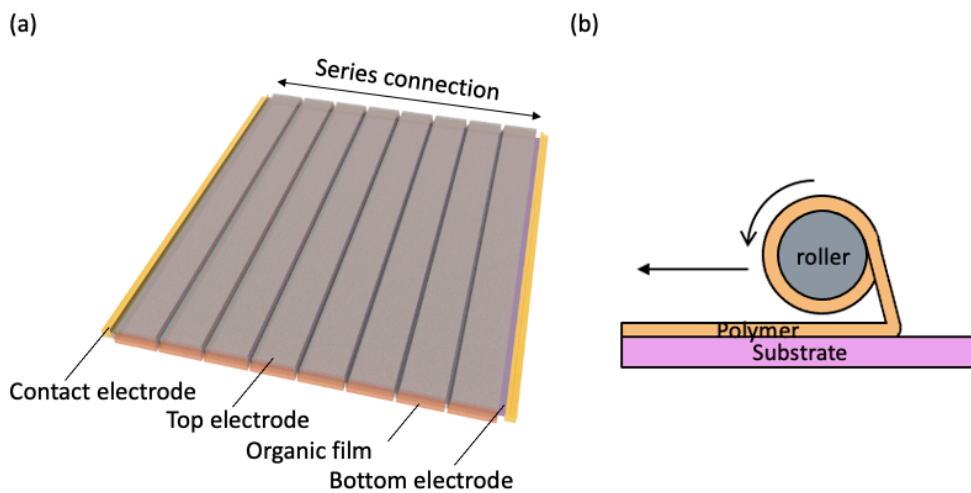


Figure 7.3 Design of module layout.

(a) Schematic of the series connected prototype OPV module layout comprising eight individual cells.

(b) Schematic of a roller-assisted peel-off design for patterning across large surfaces.

7.2.3 Experimental Methods

Substrate preparation

Glass substrates were ultrasonically cleaned with detergent, deionized water and solvents before processing. A 150 nm thick, 15 Ω /sq. indium tin oxide (ITO) layer was sputter-deposited at 1.7 \AA /s in a high vacuum chamber (base pressure $\sim 10^{-6}$ Torr, sputter pressure 3 mTorr) and thermally annealed at 400°C for 5 min in forming gas (5% H_2 + 95% N_2) to reduce the oxygen concentration. The ITO was photolithographically patterned into 4 cm \times 4.15 mm strips, with 50 μm wide separation via wet etching using $\text{HCl}:\text{H}_2\text{O}$ (3:1, v/v). The 4 cm length of the ITO cathode defines the individual device active area. Micro 90[®] was diluted in 1:1 (v/v) de-ionized water and

isopropanol at a concentration of 5% and spin-coated on top of the ITO/glass substrate at 4000 rpm as a peel-off release agent layer. The polyimide (PI-2611) was spin-coated onto the substrate at 5000 rpm followed by soft cure at 90°C and 150°C for 90 s each, and hard baked at 350°C for 30 min, which results in a thickness of 3 μm. A layer of photoresist was spin-coated onto the PI and photolithographically patterned and developed, then the PI layer was etched using O₂ plasma (C₄F₈:O₂:He = 14:56:50 sccm, 30 mTorr chamber pressure, 500 W transformer coupled plasma (TCP) power, 25 W bias power) into 50 μm and 75 μm wide strips. After etching, the sheet resistance of the substrate was measured via four-probe measurement to check whether there was residue of polymer on the ITO. As shown in Fig. 7.2(a), a 50 μm wide PI strip is patterned on each ITO strip, leaving a 4 mm ITO cathode on its left to define the width of the individual cell active areas. A 75 μm wide PI strip (50 μm on the ITO, 25 μm on the glass substrate) is patterned on the edge of each ITO strip, and is located 50 μm from the other strip. All PI strips are patterned with a wedge on one side of their edges, to assist initiation of peel-off with tweezers.

Device fabrication

The substrates with patterned ITO and PI were ultrasonically cleaned with detergent, deionized water and solvents before device fabrication. A ZnO precursor solution was spin-coated onto the substrate at 3000 rpm after filtering through a 0.45 μm pore polytetrafluoroethylene (PTFE) filter, and then baked at 160°C in air for 30 min. The PCE-10:BT-CIC:TT-FIC (1:1.25:0.5, w/w/w) solution was prepared in chlorobenzene with 10% chloroform at a total concentration of 18 mg/mL and stirred overnight at 65°C, 300 rpm. After filtering through a 0.45 μm pore PTFE filter, the solution was spin-coated at 1000 rpm on the ZnO layer in an ultrapure N₂ environment (O₂ < 0.1 ppm, H₂O < 0.1 ppm). The samples were transferred into a high vacuum chamber (base pressure ~10⁻⁷ Torr unless otherwise noted) for thermal evaporation of 20 nm thick MoO₃ at 0.2

Å/s. After the deposition, the 75 μm PI strips between two adjacent cells on the module were peeled off. For opaque devices, 150 nm thick Ag was thermally evaporated at 0.1-0.6 Å/s in vacuum as the top electrode. For semitransparent devices, 16 nm Ag was sputtered at 0.2 Å/s (chamber base pressure $\sim 10^{-6}$ Torr, sputter pressure 20 mTorr) as the top anode. After anode deposition, the 50 μm PI strips left on the module were peeled off. The optical structure was thermally evaporated at 0.5 Å/s for each layer. Modules were encapsulated by bonding a cover glass to the substrate with an ultraviolet-curable epoxy bead around the module periphery.

7.3 Prototype OPV Module Performance

7.3.1 Characterization Method

The J - V characteristics and EQE spectra of 4 mm² devices were measured in a glovebox filled with ultrapure N₂, similar to the measurement methods in previous chapters. The J_{SC} values of 4 mm² devices measured under the simulated AM1.5G illumination are with < 6% relative mismatch compared to the EQE integration. The module I - V characteristics were measured in air using a solar simulator with a 1000 W Xe lamp with an AM1.5G filter (Oriel Instruments, Model 91191) whose 1 sun intensity was calibrated with the Si reference cell, the calculated spectral mismatch factor is between 1.004 and 1.011. The modules were scanned with 0.02V step voltage and 100 ms integration time (Keithley 2400 source measure unit).

The transmission spectra were measured using UV-vis spectrometer (Perkin-Elmer 1050). The reflection spectra were measured using an F20 Filmetric thin film measurement instrument integrated with a spectrometer and a light source from 395 nm to 1032 nm. The CIELAB coordinates and color rendering index are calculated with AM1.5G spectrum as the reference

illumination and the transmitted light spectrum, $T(\lambda) \cdot S(\lambda)$, as the test light spectrum. The correlated color temperature is calculated with the transmitted light spectrum, $T(\lambda) \cdot S(\lambda)$.

7.3.2 Opaque Module

To study the feasibility of the patterning method, we fabricated an opaque OPV module and an analogous 4 mm² device comprising a 150 nm thick ITO bottom cathode, an 80 nm thick PCE-10:BT-CIC:TT-FIC (1:1.25:0.5, w/w/w) blended ternary BHJ, 30 nm thick ZnO and 20 nm thick MoO_x as electron and hole transporting layers, respectively, and a 150 nm thick Ag anode, as illustrated in Fig. 7.4(a). The performance characteristics are shown in Figs. 7.4(b) and (c) with detailed parameters listed in Table 7.1. The module achieves short circuit current $I_{SC} = 36.7 \pm 0.6$ mA, open circuit voltage $V_{OC} = 5.42 \pm 0.02$ V, fill factor $FF = 0.66 \pm 0.01$, and PCE = $10.3 \pm 0.3\%$. Compared to the 4 mm² device, the module shows negligible loss in I_{SC} (individual cell area 1.6 cm², with an average short circuit current density of $J_{SC_AVG} = 22.9$ mA/cm²) and V_{OC} , while the FF decreases from 0.69 ± 0.01 to 0.66 ± 0.01 , which is primarily due to resistance losses from the ITO cathode. Since peel-off does not introduce damage to the materials comprising the devices, the module PCE shows only a 5% decrease compared to the 4 mm² device.

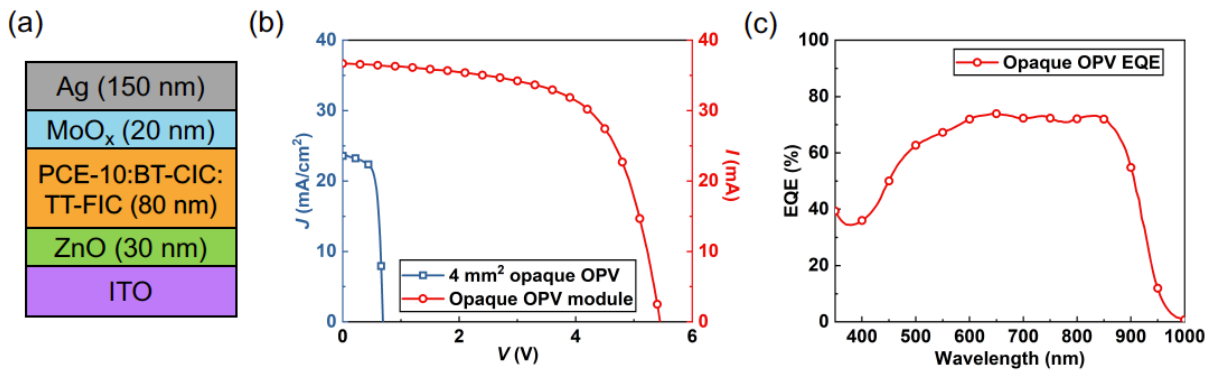


Figure 7.4 Optoelectronic properties of opaque OPV modules.

(a) Schematic of the opaque OPV device structure. (b) J - V and I - V characteristics of an opaque 4 mm² device and module. (c) EQE spectrum of the opaque OPV device.

7.3.3 Semitransparent Module with Optimized APT

The ST-OPVs were fabricated by substituting the thick Ag anode with an ultrathin 16 nm Ag layer, and integrating a 4-layer outcoupling structure comprising CBP (50 nm)/MgF₂ (100 nm)/CBP (80 nm)/MgF₂ (10 nm) (see supplemental experimental procedures),^{16,21} as illustrated in Fig. 7.5(a). Figure 7.5(b) shows the J - V and I - V characteristics of the 4 mm² ST-OPV devices and modules with and without the OC structure. The EQE, transmission, and reflection spectra of the devices are plotted in Figs. 7.5(c) and (d), with detailed performance parameters provided in Table 7.1. The ST-OPV modules show negligible loss in I_{SC} and V_{OC} compared to the analogous 4 mm² devices. The ultrathin Ag top anode introduces additional resistance loss due to its limited conductivity. This results in a reduction in FF from 0.70 ± 0.01 to 0.64 ± 0.01 . Figure 7.5(d) shows that the transmission of ST-OPV device without an OC structure has a peak at a wavelength of $\lambda = 430$ nm, followed by a significant decrease at $\lambda > 500$ nm due to the absorption by the device. To improve the APT, an OC structure was employed to maximize the transmission of visible wavelengths via control of interference peaks in the multilayer stacks.¹⁶ It enhances the transmission between 400 nm and 600 nm, with a peak at 560 nm, which is close to the peak photopic response of the eye. Therefore, the OC structure significantly improves the APT from $22.3 \pm 1.1\%$ to $41.8 \pm 1.4\%$. However, the increase in transparency leads to a reduction of I_{SC} from 28.2 ± 0.7 mA to 27.2 ± 0.5 mA, as shown by the decreased EQE in Fig. 7.5(c). As a result, the ST-OPV module with the OC structure exhibits $PCE = 7.3 \pm 0.2\%$ with high reproducibility (Figure 7.5(e)) and reaches $LUE = 3.1 \pm 0.1\%$.

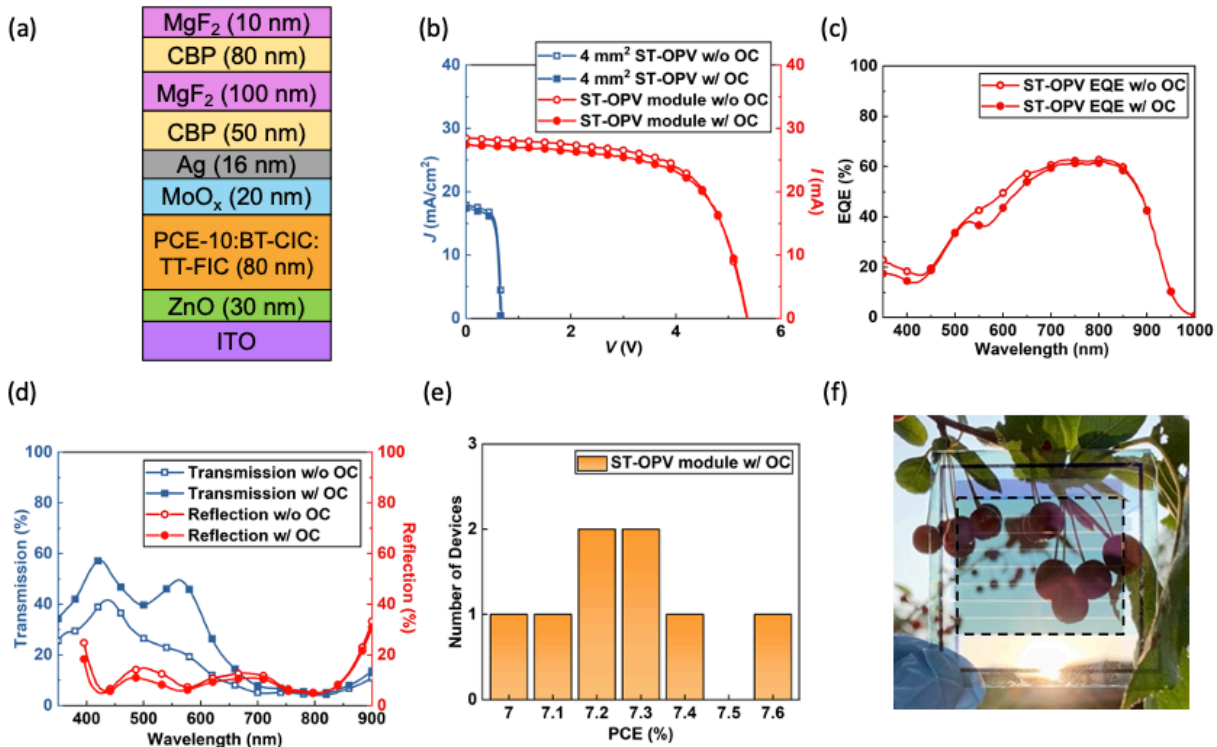


Figure 7.5 Optoelectronic properties of the ST-OPV modules with out-coupling (OC) structure.

(a) Schematic of the ST-OPV device with an optical OC structure. (b) J - V and I - V characteristics of 4 mm² ST-OPV devices and modules with and without the OC structure. (c) EQE and (d) transmission and reflection spectra of the ST-OPV with and without OC structure. (e) Distribution of PCE of eight ST-OPV modules with the OC structure. (f) Photographic image of the prototype ST-OPV module with the OC structure.

A photographic image of the module with OC structure is shown in Fig. 7.5(f). The module area (outline with a black dashed box) shows a transparent, tint and narrow, bright lines from transmission through the gaps in the interconnection regions. This effect can be reduced, either by increasing the APT to reduce the contrast between the active and interconnection areas, or by patterning narrower stripes. Ideally, modules used as window panels should transmit light as close to neutral color as possible, which requires (a^*, b^*) coordinates in the CIELAB color space that approach $(0, 0)$. The ST-OPV module with OC exhibits CIELAB coordinates $(L^*, a^*, b^*) = (70.9, -11.3, -7.5)$, which accounts for its blue-green tint.

Table 7.1 Performance of 4 mm² PCE-10:BT-CIC:TT-FIC OPV device, and 12.8 cm² active area (13.34 cm² total area) module under simulated AM1.5G illumination at 1 sun intensity.

4 mm ² device	J_{SC} (mA/cm ²)	V_{OC} (V)	FF (%)	PCE (%)	APT (%)	LUE (%)
opaque	23.2 ± 0.4	0.68 ± 0.01	0.69 ± 0.01	10.9 ± 0.3	-	-
ST w/o OC	17.8 ± 0.3	0.67 ± 0.01	0.70 ± 0.01	8.3 ± 0.2	22.3 ± 1.1	1.9 ± 0.1
ST w/ OC	17.1 ± 0.2	0.67 ± 0.01	0.70 ± 0.01	8.0 ± 0.2	41.8 ± 1.4	3.3 ± 0.1
neutral ST	17.4 ± 0.3	0.67 ± 0.01	0.70 ± 0.01	8.2 ± 0.1	22.8 ± 1.3	1.9 ± 0.1
module	I_{SC} (mA)	PCE_{active}^a (%)				
opaque	36.7 ± 0.6	5.42 ± 0.02	0.66 ± 0.01	10.3 ± 0.3	-	-
ST w/o OC	28.2 ± 0.7	5.34 ± 0.02	0.64 ± 0.01	7.5 ± 0.3	22.3 ± 1.1	1.7 ± 0.1
ST w/ OC	27.2 ± 0.5	5.34 ± 0.02	0.64 ± 0.01	7.3 ± 0.2	41.8 ± 1.4	3.1 ± 0.1
neutral ST	27.4 ± 0.4	5.34 ± 0.02	0.64 ± 0.01	7.4 ± 0.2	22.8 ± 1.3	1.7 ± 0.1

a: PCE calculated based on module active area.

7.3.4 Neutral Color Semitransparent Module

To realize neutral color ST-OPV modules, we employed a 4-layer optical structure consisting of CBP (45 nm)/ZnS (45 nm)/CBP (110 nm)/MgF₂ (10nm), as illustrated in Fig. 7.6(a), whose $J-V$ and $I-V$ characteristics are shown in Fig. 7.6(b), with detailed performance parameters listed in Table 1. The module exhibits $I_{SC} = 27.6 \pm 0.4$ mA, $V_{OC} = 5.34 \pm 0.02$ V and $FF = 0.64 \pm 0.01$, which yields $PCE = 7.4 \pm 0.2\%$. The EQE, transmission and reflection spectra are plotted in Fig. 7.6(c). Compared to the device without the OC structure, the transmission of neutral color ST-OPV decreases between $\lambda = 400$ nm and 500 nm, and increases between 550 nm and 650 nm, to reach a balance over the visible region. The neutral color module achieves $(L^*, a^*, b^*) = (53.7, -$

1.9, -3.9), a high color rendering index (CRI) of 88, and a correlated color temperature (CCT) of 5944 K, which is close to the solar surface temperature of 5776K. The APT and LUE of the module are $22.8 \pm 1.3\%$ and $1.7 \pm 0.1\%$, respectively. Figure 7.6(d) shows a photographic image with the module area bordered by a black dashed box. The illumination through the module can accurately render the colors of white, red, green and blue in the background.

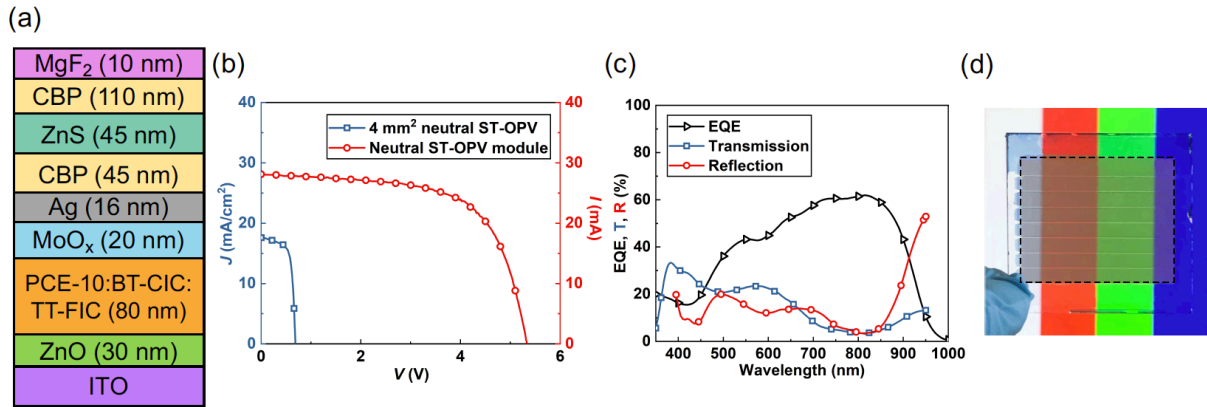


Figure 7.6 Optoelectronic properties of the neutral color ST-OPV modules.

(a) Schematic of the neutral color ST-OPV device. (b) J - V and I - V characteristics of 4 mm^2 neutral color ST-OPV device and module. (c) EQE, transmission and reflection spectra of the neutral color ST-OPV. (d) Photographic image of the prototype, neutral color ST-OPV module.

7.3.5 Discussion

Note that the mini-modules fabricated using peel-off are, to our knowledge, the first demonstration of OPV modules that overcomes the considerable PCE loss observed in other high resolution patterning processes. Its resolution suggests that the strips can be made even narrower than demonstrated, leading to GFF approaching unity.

Finally, while we cannot make a precise comparison between the costs of peel-off patterning and the widely used laser ablation patterning, a large capital expenditure in laser patterning arises from the acquisition of precise, large-scale laser ablation tools, whose illumination wavelength may have to be adjusted for specific materials and device structures. In

contrast, the photolithographic tools used in peel-off patterning are standard in semiconductor and OLED processing lines, thus reducing the cost of capital and depreciation. However, the peel-off method requires additional costs of materials used for the polymer patterning layer and in the photolithographic processes, which scale with the size of the solar panels. An accurate comparison of costs admittedly warrants further study which is beyond the scope of this demonstration.⁵⁰

7.4 Application of Peel-off Patterning in Other Organic Electronic Devices

7.4.1 Polariton-based Photodetector

With the peel-off patterning method, a polariton-based photocurrent generation device that mimics the architecture of natural photosynthetic complexes was demonstrated.⁵¹ The device combines a polariton antenna capable of long range energy transport that directs excited states to an integrated photodetecting heterojunction (HJ) reaction center (RC). Figure 7.7(a) illustrates the device structure. A thin film of a donor material, DBP, is deposited on the surface of a distributed Bragg reflector (DBR), which serves as the light gathering antenna. The antenna is edge-coupled into a bilayer donor-acceptor HJ RC composed of donor DBP and acceptor C_{70} . The RC harvests the excitation energy by dissociation into an electron and hole that are collected at the Au anode and the Ag cathode. The microscopic image of such device is shown in Fig. 7.7(b), where d is the distance between the laser pump spot and the device RC. The device is employed to investigate the long-range propagation via photodetection of organic exciton polaritons, and the photocurrent density-voltage (J_{ph} - V) characteristics as a function of d is shown in Fig. 7.7(c). The J_{ph} of the polariton-based photodetector device shows pronounced dependence on d , indicating enhanced the distance-dependent photodetection response when the organic excitons hybridize with the

propagating Bloch surface wave (BSW) mode, allowing for long-range polariton-mediated energy transport.

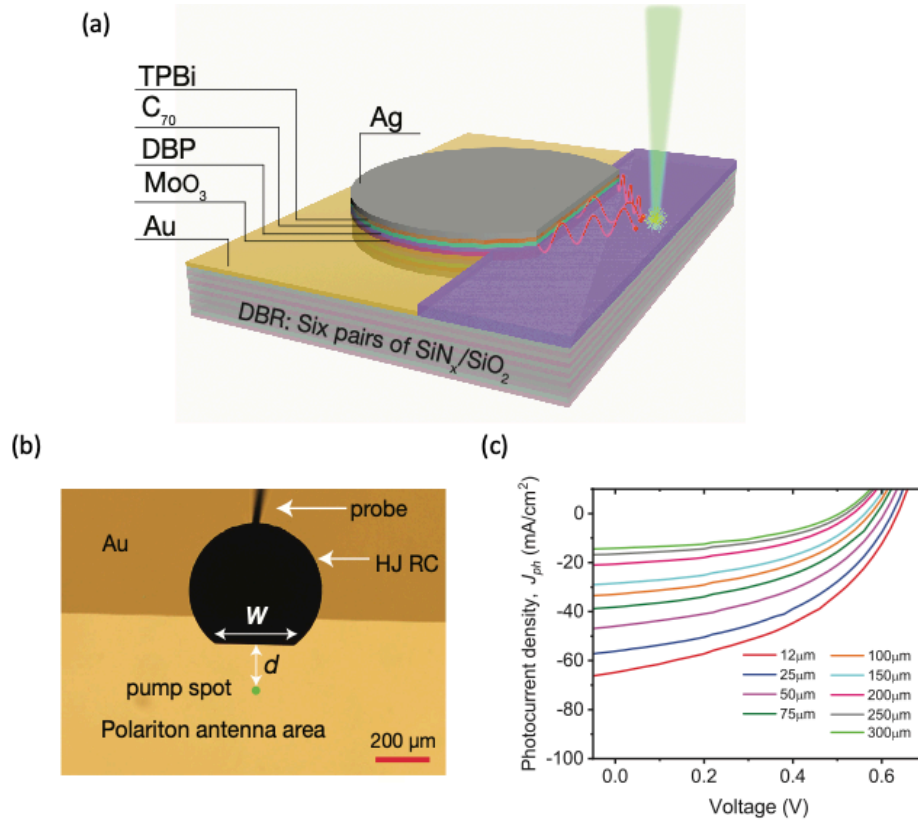


Figure 7.7 Peel-off patterned polariton-based organic photodetector.

- (a) Schematic illustration of the device structure. (b) Microscopic image of the top view of the device. (c) Photocurrent-voltage (J_{ph} - V) characteristics of the polariton device as a function of distance, d .

7.4.2 Side-by-side White OLED Solid-state Lighting

The peel-off patterning method has also been employed to demonstrate two color side-by-side (S×S) white OLED for solid-state lighting to reach micron scale resolution while avoiding precise alignment of shadow masks.⁵² Figure 7.8(a) illustrates the device structure comprising 100 μm wide blue and yellow emissive stripes separated by 50 μm , the 25 μm buffer zone is designed to spatially separate two polymer stripes for sequential peel-off. The narrow individual emissive stripes cannot be resolved by human eyes when viewed in the far field, resulting in diffuse white

light illumination shown in Fig. 7.8(b). Such S×S geometry also allows for color tunability by varying the ratio of current applied to the blue stripe and yellow stripes (I_B/I_Y). Figure 7.8(c) plots CCT and CRI vs. I_B/I_Y when maintaining the luminance at 1000 cd m^{-2} . The maximum CRI = 86 ± 1 is reached at CCT = $2000 \pm 200 \text{ K}$ and CIE color coordinates of (0.30,0.36) due to the dominance of the yellow stripe emission. In addition, the S×S white OLED exhibits reliability comparable to that of devices patterned by shadow mask owing to the non-destructive nature of the peel-off method.

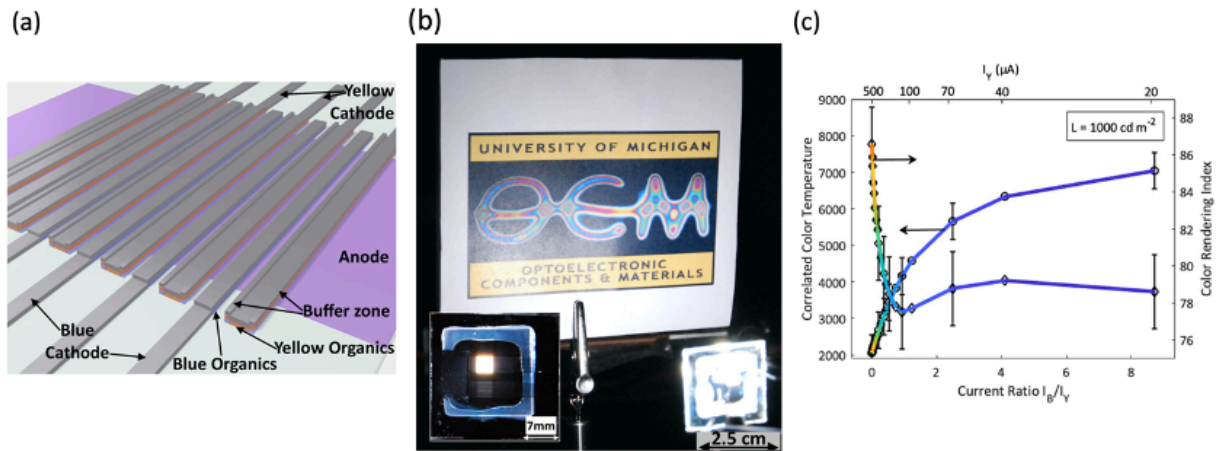


Figure 7.8 Peel-off patterned side-by-side white OLED for solid state lighting.

(a) Illustration of the device active area. (b) Photograph of the OCM group logo illuminated by a 0.63 cm^2 device. The inset is the photograph of the device in forward bias. (c) color rendering index (CRI) and correlated color temperature (CCT) vs. I_B/I_Y , the ratio of current separately applied to the blue and yellow stripes, respectively. The luminance is held constant at 1000 cd/m^2 . The top horizontal axis shows the corresponding values of I_Y .

7.5 Conclusion

In this work, we introduced a peel-off patterning technique that can achieve micron-scale patterning resolution of organic materials without introducing damage incurred using conventional photolithography. Using this method, we fabricated prototype, series-connected OPV modules with 12.8 cm^2 active area and GFF = 95.8%. An opaque OPV module was demonstrated with PCE = $10.3 \pm 0.3\%$, which features a remarkably small PCE loss of only 5% compared to analogous 4

mm² devices. ST-OPV modules were fabricated by utilizing ultrathin Ag top electrode and an OC structure. The optimized ST-OPV module achieves LUE = $3.1 \pm 0.1\%$ with PCE = $7.3 \pm 0.2\%$ and APT = $41.8 \pm 1.4\%$. Furthermore, we demonstrated a neutral color ST-OPV module with LUE = $1.7 \pm 0.1\%$ and $(L^*, a^*, b^*) = (53.7, -1.9, -3.9)$. The peel-off patterning technique introduces the possibility for realizing ST-OPV modules with high efficiency and GFF approaching 100% over large areas. In addition, we introduced the applications of such peel-off patterning method in various kinds of organic optoelectronic devices. Our result is general in that it shows a potential path for multilevel, high-resolution patterning with micron-scale resolution of chemically sensitive organic electronic materials over large areas.

Chapter 7

Bibliography

1. Forrest, S. R. *Organic Electronics: Foundations to Applications*. (Oxford University Press, 2020).
2. Li, J., Xu, L., Tang, C. W. & Shestopalov, A. A. High-Resolution Organic Light-Emitting Diodes Patterned via Contact Printing. *ACS Appl. Mater. Interfaces* **8**, 16809–16815 (2016).
3. Kim, C., Burrows, P. E. & Forrest, S. R. Micropatterning of organic electronic devices by cold-welding. *Science (80-.)*. **288**, 831–833 (2000).
4. Kim, C. & Forrest, S. R. Fabrication of organic light-emitting devices by low-pressure cold welding. *Adv. Mater.* **15**, 541–545 (2003).
5. Ling, M. M. & Bao, Z. Thin film deposition, patterning, and printing in organic thin film transistors. *Chem. Mater.* **16**, 4824–4840 (2004).
6. Höppner, M., Kneppel, D., Kleemann, H. & Leo, K. Precise patterning of organic semiconductors by reactive ion etching. *Org. Electron.* **76**, 105357 (2020).
7. Che, X., Li, Y., Qu, Y. & Forrest, S. R. High fabrication yield organic tandem photovoltaics combining vacuum- and solution-processed subcells with 15% efficiency. *Nat. Energy* **3**, 422–427 (2018).
8. Meng, L. *et al.* Organic and solution-processed tandem solar cells with 17.3% efficiency. *Science* **361**, 1094–1098 (2018).
9. Cui, Y. *et al.* Single-Junction Organic Photovoltaic Cells with Approaching 18% Efficiency. *Adv. Mater.* **32**, (2020).
10. Cui, Y. *et al.* Single-Junction Organic Photovoltaic Cell with 19% Efficiency. *Adv. Mater.*

- 33**, 2102420 (2021).
11. Burlingame, Q. *et al.* Intrinsically stable organic solar cells under high-intensity illumination. *Nature* **573**, 394–397 (2019).
 12. Li, Y. *et al.* Non-fullerene acceptor organic photovoltaics with intrinsic operational lifetimes over 30 years. *Nat. Commun.* 2021 121 **12**, 1–9 (2021).
 13. Lunt, R. R. & Bulovic, V. Transparent, near-infrared organic photovoltaic solar cells for window and energy-scavenging applications. *Appl. Phys. Lett.* **98**, 113305 (2011).
 14. Meiss, J., Holzmueller, F., Gresser, R., Leo, K. & Riede, M. Near-infrared absorbing semitransparent organic solar cells. *Appl. Phys. Lett.* **99**, 10–13 (2011).
 15. Li, Y. *et al.* High Efficiency Near-Infrared and Semitransparent Non-Fullerene Acceptor Organic Photovoltaic Cells. *J. Am. Chem. Soc.* **139**, 17114–17119 (2017).
 16. Li, Y. *et al.* Enhanced Light Utilization in Semitransparent Organic Photovoltaics Using an Optical Outcoupling Architecture. *Adv. Mater.* **31**, 1903173 (2019).
 17. Li, Y. *et al.* Color-neutral, semitransparent organic photovoltaics for power window applications. *Proc. Natl. Acad. Sci. U. S. A.* **117**, 21147–21154 (2020).
 18. Liu, Q. *et al.* Light Harvesting at Oblique Incidence Decoupled from Transmission in Organic Solar Cells Exhibiting 9.8% Efficiency and 50% Visible Light Transparency. *Adv. Energy Mater.* (2020). doi:10.1002/aenm.201904196
 19. Bai, Y. *et al.* Interfacial engineering and optical coupling for multicolored semitransparent inverted organic photovoltaics with a record efficiency of over 12%. *J. Mater. Chem. A* **7**, 15887–15894 (2019).
 20. Wang, D. *et al.* High-Performance Semitransparent Organic Solar Cells with Excellent Infrared Reflection and See-Through Functions. *Adv. Mater.* **32**, 2001621 (2020).

21. HKM Sheriff, Y. L. B. Q. S. F. Aperiodic optical coatings for neutral-color semi-transparent organic photovoltaics. *Appl. Phys. Lett.* **118**, 033302 (2021).
22. Jeong, H. I. *et al.* Rational Design of Highly Efficient Semi-Transparent Organic Photovoltaics with Silver Nanowire Top Electrode via 3D Optical Simulation Study. *Adv. Energy Mater.* 2102397 (2021).
23. Huang, X. *et al.* Novel Narrow Bandgap Terpolymer Donors Enables Record Performance for Semitransparent Organic Solar Cells Based on All-Narrow Bandgap Semiconductors. *Adv. Funct. Mater.* 2108634 (2021).
24. Huang, X., Fan, D. & Forrest, S. R. Scalable semitransparent prototype organic photovoltaic module with minimal resistance loss. *Org. Electron.* **97**, 106276 (2021).
25. Lim, D. C. *et al.* Semi-transparent plastic solar cell based on oxide-metal-oxide multilayer electrodes. *Prog. Photovoltaics Res. Appl.* **26**, 188–195 (2018).
26. Dong, S., Jia, T., Zhang, K., Jing, J. & Huang, F. Single-Component Non-halogen Solvent-Processed High-Performance Organic Solar Cell Module with Efficiency over 14%. *Joule* **4**, 2004–2016 (2020).
27. Heo, Y.-J. *et al.* Small-Molecule Organic Photovoltaic Modules Fabricated via Halogen-Free Solvent System with Roll-to-Roll Compatible Scalable Printing Method. *ACS Appl. Mater. Interfaces* **9**, 39519–39525 (2017).
28. Kutsarov, D. I. *et al.* Fabrication of air-stable, large-area, PCDTBT:PC70BM polymer solar cell modules using a custom built slot-die coater. *Sol. Energy Mater. Sol. Cells* **161**, 388–396 (2017).
29. Bernardo, G., Lopes, T., Lidzey, D. G. & Mendes, A. Progress in Upscaling Organic Photovoltaic Devices. *Adv. Energy Mater.* **11**, (2021).

30. Wang, G., Adil, M. A., Zhang, J. & Wei, Z. Large-Area Organic Solar Cells: Material Requirements, Modular Designs, and Printing Methods. *Adv. Mater.* **31**, 1–34 (2019).
31. Chen, H. *et al.* A guest-assisted molecular-organization approach for >17% efficiency organic solar cells using environmentally friendly solvents. *Nat. Energy* **2021 611 6**, 1045–1053 (2021).
32. Lucera, L. *et al.* Printed semi-transparent large area organic photovoltaic modules with power conversion efficiencies of close to 5 %. *Org. Electron.* **45**, 209–214 (2017).
33. Kubis, P. *et al.* Patterning of organic photovoltaic modules by ultrafast laser. *Prog. Photovoltaics Res. Appl.* **23**, 238–246 (2015).
34. Strohm, S. *et al.* P3HT: Non-fullerene acceptor based large area, semi-transparent PV modules with power conversion efficiencies of 5%, processed by industrially scalable methods. *Energy Environ. Sci.* **11**, 2225–2234 (2018).
35. Distler, A., Brabec, C. J. & Egelhaaf, H. J. Organic photovoltaic modules with new world record efficiencies. *Prog. Photovoltaics Res. Appl.* **29**, 24–31 (2021).
36. Pascual-San-José, E. *et al.* Towards photovoltaic windows: Scalable fabrication of semitransparent modules based on non-fullerene acceptors via laser-patterning. *J. Mater. Chem. A* **8**, 9882–9895 (2020).
37. Lucera, L. *et al.* Highly efficient, large area, roll coated flexible and rigid OPV modules with geometric fill factors up to 98.5% processed with commercially available materials. *Energy Environ. Sci.* **9**, 89–94 (2016).
38. Wang, D. *et al.* High-performance see-through power windows. *Energy Environ. Sci.* (2022). doi:10.1039/D2EE00977C
39. Röttinger, S. *et al.* Laser patterning of vacuum processed small molecular weight organic

- photovoltaics. *Sol. Energy Mater. Sol. Cells* **154**, 35–41 (2016).
40. Dong, X. *et al.* Large-Area Organic Solar Modules with Efficiency Over 14%. *Adv. Funct. Mater.* 2110209 (2021). doi:10.1002/ADFM.202110209
 41. Ilic, B. & Craighead, H. G. Topographical patterning of chemically sensitive biological materials using a polymer-based dry lift off. *Biomed. Microdevices* **2**, 317–322 (2000).
 42. Tan, C. P. *et al.* Parylene peel-off arrays to probe the role of cell–cell interactions in tumour angiogenesis. *Integr. Biol.* **1**, 587–594 (2009).
 43. Tan, C. P., Cipriany, B. R., Lin, D. M. & Craighead, H. G. Nanoscale Resolution, Multicomponent Biomolecular Arrays Generated By Aligned Printing With Parylene Peel-Off. *Nano Lett.* **10**, 719–725 (2010).
 44. Martinez, D. *et al.* Polymer peel-off mask for high-resolution surface derivatization, neuron placement and guidance. *Biotechnol. Bioeng.* **110**, 2236–2241 (2013).
 45. Defranco, J. A., Schmidt, B. S., Lipson, M. & Malliaras, G. G. Photolithographic patterning of organic electronic materials. *Org. Electron.* **7**, 22–28 (2006).
 46. Abbas, A. S. *et al.* Metal and organic nanostructure fabrication by electron beam lithography and dry liftoff. *Proc. IEEE Conf. Nanotechnol.* 392–395 (2014). doi:10.1109/NANO.2014.6968083
 47. Zou, C., Chang, C., Sun, D., Böhringer, K. F. & Lin, L. Y. Photolithographic patterning of perovskite thin films for multicolor display applications. *Nano Lett.* **20**, 3710–3717 (2020).
 48. Rowell, M. W. & McGehee, M. D. Transparent electrode requirements for thin film solar cell modules. *Energy Environ. Sci.* **4**, 131–134 (2011).
 49. Lucera, L. *et al.* Guidelines for Closing the Efficiency Gap between Hero Solar Cells and

- Roll-To-Roll Printed Modules. *Energy Technol.* **3**, 373–384 (2015).
50. Lee, B., Lahann, L., Li, Y. & Forrest, S. R. Cost estimates of production scale semitransparent organic photovoltaic modules for building integrated photovoltaics. *Sustain. Energy Fuels* **4**, 5765–5772 (2020).
51. Liu, B. *et al.* Photocurrent generation following long-range propagation of organic exciton–polaritons. *Optica* **9**, 1029–1036 (2022).
52. Arneson, C., Huang, X. & Forrest, S. R. Solid-State Lighting Using Side-by-Side White Phosphorescent Organic Light-Emitting Diodes. *ACS Photonics* **10**, 526–533 (2023).

Chapter 8

Outlook

High performance OPV devices have become an attractive solution to solar energy harvesting due to the advantages of environmental compatibility, flexibility, transparency, and scalability. Ternary OPVs that employ three molecular species in the BHJ are considered an effective strategy to improve OPV efficiency with broader absorption and reduced energy loss. In this thesis, we investigated the mechanism in ternary OPVs by assessing existed models as well as discovering new phenomena. Specifically, we studied the validity of the concept of a “molecular alloy” in the alloy model. Furthermore, we explored the end-capping exchange reaction during fabrication of ternary BHJ and the impact of the dipolar reaction products. In addition, we also demonstrated the application of NIR-absorbing ternary OPVs in tandem OPV and semitransparent OPV modules. With non-destructive scalable fabrication techniques, the PCE loss from laboratory scale to a large area module can be minimized, which provides viable pathways to the commercialization of ST-OPV technologies. In this chapter, we will discuss the potential challenges for further understanding the operating principles of ternary OPVs that have end-capping exchange. Moreover, we also provide prospects in developing ST-OPV technologies towards application in the BIPV industry.

8.1 Remaining Challenges in Understanding Ternary OPVs

8.1.1 Ternary OPVs with End-capping Exchange

As discussed in Chapter 3, the end-capping exchange reaction between A-D-A type NFAs during device fabrication results in new molecular species in the ternary BHJ. The new components have been shown to impact the photogeneration processes of the blend and lead to decreased FF and PCE. However, the V_{OC} of “hot” ternary device with new molecular species is the same as that of a “cold” ternary device (Fig. 3.6 and Fig. 3.7), which lacks appropriate explanation.

To systematically investigate whether this phenomenon is general at different NFA blend ratios, ternary OPVs based on PCE-10:BT-IC:BTIC-4Cl at blend ratios of $1 : 1.5 \cdot x : 1.5 \cdot (1 - x)$ with x varying from 0 to 1 were fabricated as the same device structure in Fig. 3.6(a). The relationship between V_{OC} and the blend ratio x is plotted in Fig. 8.1.

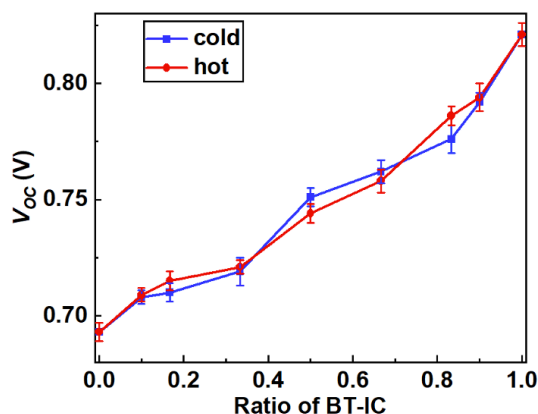


Figure 8.1 Relationship between V_{OC} and blend ratio of cold and hot ternary devices.
The V_{OC} of cold and hot ternary blend OPVs as a function of the blend ratio between BTIC:BTIC-4Cl.

The results show that the V_{OC} of ternary devices changes with blend ratio, indicating that the cascade model of ternary OPVs (charge transfer and energy transfer models in Fig. 1.15) does not apply to this ternary system. Moreover, the “hot” and “cold” ternary devices with the same

blend ratio between BT-IC and BTIC-4Cl have the same V_{OC} . As demonstrated in Chapter 3, the “hot” ternary blends contain the dipolar reaction product BTIC-2Cl, leading to different blend composition and morphology compared to the “cold” ternaries, which will impact V_{OC} if the working principle of the BHJ follows the parallel diodes or alloy model. Therefore, the conventional models cannot fully explain the V_{OC} of the “hot” ternary devices. A more comprehensive interpretation on the photogeneration processes in such NFA based ternary devices warrants further study. To understand the origin of V_{OC} of OPVs, common methods include the measurements of frontier orbitals and CT states. Especially, the broadening of DOS around frontier orbitals should be considered as the morphological disorder introduced by the reaction may induce broader DOS and impact charge transfer. In addition, since the energy barriers between the reaction products and original NFAs are usually small and may be overcome at room temperature, low-temperature measurement is a feasible method to provide further insight on the charge transport in the BHJ.

8.1.2 Mechanism of Multi-nary OPVs

Previous studies have primarily focused on the working mechanisms of ternary OPVs comprising three molecular species, while multi-nary OPVs comprising more than three components have also shown potential in improving performance in recent years.¹⁻³ In addition, the end-capping exchange reaction may produce up to seven chemical species in ternary OPVs based on one donor and two NFAs. Therefore, further investigation on the photogeneration process in multi-nary BHJ is essential for further optimization on device performance as well as understanding ternary OPVs where interactions between NFAs exist.

Figure 8.2 shows an example of quaternary OPVs based on PCE-10:BT-IC:BTIC-4Cl:BTIC-2Cl, the BHJs were prepared in cold solutions to impede end-capping exchange reaction. As shown in Figs. 8.2 (a) and (b), when BT-IC:BTIC-4Cl is 3:1 or 1:1, with increasing ratio of BTIC-2Cl, the V_{OC} of the quaternary devices maintain the same value as that of PCE-10:BT-IC:BTIC-4Cl ternary devices. On the contrary, Figure 8.2(c) shows that when BTIC:BTIC-4Cl = 1:3, the V_{OC} of the quaternary devices changes monotonically with the blend ratio of BTIC-2Cl, indicating that the impact of the fourth component, BTIC-2Cl, is dependent on the ratio between other NFA species. The working principles of multi-nary OPVs are complicated due to the participation of multiple components in charge dissociation and percolation, and the impact of each constituent is correlated to other molecules. Among all performance parameters, V_{OC} , as well as the frontier orbitals, CT states and morphology of multi-nary BHJs, can be investigated to further understand their working mechanisms, owing to their relationship with the energy levels of molecular orbitals participating in photocurrent generation. Further studies, including experiments with controlled blend ratios and analytical models, are required to understand the mechanism of such complex multi-component blend system.

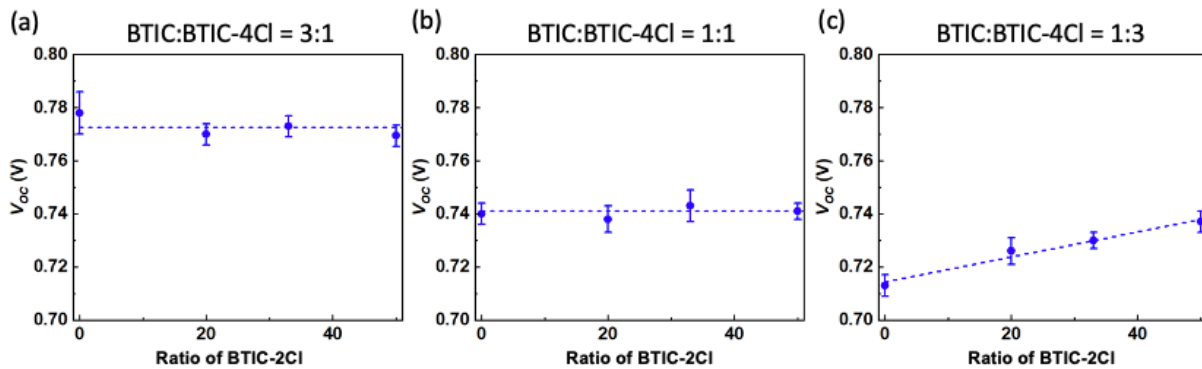


Figure 8.2 Relationship between V_{OC} and blend ratio of quaternary OPVs.

Relationship between V_{OC} and blend ratio of BTIC-2Cl in PCE-10:BT-IC:BTIC-4Cl:BTIC-2Cl quaternary devices in the situations that BTIC:BTIC-4Cl is (a) 3:1, (b) 1:1, and (c) 1:3.

8.2 Prospects for ST-OPVs

8.2.1 Scalability of ST-OPVs

Scaling ST-OPVs to large, window-sized areas introduces several issues not found in small laboratory-scale devices: yield loss due to defects and non-uniformities in thin film composition and thickness, efficiency loss from series resistance (R_s), and the geometric loss and deteriorated aesthetics due to large interconnection areas between constituent cells. Here, we will discuss the cell-to-module efficiency loss of ST-OPVs and possible strategies to overcome the limitations.

Module layout design

Figure 8.3(a) shows the calculated module efficiency loss with a cell width varied from 1 mm to 1 cm, and an interconnection width between cells from 0 to 1.5 mm, as a function of the total sheet resistance (R_{sheet}) of electrodes. As indicated from the calculation, a larger interconnection width and larger R_{sheet} both result in increased efficiency loss of ST-OPV modules. It should be noted that the influence of electrode resistance on module efficiency depends on the width of the discrete cells, which is the distance charge must travel before recombination or collection,^{4,5} indicating that larger cell width leads to increased resistance loss. In contrast, the geometric loss is dependent on the ratio between interconnection width and individual cell width, which decreases with increased cell width. As a consequence, when R_{sheet} and interconnection width are limited at certain values due to the choices of electrode materials and patterning methods, the efficiency loss can be minimized by optimization on discrete cell width. For example, when $R_{sheet} = 30 \Omega/\text{sq}$ and the interconnection distance between cells is 800 μm , the optimum cell width is 4.5 mm, whereas the optimum cell width is 6 mm when $R_{sheet} = 10 \Omega/\text{sq}$ and interconnection width is 500 μm .

Resistance loss

ST-OPV needs both transparent top and bottom electrodes to provide lateral transport of charge carriers. The relative low conductivity of transparent electrodes introduces dramatic R_S loss when scaling up. In Fig. 8.3(b), we summarize the visible transmittance (T) and R_{sheet} of several representative transparent electrode.⁶ The dashed box, which corresponds to $T > 80\%$ and $R_{sheet} < 20\Omega/sq$, represents the optimal region for transparent electrodes useful for ST-OPV modules.

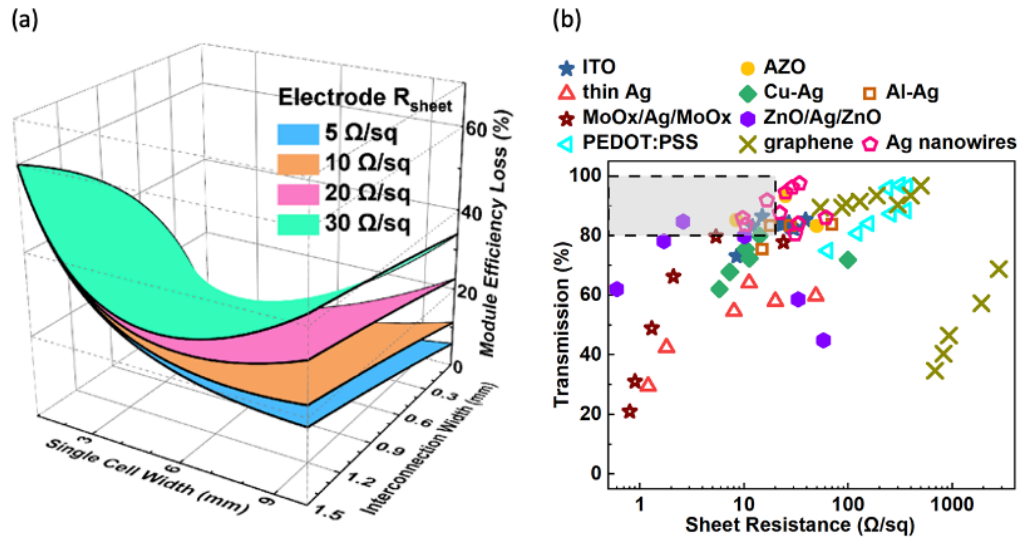


Figure 8.3 Efficiency loss in ST-OPV modules.

(a) Calculated cell-to-module efficiency loss as a function of electrode sheet resistance (R_{sheet}), individual cell width and interconnection width between sub-cells. (b) Visible transparency and R_{sheet} of representative transparent electrode materials used in ST-OPVs. Figure reproduced from Ref.⁶

Conductive metal oxides such as ITO with $R_{sheet} \leq 15 \Omega/sq$ and $T > 80\%$ are most widely used,^{7–11} while their application as the top electrode is limited by the high temperature required during fabrication.⁶ Another candidate for transparent electrodes are ultrathin metal layers, such as Ag.¹² Metal doping of Cu or Al can help avoid aggregation into islands during deposition and improve both conductivity and transparency.^{13–15} Furthermore, by integrating ultrathin metal layer between dielectric layers with appropriate refractive indexes and thicknesses,^{14,16–18} the multilayer stacks can reach $R_{sheet} \sim 10 \Omega/sq$ and $T \sim 80\%$.^{16,19} Other candidates for transparent electrodes include conductive polymers such as PEDOT:PSS,^{20,21} and nanoscale materials such as graphene

and metal nanowires.^{22–24} For example, Ag nanowire electrodes can reach $R_{sheet} = 10\text{--}100 \text{ } \Omega/\text{sq}$ and $T > 80\%$ ^{25,26}, while the challenges of using nanowire electrodes in ST-OPVs are their surface roughness, poor adhesion, and lower operational stability due to rapid oxidation.

To reduce the R_S loss in ST-OPV modules, more effort is required to develop transparent electrode materials with both high transparency and conductivity simultaneously, as well as excellent mechanical and environmental stability. Especially, the choice of top transparent electrode should also take the deposition procedure into consideration as the underlying organic materials are generally susceptible to high temperature, organic solvent, etc. As suggested in Fig. 8.3(b), oxide-metal-oxide multilayer structure has shown potential as transparent electrode as well as tunability on various parameters according to specific application. Despite the use of dielectric oxide MoO_3 and ZnO , the conductive metal oxide such as ITO and indium zinc oxide (IZO) can also be employed in the multilayer stack, where the thermal annealing procedure is not needed.^{27,28} In addition, the Ag nanowire electrodes show desirable electrical and optical properties. To overcome the challenges, the nanowires may be embedded in a polymer matrix during coating process when applied in ST-OPVs.²⁹

8.2.2 Reliability of OPV Modules

There are primarily two types of failure mechanisms of all electronic devices: intrinsic and extrinsic. Intrinsic mechanisms are those due to changes in a fundamental property of the materials and structures over time, such as photo- or electro-chemical degradation of the molecular constituents in the layer stack, changes in film morphology, or chemical reactions between species at the interfaces,^{30–32} etc. Extrinsic failure mechanisms might include package failure, ingress of contaminants (e.g. O_2 and H_2O) into the package during fabrication or from environmental

exposure, impurities within the materials left during processing, and delamination of contacts from the device or package.^{33,34}

Previous reliability studies have mostly focused on laboratory scale OPV devices and intrinsic degradation mechanisms. With optimized buffer layers, thermally evaporated fullerene based OPVs have shown exceptionally stability under high intensity illumination with extrapolated operational lifetime over 10000 years.³⁵ Moreover, by inserting interfacial protection layers to impede chemical reaction at interfaces, solution-processed NFA based OPV has shown lifetime over 30 years.³⁶ The operational stability of OPV modules, which is crucial to their commercialization, however, has attracted less attention.

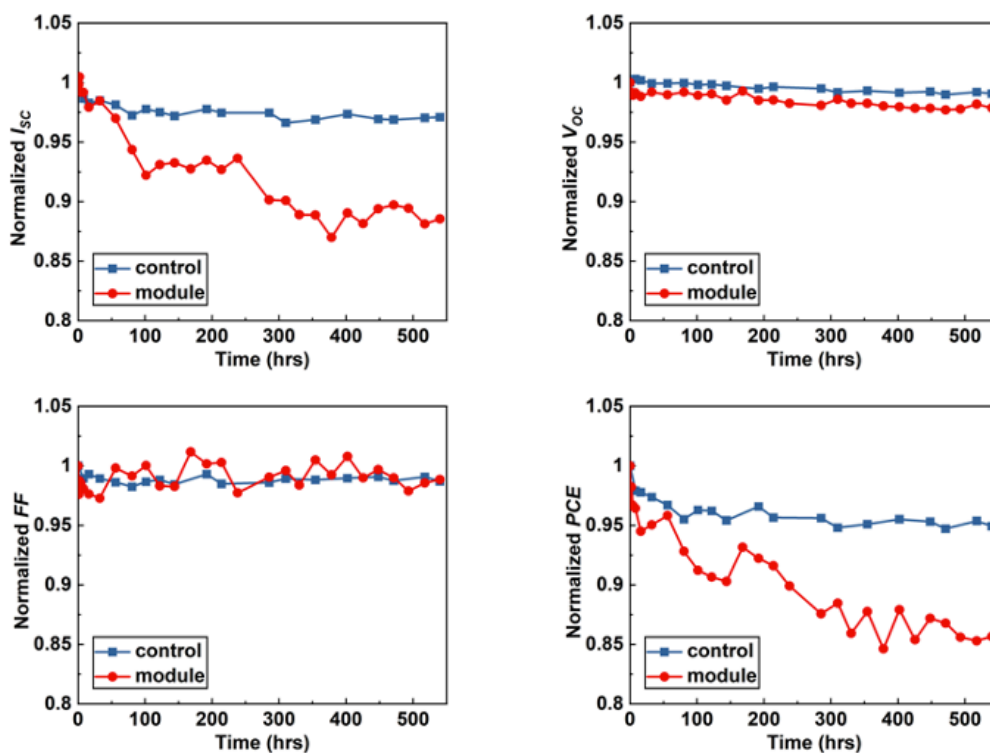


Figure 8.4 Performance degradation of OPV modules.

Performance degradation of PCE-10:BT-CIC based laboratory scale OPV devices and mini-modules under simulated AM1.5G illumination.

Figure 8.4 shows the performance evolution of 4 mm² devices as well as a 12.8 cm² module with same layered device structure based on NIR-absorbing PCE-10:BT-CIC photoactive layer

and interfacial buffer layers under simulated AM1.5G illumination.³⁶ The PCE of OPV module decreased 15% after 540h aging, whereas only 5% loss was observed for the 4 mm² devices.

The faster degradation of module may be attributed to extrinsic mechanisms of package failure and unstable contacts. Although the module was encapsulated the same as 4 mm² devices by bonding a cover glass to the substrate with UV-curable epoxy, the edge-sealing of narrow surrounding bead of epoxy around large area module showed increased risk of package failure compared to laboratory devices, leading to reduced absorption and I_{SC} of the module over time. Moreover, research has shown that such epoxy sealant may result in catastrophic package failure in outdoor operating environment even for small area OPVs. Therefore, it is essential to further investigate reliable encapsulation method for OPVs such as polyisobutylene (PIB) based sealant,³⁷⁻³⁹ atomic layer deposition (ALD),^{40,41} and integration with Ar-filled window panels for ST-OPV module, etc. In addition, the relatively large fluctuation in FF of the module indicates that the contact is unstable throughout the aging, which also needs improvement in future work to realize reliable long-term operation of OPV modules.

Chapter 8

Bibliography

1. Zhan, L. *et al.* Multiphase Morphology with Enhanced Carrier Lifetime via Quaternary Strategy Enables High-Efficiency, Thick-Film, and Large-Area Organic Photovoltaics. *Adv. Mater.* **34**, 2206269 (2022).
2. Nam, M., Lee, C. & Ko, D. H. Sequentially processed quaternary blends for high-performance indoor organic photovoltaic applications. *Chem. Eng. J.* **438**, 135576 (2022).
3. Chen, T. *et al.* Compromising Charge Generation and Recombination of Organic Photovoltaics with Mixed Diluent Strategy for Certified 19.4% Efficiency. *Adv. Mater.* **35**, 2300400 (2023).
4. Lucera, L. *et al.* Guidelines for Closing the Efficiency Gap between Hero Solar Cells and Roll-To-Roll Printed Modules. *Energy Technol.* **3**, 373–384 (2015).
5. Rowell, M. W. & McGehee, M. D. Transparent electrode requirements for thin film solar cell modules. *Energy Environ. Sci.* **4**, 131–134 (2011).
6. Cao, W., Li, J., Chen, H. & Xue, J. Transparent electrodes for organic optoelectronic devices: a review. *J. Photonics Energy* **4**, 040990 (2014).
7. Bender, M. *et al.* Dependence of oxygen flow on optical and electrical properties of DC-magnetron sputtered ITO films. *Thin Solid Films* **326**, 72–77 (1998).
8. Kang, J.-W. *et al.* Reduction of Series Resistance in Organic Photovoltaic Using Low Sheet Resistance of ITO Electrode. *Electrochem. Solid-State Lett.* **12**, H64 (2008).
9. Barnes, T. M. *et al.* Comparing the Fundamental Physics and Device Performance of Transparent, Conductive Nanostructured Networks with Conventional Transparent Conducting Oxides. *Adv. Energy Mater.* **2**, 353–360 (2012).

10. Park, H. J., Park, J. W., Jeong, S. Y. & Ha, C. S. Transparent flexible substrates based on polyimides with Aluminum Doped Zinc Oxide (AZO) thin films. *Proc. IEEE* **93**, 1447–1449 (2005).
11. Xu, D. *et al.* An anode with aluminum doped on zinc oxide thin films for organic light emitting devices. *Phys. Lett. A* **346**, 148–152 (2005).
12. Lynch, D. W. & Hunter, W. R. - An Introduction to the Data for Several Metals. in *Handbook of Optical Constants of Solids* (ed. Palik, E. D.) 341–419 (Academic Press, 1997). doi:<https://doi.org/10.1016/B978-012544415-6.50057-1>
13. Zhao, D., Zhang, C., Kim, H. & Guo, L. J. High-Performance Ta₂O₅/Al-Doped Ag Electrode for Resonant Light Harvesting in Efficient Organic Solar Cells. *Adv. Energy Mater.* **5**, 1500768 (2015).
14. Ji, C., Liu, D., Zhang, C. & Jay Guo, L. Ultrathin-metal-film-based transparent electrodes with relative transmittance surpassing 100%. *Nat. Commun.* **11**, 1–8 (2020).
15. Zhang, C. *et al.* An Ultrathin, Smooth, and Low-Loss Al-Doped Ag Film and Its Application as a Transparent Electrode in Organic Photovoltaics. *Adv. Mater.* **26**, 5696–5701 (2014).
16. Lim, D. C. *et al.* Semi-transparent plastic solar cell based on oxide-metal-oxide multilayer electrodes. *Prog. Photovoltaics Res. Appl.* **26**, 188–195 (2018).
17. Sahu, D. R., Lin, S. Y. & Huang, J. L. ZnO/Ag/ZnO multilayer films for the application of a very low resistance transparent electrode. *Appl. Surf. Sci.* **252**, 7509–7514 (2006).
18. Guo, X. *et al.* Highly Conductive Transparent Organic Electrodes with Multilayer Structures for Rigid and Flexible Optoelectronics. *Sci. Reports 2015 51* **5**, 1–9 (2015).
19. Sahu, D. R., Lin, S.-Y. & Huang, J.-L. ZnO/Ag/ZnO multilayer films for the application

- of a very low resistance transparent electrode. *Appl. Surf. Sci.* **252**, 7509–7514 (2006).
20. Cho, C. K. *et al.* Mechanical flexibility of transparent PEDOT:PSS electrodes prepared by gravure printing for flexible organic solar cells. *Sol. Energy Mater. Sol. Cells* **95**, 3269–3275 (2011).
 21. Vosgueritchian, M., Lipomi, D. J. & Bao, Z. Highly Conductive and Transparent PEDOT:PSS Films with a Fluorosurfactant for Stretchable and Flexible Transparent Electrodes. *Adv. Funct. Mater.* **22**, 421–428 (2012).
 22. Park, H., Rowehl, J. A., Kim, K. K., Bulovic, V. & Kong, J. Doped graphene electrodes for organic solar cells. *Nanotechnology* **21**, 505204 (2010).
 23. De, S. *et al.* Flexible, Transparent, Conducting Films of Randomly Stacked Graphene from Surfactant-Stabilized, Oxide-Free Graphene Dispersions. *Small* **6**, 458–464 (2010).
 24. Jung-Yong Lee, †, Stephen T. Connor, ‡, Yi Cui, § and & Peter Peumans*, †. Solution-Processed Metal Nanowire Mesh Transparent Electrodes. *Nano Lett.* **8**, 689–692 (2008).
 25. Guo, F. *et al.* Nanowire Interconnects for Printed Large-Area Semitransparent Organic Photovoltaic Modules. *Adv. Energy Mater.* **5**, 1401779 (2015).
 26. Lucera, L. *et al.* Printed semi-transparent large area organic photovoltaic modules with power conversion efficiencies of close to 5 %. *Org. Electron.* **45**, 209–214 (2017).
 27. Jeong, J. A. & Kim, H. K. Low resistance and highly transparent ITO–Ag–ITO multilayer electrode using surface plasmon resonance of Ag layer for bulk-heterojunction organic solar cells. *Sol. Energy Mater. Sol. Cells* **93**, 1801–1809 (2009).
 28. Kim, Y. C. *et al.* Bending stability of flexible amorphous IGZO thin film transistors with transparent IZO/Ag/IZO oxide–metal–oxide electrodes. *J. Alloys Compd.* **688**, 1108–1114 (2016).


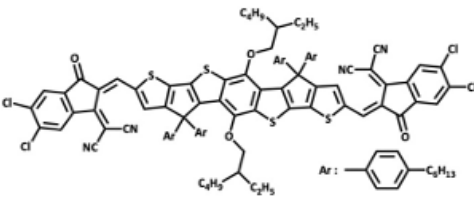
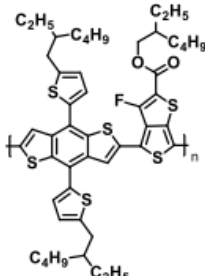
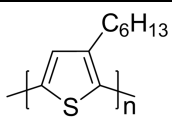
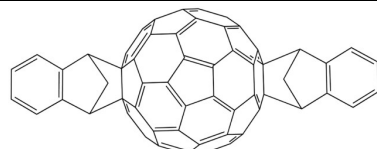
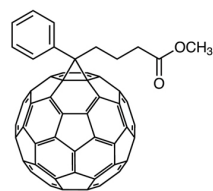
29. Ajuria, J. *et al.* Insights on the working principles of flexible and efficient ITO-free organic solar cells based on solution processed Ag nanowire electrodes. *Sol. Energy Mater. Sol. Cells* **102**, 148–152 (2012).
30. Eszter Voroshazi. *Stability of organic photovoltaic cells: failure mechanisms and operational stability*. In: Rand, B. P. & Richter, H. (eds.) *Organic Solar Cells: Fundamentals, Devices and Upscaling*. (Pan Stanford Publishing, 2014).
31. Grossiord, N., Kroon, J. M., Andriessen, R. & Blom, P. W. M. Degradation mechanisms in organic photovoltaic devices. *Org. Electron.* **13**, 432–456 (2012).
32. Cheng, P. & Zhan, X. Stability of organic solar cells: challenges and strategies. *Chem. Soc. Rev.* **45**, 2544–2582 (2016).
33. Forrest, S. R. Waiting for Act 2: what lies beyond organic light-emitting diode (OLED) displays for organic electronics? *Nanophotonics* **10**, 31–40 (2021).
34. Norrman, K., Madsen, M. V, Gevorgyan, S. A. & Krebs, F. C. Degradation Patterns in Water and Oxygen of an Inverted Polymer Solar Cell. *J. Am. Chem. Soc.* **132**, 16883–16892 (2010).
35. Burlingame, Q. *et al.* Intrinsically stable organic solar cells under high-intensity illumination. *Nature* **573**, 394–397 (2019).
36. Li, Y. *et al.* Non-fullerene acceptor organic photovoltaics with intrinsic operational lifetimes over 30 years. *Nat. Commun.* **12**, 1–9 (2021).
37. Shi, L. *et al.* Accelerated Lifetime Testing of Organic-Inorganic Perovskite Solar Cells Encapsulated by Polyisobutylene. *ACS Appl. Mater. Interfaces* **9**, 25073–25081 (2017).
38. Wang, Y. *et al.* Encapsulation and Stability Testing of Perovskite Solar Cells for Real Life Applications. *ACS Mater. Au* (2021).

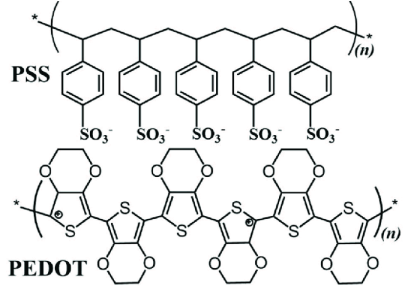
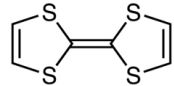
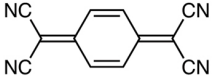
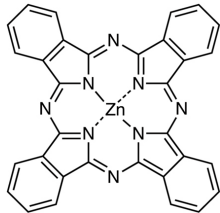
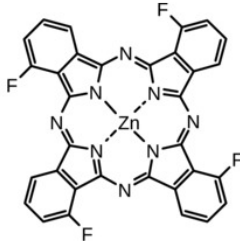

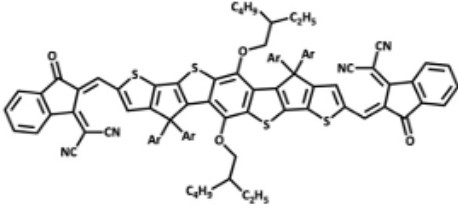
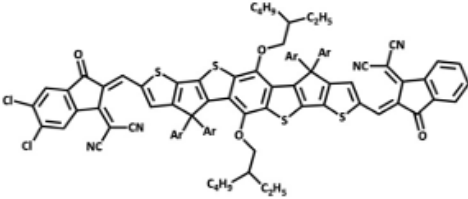
doi:10.1021/ACSMATERIALSAU.1C00045/ASSET/IMAGES/LARGE/MG1C00045_00
05.JPEG

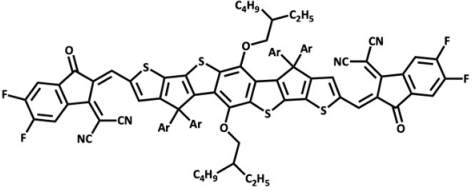
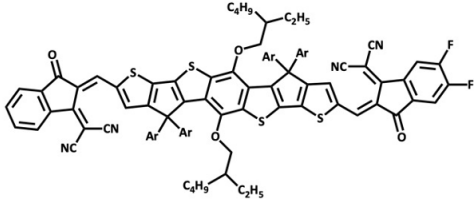
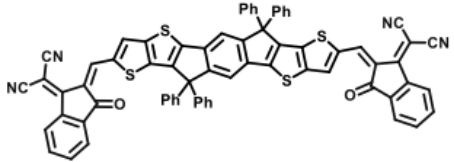
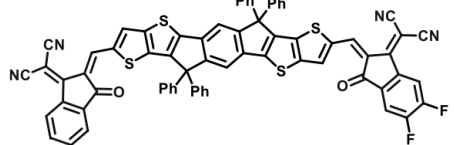
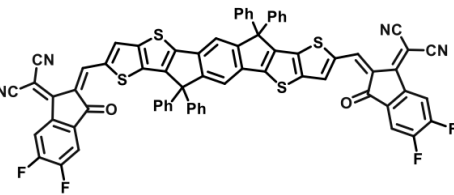
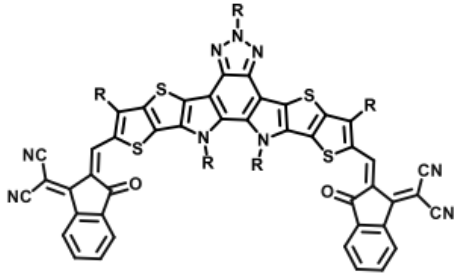
39. Ma, S. *et al.* Development of encapsulation strategies towards the commercialization of perovskite solar cells. *Energy Environ. Sci.* **15**, 13–55 (2022).
40. Zhang, Y. *et al.* Research Progress of Buffer Layer and Encapsulation Layer Prepared by Atomic Layer Deposition to Improve the Stability of Perovskite Solar Cells. *Sol. RRL* **6**, 2200823 (2022).
41. Ramos, F. J. *et al.* Versatile perovskite solar cell encapsulation by low-temperature ALD- Al_2O_3 with long-term stability improvement. *Sustain. Energy Fuels* **2**, 2468–2479 (2018).

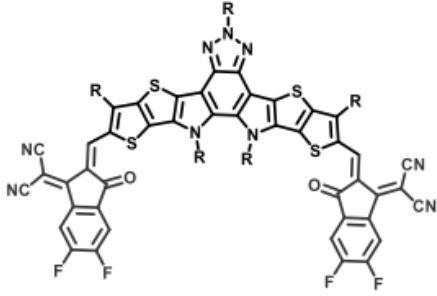
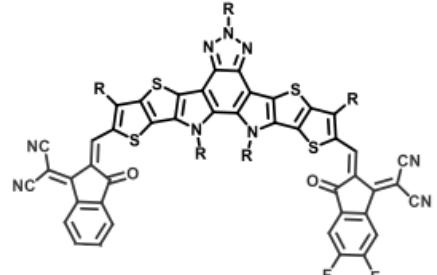
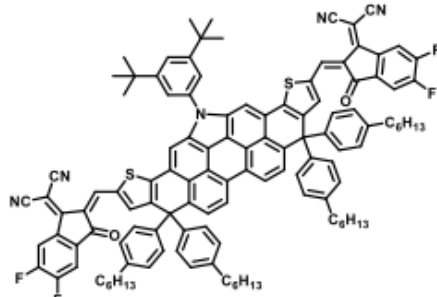
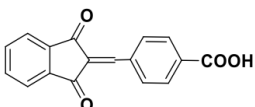
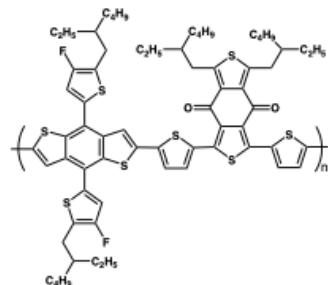
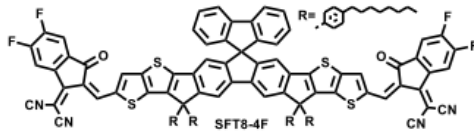
APPENDIX

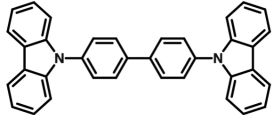
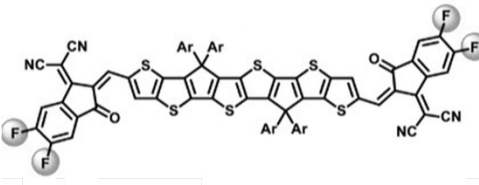
Full Chemical Names and Molecular Structures

Short name	Full chemical name	Chemical structure
C ₇₀	fullerene-C ₇₀	
BT-CIC (BTIC-4Cl)	(4,4,10,10-tetrakis(4-hexylphenyl)-5,11-(2-ethylhexyloxy)-4,10-dihydrodithienyl[1,2-b:4,5b']benzodithiophene-2,8-diyl)bis(2-(3-oxo-2,3-dihydroinden-5,6-dichloro-1-ylidene)malononitrile)	
PCE-10	poly[4,8-bis(5-(2-ethylhexyl)thiophen-2-yl)benzo[1,2-b:4,5-b']dithiophene-co-3-fluorothieno[3,4-b]thiophene-2-carboxylate]	
P3HT	poly(3-hexylthiophene)	
ICBA	indene-C ₆₀ bisadduct	
PC ₆₁ BM	phenyl-C ₆₁ -butyric acid methyl ester	

PEDOT:PSS	poly(3,4-ethylenedioxythiophene): poly(styrenesulfonate)	
TTF	tetrathiafulvalene	
TCNQ	tetracyano-p-quinodimethane	
ZnPC	zinc phthalocyanine	
F ₄ ZnPC	tetrafluoro-zinc phthalocyanine	
C ₆₀	fullerene-C ₆₀	
BT-IC	(4,4,10,10-tetrakis(4-hexylphenyl)-5,11-(2-ethylhexyloxy)-4,10-dihydrodithienyl[1,2-b:4,5b']benzodithiophene-2,8-diyl)bis(2-(3-oxo-2,3-dihydroinden-1-ylidene)malononitrile)	
BTCIC-IC (BTIC-2Cl)	-	

BTIC-4F	(4,4,10,10-tetrakis(4-hexylphenyl)-5,11-(2-ethylhexyloxy)-4,10-dihydrodithienyl[1,2-b:4,5b']benzodithiophene-2,8-diyl)bis(2-(3-oxo-2,3-dihydroinden-5,6-difluoro-1-ylidene)malononitrile)	
BTIC-2F	-	
IT-IC	3,9-bis(2-methylene-(3-(1,1-dicyanomethylene)-indanone))-5,5,11,11-tetrakis(4-hexylphenyl)-dithieno[2,3-d:2',3'-d']-s-indaceno[1,2-b:5,6-b']dithiophene	
ITIC-2F	-	
ITIC-4F	3,9-bis(2-methylene-(3-(1,1-dicyanomethylene)-6,7-difluoro)-indanone))-5,5,11,11-tetrakis(4-hexylphenyl)-dithieno[2,3-d:2',3'-d']-s-indaceno[1,2-b:5,6-b']dithiophene	
Y16	2,2'-((2Z,2'Z)-((12,13-bis(2-ethylhexyl)-3,9-diundecyl-12,13-dihydro-2-(2-ethylhexyl)-[1,2,3]triazole[3,4-e]thieno[2,3":4',5']thieno-[2',3':4,5]pyrrolo[3,2-g]thieno[2',3':4,5]thieno-[3,2-b]indole-2,10-diyl)bis(methanylylidene))bis-(3-oxo-2,3-dihydro-1H-indene-2,1-diylidene))dimalononitrile	

Y16-4F	2,2'-((2Z,2'Z)-((12,13-bis(2-ethylhexyl)-3,9-diundecyl-12,13-dihydro-2-(2-ethylhexyl)-[1,2,3]triazole[3,4-e]thieno[2,3":4',5']thieno-[2',3':4,5]pyrrolo[3,2-g]thieno[2',3':4,5]thieno- [3,2-b]indole-2,10-diyl)bis(methanylylidene))bis-(5,6-difluro-3-oxo-2,3-dihydro-1H-indene-2,1- diylidene))dimalononitrile	
Y16-2F	-	
BEIT-4F	2,2'-((2Z,2'Z)-((14-(3,5-di-tert-butylphenyl)-4,4,9,9-tetrakis(4-hexylphenyl)-9,14-dihydro-4H-dithieno[2',3':2,3;3":2'':10,11]piceno[1,14,13,12-bcdefgh]carbazole-2,11-diyl)bis(methanylylidene))bis(5,6-difluoro-3-oxo-2,3-dihydro-1H-indene-2,1-diylidene))dimalononitrile	
IC-SAM	-	
PM6 (PBDBT-2F)	poly[(2,6-(4,8-bis(5-(2-ethylhexyl)-3-fluoro)thiophen-2-yl)-benzo[1,2-b:4,5-b']dithiophene))-alt-(5,5-(1',3'-di-thienyl-5',7'-bis(2-ethylhexyl)benzo [1',2'-c:4',5'-c']dithiophene-4,8-dione)]	
SFT8-4F	-	

CBP	4,4'-Bis(N-carbazolyl)-1,1'-biphenyl	
TT-FIC	(4,4,10,10-tetrakis(4-hexylphenyl)-4,10-dihydrothieno[2'',3'':4',5']thieno[3',2':4,5]cyclopenta[1,2-b]thieno[2,3-d]thiophene-2,8-diyl)bis(2-(3-oxo-2,3-dihydroinden-5,6-difluoro-1-ylidene) malononitrile)	
DBP	tetraphenyldibenzoperiflanthene	